Study of RF Plasma Technology Applied to Air-Breathing Electric Propulsion

by

Adam Shabshelowitz

A dissertation submitted in partial fulfillment
of the requirements for the degree of
Doctor of Philosophy
(Aerospace Engineering)
in the University of Michigan
2013

Doctoral Committee:

Professor Alec D. Gallimore, Chair
Associate Professor John E. Foster
Assistant Professor Benjamin Longmier
Dean R. Massey, ElectroDynamic Applications, Inc.

$$N = R^* \times f_p \times n_e \times f_l \times f_i \times f_c \times L = 10$$

– Dr. Frank Drake, 1961

For my friends and family. Thank you.

ACKNOWLEDGMENTS

We did it! Of course, I say “we” because there is no way I could have done this all on my own. I would like to thank everyone for everything that they did to help me get to this point. First, thanks to my advisor, Alec Gallimore. Thank you for your giving me you unwavering support and sage wisdom throughout my time at Michigan. I am truly grateful for the opportunities and experiences that you have provided for me, and I am proud to be a part of the PEPL family.

Thanks also to my dissertation committee members. Professor Foster, thank you for being so encouraging, for listening to and understanding the woes of RF plasma research, and for being so friendly at conferences and in the hallways. Professor Longmier, welcome to Michigan, and thank you for being a part of my dissertation committee. It was great getting to know you first as an Ad Astra employee at PEPL, then at conferences, and now I am glad that Michigan has added a great Professor to the Aerospace department. I look forward to seeing the great things that you will accomplish. And finally, thank you, Dr. Dean. Our time in Ann Arbor overlapped almost exactly, and I am grateful to have had the opportunity both to work with you in the lab and to become your friend. You took an interest in my research, provided me with encouragement and advice, and were always willing to just try stuff out in the lab. Your honesty, creativity, and multi-disciplinary-mindedness is an inspiration to us all.

I would also like to thank the National Science Foundation for accepting me as a Graduate Research Fellow. The NSF fellowship provided me with that extra bit of encouragement to follow through with a research plan and get a Ph.D.

My thanks also go to the members of PEPL, past and present. To those who came before me and made PEPL the great place it is, and to those who have showed me how to continue that tradition. A special thanks goes to Tim Smith not only for being a knowledge base for all my PEPL questions, but also for allowing me to be a lab instructor for Aero 305. Thank you for continuing to teach the undergrads how to properly use the lab equipment and for being a great mentor to me. Thank you, Pete, for patiently showing me how to work with Hall thrusters. To the PEPL members that I have met at conferences and during visits to Ann Arbor: Prashant, Dan, Dave, Rich, and Brad. It has been great getting

to know you all. To the PEPL people who came before me: Thank you, Bryan, for showing me the ropes at PEPL. I look forward to working with you again at Lincoln Laboratory. Thank you, Kristina, for teaching me the RF rain dance and for getting me involved with helicon research at PEPL. Thank you, Sonca, for helping my NSF application succeed. Thank you, Robbie, for always being curious and willing to teach me about whatever either of us were working on. Thank you, Tom, for being the voice of reason and showing us all what a strong work ethic really is. Thank you, Rohit, for always sticking with a problem until it is solved, and for being Giggles. Thank you, Ricky, for always being courteous and helpful in the lab. Thank you, Wensheng, for teaching me both about lasers and how to manage my ninjas. Thanks to Mike M. for always being willing to share equipment stashes or show me how to use LabView codes.

To my contemporaries at PEPL: Thank you, Laura, for being my RF buddy, and for the pumpkin pie cupcakes. Those are awesome. And stop making that look while you're reading this. Thank you Ray ("Monk"), for being a great quals study partner, and for always making things nicer in the lab, both in terms of the equipment and the general cheerfulness. I wish you all the best at Space Systems Loral.

To the younger/more recent members of PEPL: Roland ("CE"), just remember to relax. The X3 will be here soon, and then we'll all be expecting pictures like the baby photos that get sent out. Mike S., Kim, and Chris D., keep up the good work and hang in there. It's been a great pleasure working with you all. Chris B., I hope you come back to continue working at the lab. You enthusiasm for everything to do with space is great for morale. Scott, I know you're the new guy now, but before you know it you'll be the senior lab member. Keep up the PEPL tradition.

Extra special thanks to Denise, Tom, Terry, Chris, Eric, Dave, Suzanne, Cindy E., and Aaron for everything that you do for all of us graduate students. We wouldn't get through it without your help and support. Thank you, Colleen, for helping us always find a time to meet with Alec. A special thank you also goes to Peggy Gramer for helping me get through all the paperwork for my NERS MSE.

Many thanks also go to Anthony Sebastian of the University of Michigan's Lurie Nanofabrication Facility for showing me a great deal about implementing RF hardware in plasma systems. I'd also like to thank Professor Mitchell Walker, Logan Williams, and Alex Kieckhafer of Georgia Tech for many helpful discussions regarding RF. I also would like to acknowledge the Air Force Research Laboratory and Aerojet for their creation of the HHT.

Thank you to all of the friends that I've met while in Ann Arbor. In particular, to the Aero Scotch and Wine Clubs, the med students, the golf course tailgate, and the Michigan

Marlies for helping me keep a healthy level of work-life balance, and for introducing me to Michigan sports. I don't have enough space to list every one, but each and every one of you has helped me along the way, and I hope you all know that you are appreciated.

Thank you to all of my friends back home for constantly asking me when I'll be done. Well, I'm done and I'm moving back home, so I'll see you all very shortly. Finally, thanks to my family for being so supportive of me all the time. Eric and Leah, I look forward to seeing you more often. Mom and Dad, thank you for trusting me enough to take some time off. I love you, and even though I'm not great at showing it, I really do appreciate all of the love and support that you always give to me.

Adam Shabshelowitz
January 2013

TABLE OF CONTENTS

LIST OF FIGURES

LIST OF TABLES

LIST OF APPENDICES

LIST OF ABBREVIATIONS

ABIE Air-Breathing Ion Engine

AC Alternating Current

DC Direct Current

DSMC Direct Simulation Monte Carlo

EMI Electromagnetic Interference

EP Electric Propulsion

FCC Federal Communications Commission

FRC Field Reversed Configuration

GOCE Gravity field and steady-state Ocean Circulation Explorer

HHT Helicon Hall Thruster

HWHM Half-Width at Half-Maximum

ISM Industrial, Scientific, and Medical

ISRU In-Situ Resource Utilization

IVD Ion Voltage Distribution

JAXA Japan Aerospace eXploration Agency

LEO Low Earth Orbit

LVTF Large Vacuum Test Facility

LVDT Linear Variable Differential Transformer

MHD Magnetohydrodynamic

NASA National Aeronautics and Space Administration

PEPL Plasmadynamics and Electric Propulsion Laboratory

PHARO Propellant Harvesting of Atmospheric Resources in Orbit

PPIMO Propellant Production in Mars Orbit

PROFAC Propulsive Fluid Accumulator

RF Radio frequency

RPA Retarding Potential Analyzer

RPT Radio frequency Plasma Thruster

SLATS Super Low Altitude Test Satellite

SMAD Space Mission Analysis and Design

SNR Signal-to-Noise Ratio

NOMENCLATURE

Constants

c	Speed of light, 2.9979×10^8	[m/s]
e	Base of the natural logarithm, 2.7183	[-]
e	Elementary charge, 1.6022×10^{-19}	[C]
eV	Electron Volt, 1.6022×10^{-19} or 11604	[J or K]
$\mathcal{F}$	Faraday constant, 96485	[C/mol]
G	Universal gravitational constant, 6.6738×10^{-11}	[m^3/kg/s^2]
g_0	Earth standard gravity acceleration, 9.8067	[m/s^2]
j	Imaginary number, $\sqrt{-1}$	[-]
k_B	Boltzmann constant, 1.3807×10^{-23}	[J/K]
m_e	Electron mass, 9.1094×10^{-31}	[kg]
$M_\oplus$	Mass of Earth, 5.9722×10^{24}	[kg]
R_e	Radius of Earth, 6.3781×10^6	[m]
ε_0	Vacuum permittivity, 8.8542×10^{-12}	[F/m]
μ_0	Vacuum permeability, $4\pi \times 10^{-7}$	[H/m]
π	3.1416	[-]

Variables

a	Coaxial cable shield inner diameter	[m]
A	Area	[m^2]
$A_{c,eff}$	Effective probe collection surface area	[m^2]
A_{drag}	Spacecraft cross-sectional area, excluding inlet	[m^2]
A_{inlet}	Area of spacecraft gas collector inlet	[m^2]
A_x	Cross-section for collision with debris	[m^2]
b	Coaxial cable center conductor outer diameter	[m]
B	Susceptance	[Ω^{-1}]
$\vec{B}$	Magnetic field	[T]
B_z	Axial magnetic field strength	[T]
C	Capacitance	[F]
C_D	Drag coefficient	[-]

C_{gas}	Ion gauge gas correction factor	[-]
D	Diffusion coefficient	[m^2/s]
D_A	Optical payload aperture diameter	[m]
d_{hs}	Gas molecule hard-sphere diameter	[m]
$\vec{E}$	Electric field	[V/m]
E_1	Voltage exchange parameter	[-]
E_2	Mass exchange parameter	[-]
f	Circular frequency	[1/s]
F	Force	[N]
$f(\varepsilon)$	Electron energy distribution function	[1/J]
$f(V)$	Ion voltage distribution	[1/V]
F_D	Drag force	[N]
$\vec{F}_{el}$	Electric force	[N]
F_i	Theoretical thrust due to accelerated ions	[N]
F_T	Thrust force	[N]
G	Conductance	[Ω^{-1}]
h	Orbit altitude	[km]
I	Current	[A]
I_{axial}	Axial ion beam current	[A]
I_{beam}	Total ion beam current	[A]
I_c	Current collected by probe	[A]
I_f	RF forward current amplitude	[A]
I_L	RF current through load	[A]
I_r	RF reflected current amplitude	[A]
I_{sp}	Specific impulse	[s]
k	mass fraction or Wave number $\equiv 2\pi/\lambda$	[- or m^{-1}]
k_G	Spacecraft solar panel area geometry factor	[-]
k_l	Rate constant for process l	[m^3/s]
Kn	Knudsen number	[-]
l	Transmission line length	[m]
L	Inductance	[H]
$L_{s/c}$	Spacecraft length	[m]
m	Mass	[kg]
$\dot{m}$	Mass flow rate	[kg/s]
$\mathcal{M}$	Molar mass	[kg/mol]
M	Vehicle mass	[kg]

M_0	Initial vehicle mass	[kg]
M_f	Final vehicle mass	[kg]
n	Number density	[m^{-3}]
n_d	Density of debris objects	[m^{-3}]
p	True pressure	[Torr]
P	True RF power delivered	[W]
$\bar{P}$	Measured RF power delivered	[W]
P_3	Normal momentum flux incident on flat plate	[N/m^2]
p_b	Base pressure	[Torr]
P_c	Probability of collision	[-]
P_{elec}	Electrical power delivered to thruster	[W]
P_{FWD}	Forward RF power	[W]
P_{jet}	Exhaust jet power	[W]
p_{ob}	Observed ion gauge pressure	[Torr]
P_{REF}	Reflected RF power	[W]
P_{req}	Power required	[W]
$P_{RF,A}$	Antenna RF power	[W]
q	Charge	[C]
r	Faraday probe distance from thruster	[m]
r_L	Larmor or cyclotron radius	[m]
R	Resistance	[Ω]
s	Distance along trajectory	[m]
s_3	Speed ratio	[-]
t	Time	[s]
t_b	Thrust duration time	[s]
T	Temperature	[K]
v, $\vec{v}$	Velocity	[m/s]
v_B	Bohm velocity	[m/s]
V	Voltage or electric potential	[V]
V_{bias}	Probe bias voltage	[V]
v_{ex}	Effective exhaust velocity of thruster	[m/s]
v_f	Final vehicle velocity	[m/s]
V_f	Floating potential or RF forward voltage amplitude	[V]
V_i	Effective ion acceleration voltage	[V]
V_{mp}	Exhaust ion most probable potential	[V]
v_o	Orbital velocity	[m/s]

V_p	Plasma potential	[V]
V_r	RF reflected voltage amplitude	[V]
v_{rel}	Relative velocity	[m/s]
V_{ret}	RPA Ion retarding grid potential	[V]
v_{th}	Mean thermal velocity	[m/s]
v_0	Initial vehicle velocity	[m/s]
v_3	Flat plate velocity normal to surface area	[m/s]
$\|V_-\|$	Reflected voltage amplitude	[V]
$\|V_+\|$	Forward voltage amplitude	[V]
x	Spatial coordinate	[m]
X	Reactance	[Ω]
X'	Ground resolution	[m]
Y	Admittance	[Ω^{-1}]
Z	Impedance	[Ω]
Z_{cap}	Capacitor impedance	[Ω]
Z_{ind}	Inductor impedance	[Ω]
Z_S	Source impedance	[Ω]
Z_0	Characteristic impedance	[Ω]
$\|\Gamma\|$	Magnitude of the reflection coefficient $\equiv \|V_-\| \,/\, \|V_+\|$	[-]
ε	Electric permittivity or electron energy	[F/m or J]
ε_r	Relative permittivity	[-]
ε_{V_-}	Reflected voltage amplitude measurement error	[V]
ε_{V_+}	Forward voltage amplitude measurement error	[V]
ε_P	Relative power error	[-]
$\varepsilon_{V_\pm}$	Relative voltage measurement error $\equiv \Delta V_\pm \,/\, \|V_\pm\|$	[-]
η	efficiency	[-]
η_A	Antenna efficiency	[-]
η_{BP}	Beam power efficiency	[-]
η_I	Current utilization efficiency	[-]
η_M	Matching network efficiency	[-]
η_{PRF}	RF power factor	[-]
η_{PV}	Solar panel photovoltaic efficiency	[%]
η_{RF}	Thrust efficiency due to RF power	[-]
η_t	Thruster efficiency	[-]
η_V	Voltage utilization efficiency	[-]
θ	Angular position of Faraday Probe	[rad]

θ_{div}	Effective exhaust divergence half-angle	[degrees]
λ	Wavelength	[m]
λ_D	Debye length	[m]
λ_{mfp}	Mean free path for collision	[m]
λ_z	Helicon axial wavelength	[m]
μ	Magnetic permeability or electric mobility	[H/m or m^2/V/s]
μ_r	Relative permeability	[-]
ν	Collision frequency	[1/s]
Π_{AB}	Air-breathing spacecraft feasibility parameter	[-]
ρ	Mass density	[kg/m^3]
ρ_q	Charge density	[C/m^3]
σ_l	Cross section for process l	[m^2]
τ_L	Spacecraft lifetime or mission duration	[-]
Φ_3	Normal mass flux incident on flat plate	[$kg/m^2/s$]
Φ_P	Propellant utilization efficiency	[-]
Ψ_B	Beam divergence efficiency	[-]
ω	Angular frequency	[rad/s]
ω_c	Cyclotron frequency	[1/s]
ω_p	Plasma frequency	[1/s]

Subscripts

a	Anode or ambipolar
bus	Spacecraft bus
c	Cathode or collector or cyclotron
d	Discharge
DC	Direct current
e	Electron
fuel	Spacecraft fuel
g	Neutral gas
i	Ion
in	Inlet or input
k	Species k
L	Load or lifetime
m	Momentum exchange
mag	Magnet
p	Components in parallel

p/l	Spacecraft payload
pr	Propellant
RF	Radio frequency
s	Components in series
s/c	Spacecraft
tot	Total
$\parallel$	Parallel to magnetic field
$\perp$	Perpendicular to magnetic field

ABSTRACT

Study of RF Plasma Technology Applied to Air-Breathing Electric Propulsion

by

Adam Shabshelowitz

Chair: Alec D. Gallimore

Satellites in low Earth orbit experience an aerodynamic drag force due to the finite density of gas in the thermosphere. Left unchecked, this drag force acts to reduce satellite altitude, eventually causing re-entry. To maintain a satellite in its intended orbit, an onboard propulsion system is typically implemented to counteract the drag. The initial satellite mass delivered to a particular orbit is fixed by the launch vehicle, and the propulsion system requires a significant portion of this mass to be allocated to propellant. These and other altitude-dependent factors strongly affect spacecraft design and cost of the mission.

Electric propulsion systems use electric and magnetic fields rather than chemical energy to accelerate propellant to high exhaust velocities. The physical mechanisms that produce thrust are independent of propellant species, and so the ambient gas in the thermosphere may be used as propellant. However, the atmosphere consists of gases that are not typically used in electric propulsion systems, and previous studies have shown that operating with these gases may reduce thruster performance and lifetime. Radio frequency plasma systems are used by the semiconductor manufacturing industry to efficiently create a dense plasma source from a wide variety of gases. These systems may therefore be capable of increasing the performance of electric propulsion systems operating with atmospheric gases.

This dissertation presents an experimental investigation into the use of radio frequency plasma in an air-breathing electric propulsion system. Based on the requirements for such a system, two novel thrusters are tested in the laboratory. The first thruster uses only radio frequency power and a magnetic field to create thrust. The second is a two-stage thruster that uses a radio frequency ionization stage to increase the propellant utilization efficiency of a traditional Hall thruster. Thruster performance measurements are presented in the context of an air-breathing system, as well as plasma probe measurements of the exhaust to characterize the major loss mechanisms. The results suggest that an air-breathing satellite is feasible with currently available technology.

CHAPTER 1

Introduction

On October 4th 1957, the launch of Sputnik by the former Soviet Union marked the beginning of the Space Age. Today, only 55 years later, the satellite industry operates nearly a thousand spacecraft in orbit around the Earth, employs over 240,000 people in the United States, and earned $177 billion in revenues in 2011 [1]. Satellites have become a part of everyday life, playing essential roles in personal navigation, global communications, weather prediction, and emergency response. For scientists, satellites are an essential tool for investigating deep, far-reaching questions like how the universe began, and practical, close-to-home questions like how solar activity affects the power grid on Earth. Satellites are produced in many shapes and sizes, and the rise in popularity of inexpensive, university-built nano- and pico-satellites demonstrates an interest in exploring innovative uses for alternative satellite form factors [2].

Although the density of the atmosphere decreases with increasing altitude, satellites in Low Earth Orbit (LEO) experience an aerodynamic drag force. This drag force causes satellites in LEO to fall toward the Earth, and eventually burn up in the Earth's atmosphere. On-board propulsion systems are generally employed to maintain LEO satellites in their intended orbit. These propulsion systems all fall under the category of *rockets*. One downside of rocket systems is that they must store all of the propellant on the vehicle. Since satellites are not typically refueled in space, the usable lifetime of a state-of-the-art LEO satellite is fundamentally limited by the amount of propellant the satellite initially carries

with it during launch. Launch vehicles can only deliver a fixed amount of mass into a given orbit. Thus, the propellant mass launched with a satellite directly takes away from mass that could be allocated to other subsystems, including the payload.

The only way to increase the usable amount of mass available to a satellite without launching more mass from Earth is to utilize natural resources that are available in space. The practice of using materials that are already in space is known as In-Situ Resource Utilization (ISRU). The development of ISRU technologies has been identified as critical for sustaining a long-term space exploration program that ventures beyond LEO [3]. Recent ISRU demonstration activities at the National Aeronautics and Space Administration (NASA) have focused on the production of oxygen from lunar regolith, which is useful both for providing air to astronauts and for fueling a lunar launch vehicle [4]. Earlier studies have considered using the gas in the Earth's upper atmosphere [5]. The composition of the atmosphere in LEO is mostly nitrogen and oxygen, which are useful for both life support and rocket propulsion. The development of ISRU capabilities in LEO would yield enabling and sustaining technologies for future space missions to LEO and more distant destinations.

1.1 Motivation

Satellites are purpose-built to perform a particular set of tasks, referred to as the *mission*. Many engineering trades must be considered when designing a spacecraft to fulfill the specific mission objectives. Typically, there is more than one system architecture that will fulfill all of the requirements for accomplishing the mission. The most desirable solution is the one that accomplishes all of the goals of the mission at the lowest cost. As the well-known textbook Space Mission Analysis and Design (SMAD) states, "Space is expensive. Cost is a fundamental limitation to nearly all space missions and is becoming more so" [6]. It is therefore important to investigate concepts that may have a profound impact on cost. Based on publicly available information for one of the least expensive launch vehicles, the

Space Exploration Technologies (SpaceX) Falcon 9, the cost-per-mass to LEO is currently about $4,100 per kilogram [7].

Some aspects of mission design for all satellites are altitude-dependent. For example, for a given launch vehicle and orbit inclination, more mass can be launched into a lower-altitude orbit. If the launch vehicle cost is not sensitive to the choice of orbit, then the cost-per-mass of a satellite may be reduced by employing a more massive satellite at a lower orbit. This altitude-dependence of launch vehicle capability tends to be stronger for smaller launch vehicles [7, 8]. Since smaller launch vehicles tend to be less expensive than larger ones, the greatest reduction in cost would be realized by using a small launch vehicle in a low orbit.

Many LEO satellites are used for Earth observation. An important figure of merit for observation is the *ground resolution*, X', which is the length scale of the smallest feature that the satellite can image on the ground. The ground resolution is physically limited by the aperture diameter of the optics, D_A, the wavelength of light being observed, λ, and the satellite altitude, h. The diffraction-limited resolution is given by Eq. 1.1 [6], where all variables are in units of meters and the constant factor of 2.44 is two times the first zero of the Bessel function of the first kind.

$$X' = 2.44\frac{h\lambda}{D_A} \tag{1.1}$$

According to Eq. 1.1, the minimum diameter of the optical instrument for a required ground resolution linearly decreases with decreasing orbit altitude. One study determined that the cost of large, space-based telescopes scales with the square of aperture diameter (i.e. Cost $\propto D_A^2$) [9]. Thus, a reduction in the required aperture size would likely yield significant cost savings, even for a smaller optical system. The Super Low Altitude Test Satellite (SLATS) was developed to take advantage of this property [10]. The Japan Aerospace eXploration Agency (JAXA) is planning to launch SLATS in 2013 [11], showing that there

is potential long-term interest in developing satellites that operate at lower altitudes. Additional performance gains, such as increased communication signal-to-noise ratio and strategic observation advantages, have been cited as benefits to operating at lower altitudes [12].

Risk is another major consideration for satellite mission planning. The impact probability of a piece of debris with a spacecraft, P_c, can be estimated using Eq. 1.2, where n_d is the density of debris objects, A_x is the collision cross-section, τ_m is the mission duration, and v_{rel} is the relative velocity between the spacecraft and the debris [6]. There is a high probability that most spacecraft will encounter micrometeoroids and small orbital debris during their operational lifetime, and so passive shielding is often used to protect the spacecraft components [6].

$$P_c = 1 - e^{-n_d A_x \tau_m v_{rel}} \tag{1.2}$$

Orbital debris populations (a.k.a. "space junk") in LEO significantly increase with altitude up to about 1000 kilometers, as shown by Fig. 1.1 [13]. This is especially troublesome in high-inclination orbits, which are greatly valued for Earth observation missions [14].

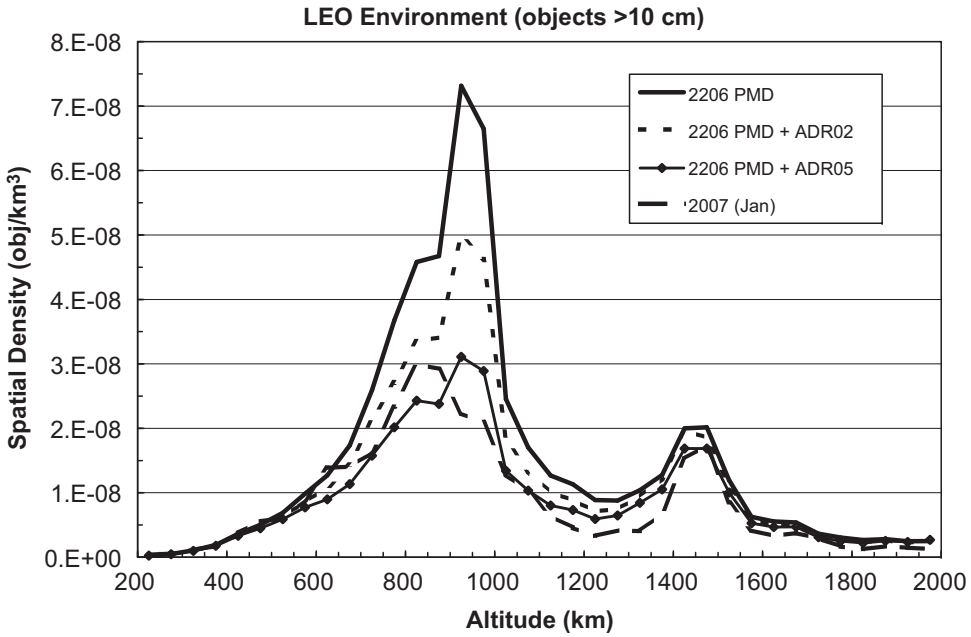

Figure 1.1: Density of orbital debris objects larger than 10 centimeters. The known 2007 debris environment and projected population after 200 years are shown. The plot indicates that post-mission disposal (PMD) must be observed and five LEO objects must be actively removed per year (ADR05) in order to keep the future LEO debris environment stable [13].

Debris populations will naturally increase when there is enough debris is in orbit such that collisions between the pieces of debris occur more frequently than the pieces re-enter. The collisions cause the pieces of debris to break up into more, smaller fragments, and the smaller fragments may still be large enough to cause significant damage to a spacecraft. Recent studies have shown that the current debris population is sufficiently large that it will continue to increase, even if nothing else is launched into space in the future [13]. Thus, another benefit of operating a satellite at a lower altitude is a significant reduction in the risk of an on-orbit collision with an uncontrolled object. If the risk of collision is sufficiently reduced, this could translate to an increase in payload mass by eliminating the need for passive shielding used to protect the satellite. Operating at a lower altitude will also naturally dispose of the satellite in Earth's atmosphere rapidly at end-of-life, and would therefore be far less likely to contribute to the long-term problem of debris population growth.

One disadvantage to operating at a lower altitude is that the atmospheric drag increases significantly. If a satellite operating in a circular orbit below 300 kilometers does not compensate for drag, it is likely to re-enter the Earth's atmosphere within a few months [6]. If the spacecraft constantly compensates for drag, then a large fraction of the satellite's launch mass would necessarily be allocated for propellant in order to extend the satellite lifetime. The mass of propellant required would mitigate the gains discussed above. The increase in drag is the main reason why almost no satellites operate at such low orbits.

The increased drag is due to an increase in ambient gas density. If a satellite were to use the ambient gas as propellant for an on-board propulsion system, then the satellite could be sustained at lower altitudes without requiring a high propellant mass fraction at launch. This type of a propulsion scheme is referred to as an *air-breathing* system, even though the chemical composition of the gas in LEO may be different than that found on the Earth's surface. The development of an orbital air-breathing propulsion system has the potential to significantly reduce the cost of satellites, especially those performing Earth-observation missions in LEO.

The cost savings would be realized by extending the useful lifetime of satellites in very low LEO orbits. This would allow a given launch vehicle to deliver a greater amount of mass into orbit, without requiring much of that mass to be propellant. As previously discussed, operating an Earth-observing satellite at a lower orbit would reduce the size (and cost) of the observation instrument required for a given ground resolution. The air-breathing propulsion system may also enable high-Δv (i.e. expensive) maneuvers, such as orbit inclination changes, without reducing the payload mass or spacecraft lifetime. In addition, it would allow scientist to gain greater access to very low LEO altitudes. The atmosphere at these altitudes is very interesting because it is not currently well-characterized. Finally, the demonstration of an air-breathing spacecraft would provide a strong example of the benefit of ISRU, without requiring the large budget and risk associated with a mission beyond Earth's orbit.

1.2 History of Air-Breathing Spacecraft

Concepts for using ambient gas in the upper atmosphere as rocket propellant are nearly as old as Sputnik. In the 1960s, solar cells were only about 12% efficient [15] and it was anticipated that nuclear reactors would be tested on-orbit within the decade [16]. So, early studies focused on the feasibility of higher-power systems. The later development of more advanced propulsion systems and more efficient solar cells has led to a revival of interest in the past decade, with much of the recent work focusing on inlet and thruster design.

1.2.1 Early Studies

The first published studies analyzing the potential for air-breathing orbital vehicles came about in the late-1950s. These studies attempted to determine the optimal vehicle parameters for the accumulation of air [5, 17, 18]. The air-accumulating vehicles would be stationed in LEO and used as propellant depots for refueling lunar or interplanetary

vehicles coming from the Earth's surface. These studies mainly pointed out the characteristics of the power and propulsion systems that would be necessary and/or optimal for the accumulation of air. The systems that these studies considered were feasible with 1960s technology, but were not readily available at the time.

In 1959, Sterge Demetriades, a research scientist at Northrop Corporation, described a Propulsive Fluid Accumulator (PROFAC) that was intended to operate at 85–120-kilometer altitudes, and collect 400 kilograms of air per day for every square meter of inlet area [5]. He suggested that solar power could make the PROFAC feasible above 150 kilometers, but that the idea is not economical above 130 kilometers, and so the baseline design would use a 1958 state-of-the-art 6-megawatt reactor in an 11-ton vehicle at 100 kilometers to collect 43 tons of air every 100 days. Demetriades also suggested that a larger PROFAC system could be used for lunar travel with a nuclear thermal rocket, or that the accumulated air could be transferred to a separate vehicle to be used as oxidizer with hydrogen lifted from the Earth's surface. Demetriades noted that it would be necessary to design a Magnetohydrodynamic (MHD) accelerator to use as a thruster for the PROFAC with the collected nitrogen as propellant. The MHD accelerator would be required in order to produce the high thruster exhaust velocity required to efficiently compensate for the drag [5].

Around the same time that the PROFAC concept appeared, Felix Berner and Morton Camac of the Avco-Everett Research Laboratory described a similar "air scooping vehicle" that would operate at altitudes from 75 kilometers up to and above 170 kilometers [17]. They gave a more thorough mathematical treatment of the problem than Demetriades, including technical details, such as the required heat flux rejection. They also considered the "breakeven time" after which an air scooping system gives an economical advantage over a conventional vehicle. They found that the optimum propulsion system for the air scooping vehicle would have an effective exhaust velocity of about twice the orbital velocity when operating in a circular orbit (i.e. a specific impulse, I_{sp}, of approximately 1600 seconds). They also noted that the break even time strongly depends on the specific weight of the

power system, and on the cost of the launch (they estimated that launch costs will be $100 per pound-mass to LEO in the future). They concluded that nuclear reactors would be appropriate for 100–110-kilometer altitudes, and that the vehicle would reach an economical break even time after only 10s–100s of days, even in the case of low specific power. They determined that arcjets of the time had too low of an efficiency, and that gridded ion engines had too low of an efficiency at the ideal specific impulse. So, like Demetriades, they concluded that an efficient accelerator for nitrogen must be developed in order to make the concept possible [17].

A. Zukerman and C. B. Kretschmer from the Aerojet-General Corporation studied the feasibility of using chemical energy stored in the upper atmosphere as fuel for a ramjet [19]. Their concept relied on the fact that atomic oxygen is the majority component of the atmosphere above 100 km, and that atomic oxygen recombination is an exothermic reaction. They gave a detailed treatment that deemed this concept to be infeasible without the addition of auxiliary propellant. They also examined whether the heat due to friction and oxygen recombination could be transferred to an on-board coolant fluid, which would then be expanded through a nozzle to produce thrust. However, they found that this concept had no advantage over a traditional chemical propulsion system [19].

Finally, Aleksander Dolgich presented early Soviet research of the 1960s regarding air-breathing satellites. His work mainly summarized ten papers that appeared in Soviet journals. Dolgich focused on the power required for the concept. He found that a satellite optimally employing a low-thrust, air-scooping space engine is capable of carrying a payload up to 2.5 times greater than one without such a system [18].

1.2.2 Other Applications

Although the work in this dissertation focuses on applications in very low LEO, it is worth noting that similar concepts to air-breathing or atmospheric scooping vehicles have been proposed for much more ambitious programs. Missions operating in locations away

from Earth may be able to achieve a sustainable air-breathing platform, with different engineering challenges presented in different locations. For example, when compared to Earth, Mars is slightly less massive and has a lower intensity of sunlight. Mars also has a much thinner atmosphere with a different composition than that of Earth. Around Mars, both the drag and the mass available for use as propellant would be significantly smaller. A solar-powered mission to Mars would require larger solar panels for a given amount of electrical power. So, a detailed analysis would be required to determine whether current technology might satisfy the power and propulsion requirements for an air-breathing Mars mission. Another interesting body to consider might be Saturn's moon Titan, which is much less massive than Earth, yet has a thicker atmosphere [20].

Perhaps the most ambitious air-breathing-like concept is the "interstellar ramjet" proposed by Robert Bussard of the Los Alamos National Laboratory in 1960 [21]. Bussard's vehicle would ingest interstellar gases, which would undergo nuclear fusion, and then be expelled to produce thrust. This idea was popularized in a science fiction novel titled *Tau Zero* that described an interstellar mission undertaken by fifty people from Earth [22]. An interesting side note is that Bussard's concept is relatively insensitive to starting velocity, and so a large rocket would not be needed to accelerate the interstellar vehicle to near light-speed prior to ignition of the fusion ramjet. An actual mission would require a very large vehicle that would be difficult to construct, but as Bussard aptly stated in his conclusions, "nothing worthwhile is ever achieved easily" [21].

Bryan Palaszewski of the NASA Glenn Research Center presented purely conceptual missions for extracting resources from the atmospheres of the outer planets [23]. The major focus of his work was the mining of Helium-3 for fusion energy sources. Palaszewski also noted that many natural resources relevant for life support and building materials may be extracted to sustain permanent establishments in the outer solar system. Two of these concepts used "scoopers" and "cruisers" to skim materials from the atmospheres of the gas giants. Although this concept would require a more detailed treatment depending on the

particular application, it suggested that harvested atmospheric gases would likely be the source of propellant for transporting the mined materials.

Michael Minovitch described an overview of a transportation system that uses Berner and Camac's air scooping vehicle to enable re-fueling of a high-mass orbital transfer vehicle [24]. The concept relied on beaming microwave power between ground antenna arrays and the orbiting vehicles to enable an economical "interorbital transportation system." The propellant-accumulating vehicle that Minovitch proposed would operate at 100–110-kilometer altitudes, and so the incoming air flow would flow through intense shock waves. The shock waves would ionize a large fraction of the flow, and so Minovitch proposed that the vehicle could use an MHD generator to extract electrical power from the incoming ionized air. This electrical power would then help to power compression and liquefaction equipment as well as an MHD accelerator that produces thrust for the vehicle. The system Minovitch imagined is quite large, with the MHD generator producing up to 300 megawatts, and the vehicle accumulating a net 4000 kilograms of air per day through a 50-meter diameter air scoop. Minovitch preferred to use the highest specific impulse possible, and so his MHD accelerator was designed to consume 30 megawatts of power to achieve a specific impulse of 3000 seconds [24].

In 2004, Julien-Alexandre Lamamy explored the benefit of Propellant Production in Mars Orbit (PPIMO) for a robotic sample return mission. Mars missions typically use aero-braking maneuvers to reduce the spacecraft speed upon arrival to Mars. So, Lamamy proposed that the aerobraking spacecraft could both collect ambient carbon dioxide and generate heat. The heat would be used to drive chemical reactions between the collected carbon dioxide and hydrogen carried from Earth. The products of the PPIMO system would then be used to re-fuel a rocket propulsion system. Lamamy concluded that utilizing PPIMO with a chemical propulsion system offers a practical benefit over an electric propulsion system when a short trip duration is required [25].

1.2.3 Recent Work

The early studies previously described focused on determining the appropriate performance parameters for air-accumulating vehicles. They especially noted the requirements for the power and propulsion systems that would make such a system economically advantageous. Notably, most of these concepts relied on the availability of multi-megawatt-class nuclear power sources in LEO. Although on-orbit nuclear power solutions are technically feasible with current technology, it is generally known that current social and political obstacles are sufficient to eliminate the possibility of employing a large nuclear power source on orbit. Thus, most current research has focused on air-breathing applications for smaller satellites. Some work has focused on designing an efficient inlet/collection scheme [26]. Others around the world are currently investigating thruster concepts that may have the appropriate performance characteristics when operating with atmospheric constituents [27–29].

Timothy Pigeon and Ryan Whitaker, two undergraduate students at the Massachusetts Institute of Technology, analyzed the potential for a "Near-Vacuum Hall Thruster," that would ingest ambient gas and accelerate it using the Hall effect. Initial experiments suggested that the thruster may work [30], but later experiments by Omar Bashir and Regina Sullivan measured properties in the exhaust plume that indicated the performance at all operating conditions would be far too low to compensate for satellite drag at the altitudes of interest [31].

Two similar concepts were introduced by Gordon Dressler of the Northrop Grumman Corporation [32], and Leonid Pekker of ERC Incorporated with Michael Keidar of George Washington University [33]. Dressler's concept, called the "Ambient Atmosphere Ion Thruster," used an open set of grids to electrostatically accelerate ambient gas that is already ionized, without needing any sort of scooping structure. Dressler's work did not address some of the more challenging technical details of the concept, including the mechanism for thrust production. Pekker and Keidar presented a thorough model of a similar concept

that uses a Hall accelerator instead of grids. They came to the conclusion that the concept could work at 80–90-kilometer altitudes with megawatts of power. However, Pekker and Keidar used optimistic assumptions for some of the characteristics of Hall thrusters in their calculations [33].

Kazutaka Nishiyama of JAXA noted that scientists do not currently have access to the region of the atmosphere at altitudes of 60–200 kilometers. He proposed using an Air-Breathing Ion Engine (ABIE), to compensate for the drag of a satellite in a 150–200-kilometer orbit in order to study the atmosphere at those altitudes for a mission duration of at least several months. Nishiyama stated that an efficient air inlet design is the key to making the concept viable, and that the inlet materials must be resistant to degradation when interacting with atomic oxygen. He determined reasonable characteristics for a small satellite mission, with a 4.1–5.6-kilowatt ion engine providing the thrust at a specific impulse of 7,300–10,000 seconds. His work also identified many of the engineering challenges that must be overcome to make this concept a reality [34].

Following from Nishiyama's work, Masahito Tagawa et al. created a fast atomic oxygen source to simulate the environment that the ABIE would experience on orbit [35]. The experiment indirectly measured the thrust produced from an ABIE-like set of grids. The authors noted that the experiment was fundamentally different than operation in LEO because the atomic oxygen source was pulsed, rather than steady-state. This led to the development of a steady-state atomic oxygen source capable of testing a small-scale ABIE in an environment representative of the very low LEO atmosphere [29].

In 2010, Jones et al. revived Demetriades's PROFAC work, and presented a concept called Propellant Harvesting of Atmospheric Resources in Orbit (PHARO). The proposed PHARO mission was a propellant depot that would collect 300 metric tons of oxygen from the Earth's atmosphere during one year of operation. The PHARO vehicle would then load the collected oxygen onto a Mars-transfer vehicle. Jones's work mainly presented the Direct Simulation Monte Carlo (DSMC) analysis of various inlet designs, with computa-

tional results for the continuum-rarefied transitional flow regime at about 100 kilometers. The study determined that the propulsion system must be capable of providing at least 134 newtons of thrust at a minimum 1000-second specific impulse. The authors suggested that the high thrust required could be distributed among multiple vehicles or engines [36].

DiCara et al. also presented DSMC results of an inlet design, along with a reasonable mission concept for using a "RAM-EP" propulsion system. The authors gave a very detailed description of a proposed demonstration mission that mostly uses off-the-shelf technology. The study determined that a mission is possible down to an altitude of 180 kilometers, and that the RAM-EP concept is only advantageous at altitudes below about 250 kilometers. For the designed demonstration mission, the thrusters would need to provide 2–20 millinewtons of thrust with approximately 1 kilowatt of electrical power. The authors noted that both the inlet design and thruster performance with atmospheric gases must be verified before further system development can occur [27].

Other studies have focused specifically on using or modifying existing thruster technologies in air-breathing applications. Kevin Diamant of the Aerospace Corporation experimentally studied a two-stage thruster concept designed to have a very long lifetime [37]. Diamant's experiments used xenon propellant, and the results suggested that there was no advantage to using a two-stage thruster design over a more traditional Hall thruster. David Kirtley of MSNW LLC plans to use a Field Reversed Configuration (FRC) thruster concept with neutral flow entrainment to achieve the appropriate performance characteristics for an air-breathing propulsion system [28]. Recent measurements suggest that the FRC technology shows promise, and future testing is planned for use with Mars and Earth atmospheric propellants, as well as materials possibly found in asteroids [38]. However, no direct performance measurements are yet available to assess the applicability of FRC technology.

In addition to the work presented at academic conferences and in peer-reviewed journals, two patents have been awarded by the United States Patent and Trade Office in the past decade regarding air-breathing space propulsion technology. One is for an "air breath-

ing electrically powered hall effect thruster," which is similar to the concepts described by Pigeon and Whitaker, and by Pekker and Keidar [39]. The other patent is for an "air-breathing electrostatic ion thruster," which is most similar to the thruster concepts described by Nishiyama and Dressler [40].

1.3 Research Goals

Two unknowns are frequently cited in literature regarding the feasibility of air-breathing spacecraft concepts: 1) the efficiency and 2) the performance characteristics of space propulsion systems operating with atmospheric gases. Another unknown that is not as frequently cited is the lifetime of these propulsion systems. This dissertation aims to address the feasibility and practicality of operating an air-breathing propulsion system on a small satellite in very low LEO with currently available technology. The approach taken is to choose the appropriate thrusters to test, and to directly measure their performance when operating with atmospheric propellant. Radio frequency (RF) plasma technology is used widely in the multi-billion dollar semiconductor manufacturing industry. The ability of this technology to increase the performance of an air-breathing system is a major focus of the investigation.

Chapter 2 gives background information and the feasibility analysis used to determine the appropriate thruster technologies to test in the laboratory. Chapter 3 presents further information regarding RF plasma systems. Chapter 4 presents the designs of the thrusters, and Chapter 5 describes the facilities and diagnostics used to test the thrusters. Chapter 6 then presents the results of thruster performance testing, and Chapter 7 discusses the physics of thruster operation. Finally, Chapter 8 makes concluding remarks regarding the future application of these thrusters to a satellite mission employing an air-breathing propulsion system.

CHAPTER 2

Background

This chapter addresses the feasibility of using Earth's atmosphere as propellant for drag compensation. The results of the feasibility analysis are then used to determine the appropriate thruster concepts to investigate. First, the properties of Earth's atmosphere in very low LEO are described. Then, the propulsion requirements of an air-breathing system are presented. A reference mission is then defined to generate representative values for a small demonstration spacecraft that uses currently available technology. Finally, the decision of the appropriate thruster technology to investigate is made.

2.1 Earth's Atmosphere

The NRLMSISE-00 model is a standard global atmospheric model used by NASA in the range of altitudes from 0–1000 kilometers above the Earth's surface. The "NRL" indicates that the model was published by the United States Naval Research Laboratory. The "MSIS" stands for *Mass Spectrometer and Incoherent Scatter*, the "E" denotes that the model extended the MSIS-86 model into the middle and lower thermosphere, and "00" indicates that it was released in the year 2000. It is an empirical model based on mass spectrometry and incoherent scatter radar measurements taken by satellites and ground stations, as well as supplemental data from sounding rocket experiments and space shuttle flights. A website supported by NASA's Goddard Space Flight Center provides the mass density,

temperature, and gas composition of the atmosphere versus altitude according to the previously released MSISE-90 model [41].

Atmospheric conditions vary by altitude, latitude, longitude, and over the course of a day/night cycle, the yearly seasonal cycle, and the solar cycle (approximately an 11-year period). To assess the feasibility of an air-breathing system, the NRLMSISE-00 data is taken from the Draft International Standard atmosphere for low, mean, and high solar and geomagnetic activity [42]. The values used for the atmospheric properties are given in Appendix A. Although many of the properties may affect the required performance of an air-breathing propulsion system, one of primary importance is the mass density of the gas, plotted in Fig. 2.1.

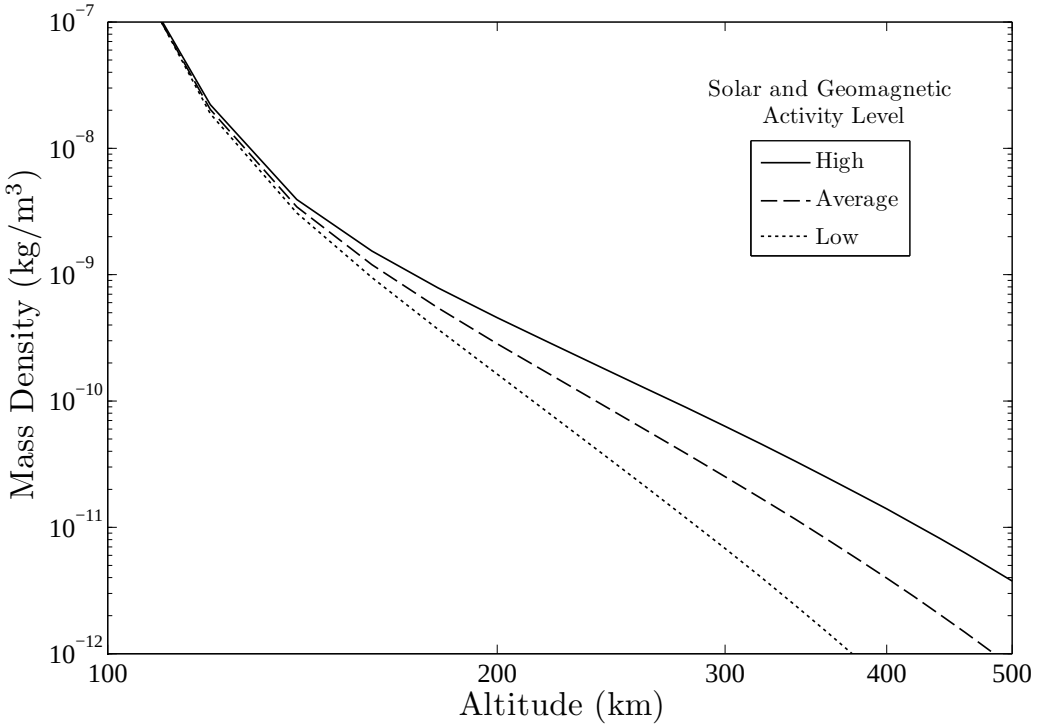

Figure 2.1: Mass density of atmospheric gas versus altitude from the NRLMSISE-00 model at different levels of solar activity, from Draft International Standard ISO/DIS 14222 [42]. Solar and geomagnetic activity may vary over time scales as short as an hour and as long as a decade.

Atmospheric composition is also important when considering the development of an air-breathing spacecraft. Argon, helium, and molecular nitrogen are inert. However, atomic oxygen and hydrogen are very reactive, and they can cause increased erosion of space-

craft materials. Candidate methods of propulsion must be able to effectively use the atmosphere's constituent gases as propellant. For example, even though atomic oxygen is the majority component of the upper atmosphere, as shown in Fig. 2.2 [42], Zukerman calculated that an atomic oxygen-recombination ramjet would have insufficient performance to compensate for drag [19].

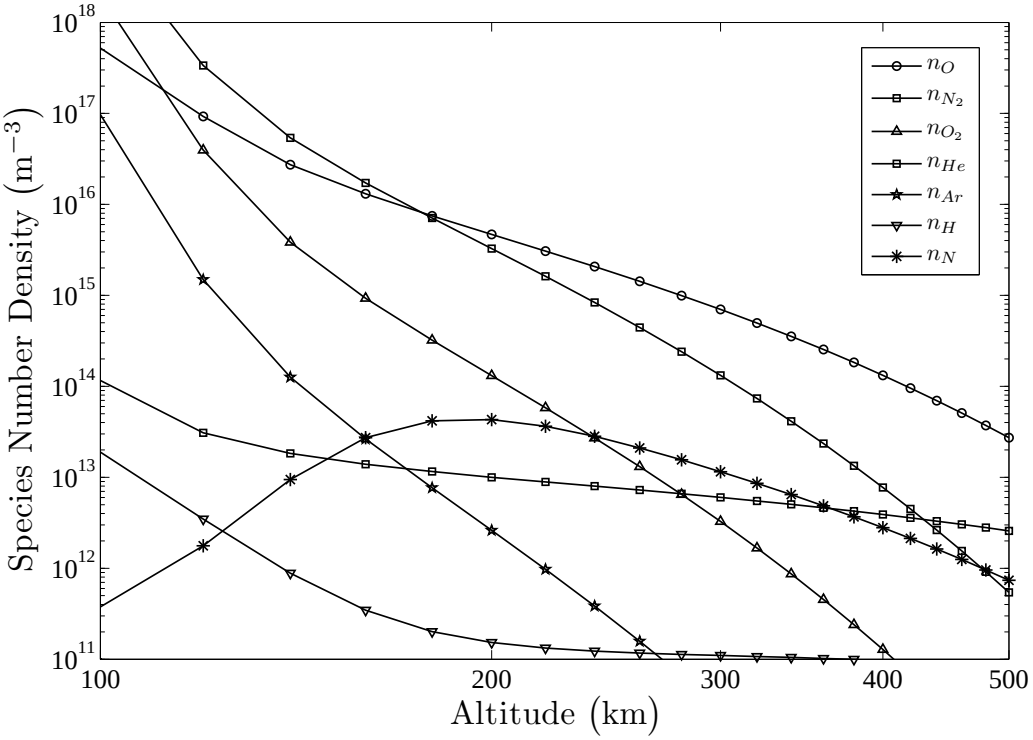

Figure 2.2: Number density of atmospheric constituents versus altitude at mean solar and geomagnetic activity. Data are from the NRLMSISE-00 model, given by Draft International Standard ISO/DIS 14222 [42]. Atomic oxygen is the majority component above about 200 km.

2.2 Kinetic Theory

Kinetic theory is a description of macroscopic gas behavior that treats the gas as a collection of individual microscopic particles, or molecules. The individual molecules are in a constant state of motion, and they interact with material surfaces and other molecules in the gas through frequent collisions [43]. The average distance that a molecule will travel before it collides with another molecule is called the *mean free path*, λ_{mfp}. To describe the

macroscopic behavior of the gas in a real system, an important non-dimensional quantity for Kinetic theory is the *Knudsen number*, *Kn*. The Knudsen number is the ratio of the mean free path of the molecules to the length scale of the system. The systems analyzed in this dissertation are spacecraft, and so the length scale used to calculate the Knudsen number is the characteristic length of the spacecraft, $L_{s/c}$, as shown in Eq. 2.1.

$$Kn = \frac{\lambda_{mfp}}{L_{s/c}}, \tag{2.1}$$

The Knudsen number gives the ratio of the length scale that a molecule travels between microscopic interactions to the macroscopic length scale of the whole system. When the Knudsen number is greater than or equal to one, the gas behavior in the system is said to be in the *free-molecular* flow regime. In free-molecular flow, the material surfaces are not large enough to cause flow discontinuities to develop. Thus, shocks are not present, and the sound speed is not an important quantity for describing flow behavior.

In order to estimate the mass flow rate and drag of an air-breathing satellite, it is assumed that the behavior of the gas surrounding the satellite is in the free-molecular flow regime. This assumption is dependent on the specific atmospheric conditions and the size of the spacecraft being analyzed, and it is checked for all analyses presented. Because the satellite is in a free-molecular flow, simplified equations may be used to describe the interactions between the satellite and the atmosphere. The front surface of the spacecraft is modeled as a flat plate moving through a stationary gas. The gas is characterized by the mass of each molecule, m, the number density, n, and the temperature, T_g, as shown by Fig. 2.3. The ratio of the plate velocity, v_3, to the most probable thermal speed of the gas is known as the *speed ratio*, or s_3, and is defined in Eq. 2.2.

$$s_3 \equiv \frac{v_3}{\sqrt{\frac{2k_B T_g}{m}}} \tag{2.2}$$

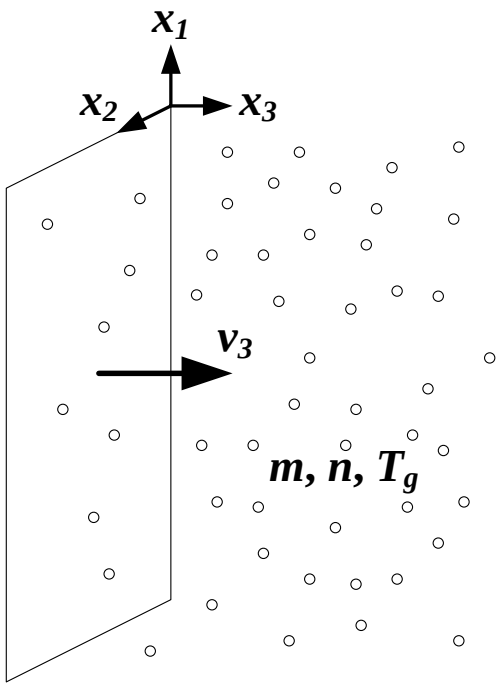

Figure 2.3: Kinetic theory description of a flat plate moving through ambient gas.

Assuming that the ambient gas has a Maxwellian energy distribution, Eqs. 2.3 and 2.4 give the solutions to the Boltzmann relations for incident mass flux, Φ_3, and momentum flux, P_3, on the flat plate, respectively. Note that the speed ratio, s_3, is the critical parameter for determining the asymptotic solutions to Eqs. 2.3 and 2.4.

$$\Phi_3 = \frac{1}{4} mn \left(\frac{8 k_B T_g}{\pi m} \right)^{1/2} \left[\exp\left(-s_3^2\right) + \sqrt{\pi} s_3 \left(\text{erf}(s_3) + 1 \right) \right] \tag{2.3}$$

$$P_3 = n k_B T_g \left[\frac{s_3}{\sqrt{\pi}} \exp\left(-s_3^2\right) + \left(\frac{1}{2} + s_3^2 \right) \left(1 + \text{erf}(s_3) \right) \right] \tag{2.4}$$

As will be discussed later, the orbital velocity of the satellite is used as the plate velocity in the kinetic theory model of the air-breathing system. At the altitudes of interest for an air-breathing spacecraft, the speed ratio is always greater than 8. This is sufficiently large for the asymptotic solutions to Eqs. 2.3 and 2.4 to apply. Thus, the spacecraft front surface is in free-molecular flow, and the mass and momentum flux to the front surface are given

by Eqs. 2.5 and 2.6, respectively, where m is the mass of each molecule in the surrounding gas, n is the number density of the surrounding gas, and v_3 is the normal velocity of the spacecraft relative to the surrounding gas.

$$\lim_{s_3 \to \infty} \Phi_3 = mnv_3 \tag{2.5}$$

$$\lim_{s_3 \to \infty} P_3 = mnv_3^2 \tag{2.6}$$

2.3 Propulsion Systems

Satellites employ propulsion systems to exert a force for the purposes of orbit maintenance, attitude control, and/or orbit raising. According to Newton's third law, any force exerted on a mass (i.e. an *action*) causes a force equal in magnitude and opposite in direction to another mass (i.e. a *reaction*). Propulsion systems near the Earth's surface, such as boat or airplane propellers, can use the atmosphere as reaction mass by "pushing" against the surrounding water or air. The atmospheric density a few tens of kilometers above Earth's surface is too low for these types of propulsion systems to effectively "push" against. At such high altitudes, the vehicle normally carries all of the reaction mass on board.

2.3.1 Rocket Propulsion

A propulsion system that uses no external sources of reaction mass is called a *rocket*, and the stored reaction mass is called the *propellant*. The force provided by a rocket is called the *thrust*, F_T, and it is equal to the rate at which propellant mass is expelled from the vehicle (the *propellant mass flow rate*), $\dot{m}_{pr}$, multiplied by the velocity of the expelled propellant relative to the vehicle (the *effective exhaust velocity*), v_{ex}, according to Eq. 2.7.

$$F_T = M(t)\frac{dv(t)}{dt} = \frac{dm_{pr}}{dt}v_{ex} = \dot{m}_{pr}v_{ex} \tag{2.7}$$

Note that both the mass, $M(t)$, and the velocity, $v(t)$, of the vehicle are functions of time. As shown in Fig. 2.4, the stored propellant mass is expelled from the vehicle, and the vehicle is accelerated in the opposite direction by the thrust force. The effective exhaust velocity is a physical property of the particular type of rocket that is used.

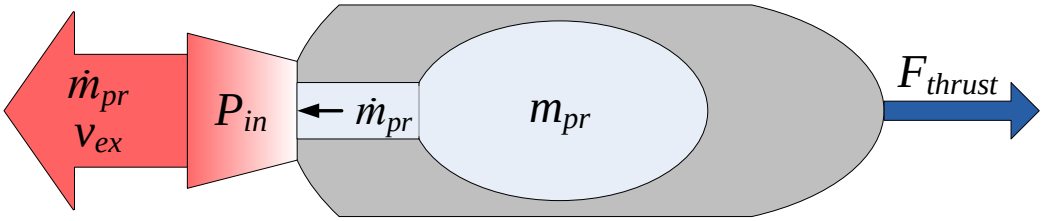

Figure 2.4: Diagram of rocket operation.

The initial mass of the vehicle is given as M_0. The flow rate and effective exhaust velocity are assumed to be constant. Thus, the mass of the vehicle decreases linearly with time, as shown by Eq. 2.8.

$$M(t) = M_0 - \dot{m}_{pr}t \tag{2.8}$$

Because a real vehicle may only carry a finite amount of propellant, m_{pr}, all of the propellant mass will eventually be expended after the *total burn time*, t_b. The vehicle mass remaining after the propellant is expended is the final mass of the vehicle, M_f, as shown by Eq. 2.9.

$$M(t_b) \equiv M_f = M_0 - \dot{m}_{pr}t_b \tag{2.9}$$

Equation 2.7 can then be rewritten as Eq. 2.10, where v_0 is the initial vehicle velocity and v_f is the final vehicle velocity.

$$\int_{M_0}^{M_f} \frac{dM'}{M} = \frac{1}{v_{ex}} \int_{v_0}^{v_f} dv' \tag{2.10}$$

Carrying out the integration yields Eq. 2.11. Equation 2.11 was originally published by Russian schoolteacher Konstantin Eduardovich Tsiolkovsky in 1903 [44], and it is still commonly referred to as "the rocket equation."

$$\frac{M_f}{M_0} = e^{-\frac{\Delta v}{v_{ex}}} \tag{2.11}$$

The maneuver that the rocket pushes the vehicle through defines the "delta-vee" required, Δv. This is the change in velocity imparted to the final vehicle mass when $M_0 - M_f$ amount of propellant mass is consumed. Note that for a given Δv (i.e. vehicle maneuver), a rocket with a higher effective exhaust velocity requires less propellant mass to complete the maneuver.

The thrust integrated over the entire burn time of the rocket represents the total momentum change that the propulsion system can impart to the vehicle, and it is called the *total impulse*. A commonly cited figure of merit for rocket systems is the *specific impulse*, I_{sp}, which is the impulse imparted to the spacecraft per unit weight of propellant. This quantity is defined in Eq. 2.12, where g_0 is the acceleration due to gravity at sea level on Earth. Specific impulse is a measure of how effectively the rocket system uses the propellant mass.

$$I_{sp} \equiv \frac{\int_0^{t_b} F_T(t')dt'}{g_0 \int_0^{t_b} \dot{m}_{pr}(t')dt'} \tag{2.12}$$

If the average values of thrust and flow rate are determined for the entire burn time, then calculating the specific impulse is equivalent to determining the average effective exhaust velocity, as shown by Eq. 2.13.

$$I_{sp} = \frac{\overline{F}_T}{g_0 \dot{m}_{pr}} = \frac{\dot{m}_{pr} v_{ex}}{g_0 \dot{m}_{pr}} = \frac{v_{ex}}{g_0} \tag{2.13}$$

Assuming that it is initially stationary on the vehicle, some source of potential energy (e.g. gas pressure, chemical bond energy, electric potential energy, etc.) must be converted to kinetic energy in order to accelerate the propellant to the exhaust velocity. The power contained in the rocket exhaust that contributes to the thrust is called the *jet power*, P_{jet}, and it can be defined using different characteristics of the rocket, as shown by Eq. 2.14.

$$P_{jet} = \frac{1}{2}\dot{m}_{pr}v_{ex}^2 = \frac{1}{2}F_T v_{ex} = \frac{1}{2}F_T g_0 I_{sp} = \frac{1}{2}\dot{m}_{pr}(g_0 I_{sp})^2 \tag{2.14}$$

No matter what the original source of energy is, the *total efficiency*, η_{tot}, of a rocket can be defined by the fraction of the input power, P_{in}, that is converted to jet power, as shown in Eq. 2.15.

$$\eta_{tot} \equiv \frac{P_{jet}}{P_{in}} = \frac{P_{jet}}{P_{chemical}}, \text{ or } \frac{P_{jet}}{P_{electrical}}, \text{ or } \frac{P_{jet}}{P_{nuclear}}, \text{ etc.} \tag{2.15}$$

Rockets can be categorized by the source of power used to generate thrust. One fundamental categorization of rocket types is the distinction between chemical and electric rockets. Chemical rockets use only the internal energy that is contained in the propellant itself. This internal energy can be stored as a high pressure or as chemical bonds in the propellant molecules. Once the chemical energy is released, the propellant flows through a nozzle to convert the isotropic thermal energy into a directed exhaust jet. Electric rockets instead use an electrical power source to add energy to the propellant. Depending on the method for electrical energy input, a nozzle may or may not be used. Figure 2.5 shows the operating regimes for the different types of rockets.

The input power for chemical propulsion systems is fundamentally limited by the density of the internal energy stored in the propellant. The maximum specific impulse is limited by the temperature that the propellant combustion products can attain and the efficiency of the nozzle. For example, unavoidable "frozen flow" losses (losses due to the propellant molecules carrying internal energy into the exhaust) prevent all of the chemical bond energy from being converted into directed kinetic energy that produces thrust. The practical maxi-

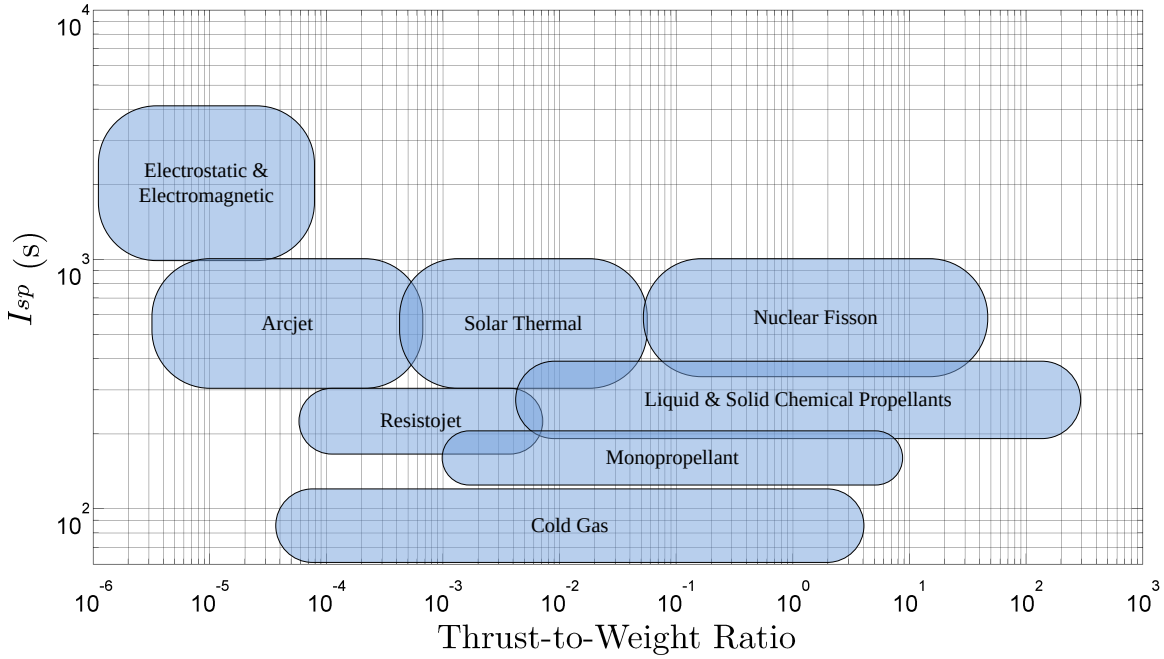

Figure 2.5: Operating regimes of different types of rockets [45].

mum specific impulse in modern chemical rockets is approximately 450 seconds, which is attained by using liquid oxygen and liquid hydrogen as propellant. Higher specific impulse has been demonstrated with more energetic propellant combinations (e.g. 532 seconds in a lithium-fluorine-oxygen rocket [46]). These exotic propellants are generally more difficult to handle or store, and the modest performance gains realized would not offset the large development costs required to make these propellants viable [47].

2.3.2 Air-Augmented Rocket Propulsion

The previous analysis applies specifically to rockets, which by definition carry all propellant on board the vehicle. However, the same principles can be applied to a system that uses an external source of propellant. A chemical rocket typically requires both a fuel and an oxidizer to release the stored chemical energy. In Earth's lower atmosphere, oxygen is available at high enough densities such that the air can be used as an oxidizer. Thus, the fuel stored on the vehicle can be reacted with the air in either a *duct jet* propulsion system (e.g. ramjet, turbojet, etc.) or a *ducted rocket* or *air-augmented rocket*, as shown in Fig. 2.6.

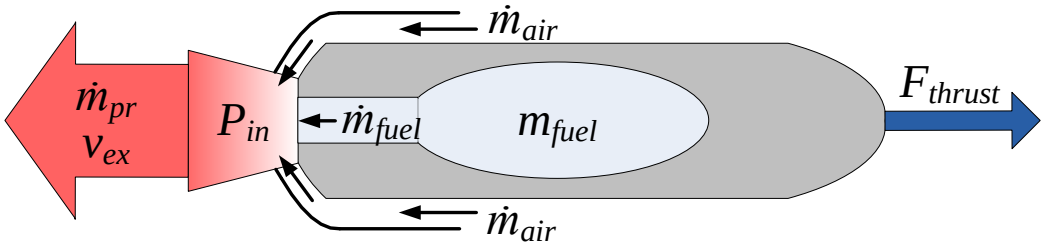

Figure 2.6: Diagram of ducted or air-augmented rocket operation.

Because this type of vehicle uses ambient gas as propellant, the equation for specific impulse is modified. For a constant total propellant flow rate, Eq. 2.16 applies, where $\dot{m}_{fuel}$ is the mass flow rate of stored fuel, and $\dot{m}_{air}$ is the mass flow rate of collected air.

$$\dot{m}_{pr} \equiv \dot{m}_{fuel} + \dot{m}_{air} \tag{2.16}$$

In an air-augmented rocket, both the fuel and air contribute to the thrust, but only fuel is expended from the vehicle. Thus, by substituting Eq. 2.16 for the propellant flow rate in Eq. 2.13, the specific impulse of an air-augmented rocket can be written as Eq. 2.17.

$$I_{sp} = \frac{(\dot{m}_{fuel} + \dot{m}_{air})v_{ex}}{g_0 \dot{m}_{fuel}} = \frac{v_{ex}}{g_0}\left(1 + \frac{\dot{m}_{air}}{\dot{m}_{fuel}}\right) \tag{2.17}$$

Equation 2.17 shows that the specific impulse of a propulsion system can be drastically increased if a significant amount of the propellant can be drawn from the vehicle surroundings, and if the exhaust velocity is not significantly diminished. This is the reason why commercial airplanes use turbofan engines instead of rockets. It also explains why there is a considerable research effort dedicated to replacing rocket propulsion with ramjet and scramjet engines for endo-atmospheric missions. However, previous work has shown that a purely air-breathing chemical rocket is not feasible in orbit, and that an augmented chemical rocket is not practical for orbital applications [19].

2.3.3 Electric Propulsion

Electric Propulsion (EP) refers to rocket systems that convert electrical energy into kinetic energy of the propellant. The source of electrical energy is external to the propellant, and so the exhaust velocity is not fundamentally limited by the internal energy that can be stored in the propellant. EP can be further sub-divided into categories based on the physical process that converts the electrical energy to jet power of the propellant. The three categories are described below, and a comparison of typical performance parameters is given in Table 2.1

1. **Electrothermal** Thrusters operate by heating propellant, and expanding it through a nozzle. Examples of electrothermal propulsion include resistojets and arcjets.

2. **Electrostatic** Thrusters operate by ionizing the propellant, and accelerating the ion species to high velocity with an applied electric field. Examples of electrostatic propulsion include gridded ion thrusters, Hall/Stationary Plasma Thrusters (SPTs), and colloid thrusters.

3. **Electromagnetic** Thrusters operate by ionizing and driving electrical current through the propellant. The driven current interacts with an applied magnetic field to accelerate the ionized propellant. Examples of electromagnetic propulsion include Pulsed Plasma Thrusters (PPTs), Magnetoplasmadynamic thrusters (MPDs), Pulsed Inductive Thusters (PITs), and Field-Reversed Configuration Thrusters (FRCs).

A plasma is an ionized gas that can experience body forces due to applied electric and magnetic fields. It logically follows that electrostatic and electromagnetic EP systems employ the use of plasmas. The exhaust velocities of these systems are set by the strength of the applied fields. The thrust force is transmitted to the thruster through the fields themselves. This implies that the ionized propellant does not need to collide with any thruster components to exert a force on the vehicle. However, some of the fast-moving molecules do collide with the thruster, causing the erosion of materials and limiting thruster lifetime.

Table 2.1: Electric propulsion performance characteristics [45, 48–52].

Type	Power (kW)	I_{sp} (s)	η_{tot} (%)	Life (hrs)	Status
Resistojet (N_2H_4)	0.5–1.5	300	80	500	Flight
Arcjet (N_2H_4)	0.3–2	500–700	35	$>$ 1,000	Flight
Arcjet (H_2)	0.005–100	1000–1500	25–40	—	R & D
Hall Thruster (Xe)	0.1–50	1000–3000	40–70	$>$ 7,000	Flight
Hall Thruster (Kr)	1–74	1500–4500	30–65	—	R & D
Ion Thruster (Xe)	0.2–40	2000–10000	60–75	$>$ 40,000	Flight
MPD (NH_3, H_2, Ar)	0.001–4000	2000–5000	30–50	—	R & D

As will be discussed in the next section, if a satellite uses propellant only from the collection of ambient atmospheric gas, then the minimum specific impulse required from the propulsion system to sustain the satellite in a 200-kilometer orbit is approximately 800 seconds. In addition, for an air-breathing satellite to yield a practical benefit over a non-air-breathing satellite, the propulsion system must have an operating lifetime of at least 30,000 hours. The combination of these two requirements eliminates resistojets and arcjets for consideration in an air-breathing system.

Table 2.1 shows that Hall thrusters are not be capable of operating for the long lifetime required to make the air-breathing system practical. However, recent research suggests that Hall thrusters can be designed to dramatically increase Hall thruster lifetime. This can be accomplished either by continuously replenishing the eroded thruster materials or by altering the magnetic field geometry. The High Voltage Hall Thruster program at the NASA Glenn Research Center has demonstrated that the material replenishment concept can extend thruster lifetime beyond 15,000 hours [53]. The operation of a Hall thruster in a "magnetically-shielded" configuration at the Jet Propulsion Laboratory demonstrated that material erosion rates can be reduced by three orders of magnitude [54]. This could extend the lifetime of a magnetically-shielded Hall thruster to the order of 1,000,000 hours [55].

Although electric propulsion systems can generally operate with different propellants, the choice of a propellant can affect the overall thruster performance. For example, Table 2.1 shows how the operation of an arcjet can change when operating with hydrazine

(N_2H_4) versus hydrogen (H_2) propellant. In addition to altering performance characteristics, using different propellants can affect the thruster material compatibility. Hall thrusters and gridded ion thrusters are life-limited due to the erosion of thruster materials. These thrusters are generally designed to operate with xenon propellant, and preliminary experiments suggest that erosion rates are increased when operating with oxygen propellant [56]. Ion thrusters have been successfully operated on the Gravity field and steady-state Ocean Circulation Explorer (GOCE) satellite at low orbit altitudes where there is a significant amount of atomic oxygen [57]. However, the performance of ion and Hall thrusters operating with nitrogen and oxygen propellant is not well-documented.

2.4 Air-Breathing Spacecraft

Air-breathing space propulsion is an enabling technology that could allow a spacecraft to perform propellant-expensive maneuvers at low orbit altitudes without suffering a reduction in the payload mass or lifetime. At a minimum, the air-breathing propulsion system must be capable of compensating for drag. It is important to quantify the altitudes where this is possible, and the practical benefit that an air-breathing system might achieve over a non-air-breathing system. This section describes the procedure used to calculate the performance requirements of the propulsion system.

First, it is important to understand the properties of a non-air-breathing spacecraft. In general, a spacecraft can be divided into three major sources of mass: the bus (i.e. the structure, wiring harness, communications subsystems, solar panels, etc.), the propellant, and the payload, given by Eq. 2.18.

$$M_0(h) = M_{bus} + m_{fuel} + M_{p/l} = M_0 \left(k_{bus} + k_{fuel} + k_{p/l}\right) \tag{2.18}$$

Although the payload requirements generally drive the properties of the spacecraft bus, the mass available as payload, $M_{p/l}$, is the most valuable to the customer. The total mass

delivered to a particular orbit, $M_0(h)$, is set by the launch vehicle, and is primarily a function of the orbit altitude and inclination. For a given launch vehicle, less total vehicle mass can be delivered to higher orbits.

The drag force, F_D, on a spacecraft in LEO is calculated according to Eq. 2.19, where ρ is the mass density of the atmosphere, $v_{s/c}$ is the spacecraft velocity, $A_{s/c}$ is the frontal area of the spacecraft, and C_D is the drag coefficient. For typical spacecraft, the drag coefficient is in the range of 2–4 [6].

$$F_D = \frac{1}{2}\rho v_{s/c}^2 C_D A_{s/c} \tag{2.19}$$

The lifetime of the satellite, τ_L, is calculated according to Eq. 2.20, assuming that the spacecraft ends its mission when all of the propellant has been expended. The drag, F_D, the propellant flow rate, $\dot{m}_{pr}$, and the specific impulse, I_{sp}, of the propulsion system are assumed to be constant.

$$\tau_L = \frac{m_{fuel}}{\dot{m}_{fuel}} = \frac{k_{fuel} M_0}{\frac{F_D}{I_{sp} g_0}} \tag{2.20}$$

If an electric propulsion system is used, and the thrust is exactly equal to the drag, then the electrical power required by the propulsion system, P_{req} may be calculated from Eq. 2.21.

$$P_{req} = \frac{1}{2\eta_{tot}} F_D I_{sp} g_0 \tag{2.21}$$

2.4.1 Model

The goal of the air-breathing spacecraft is to eliminate the need to store propellant onboard the spacecraft at launch (i.e. to reduce k_{fuel} in Eq. 2.18 to zero). The elimination of the stored propellant allows more spacecraft mass to be allocated to other systems, such as the payload. In addition, the on-orbit lifetime of the air-breathing propulsion system must not be significantly reduced in order for it to yield a practical benefit over a conventional propulsion system. Although alternative spacecraft geometries might be imagined

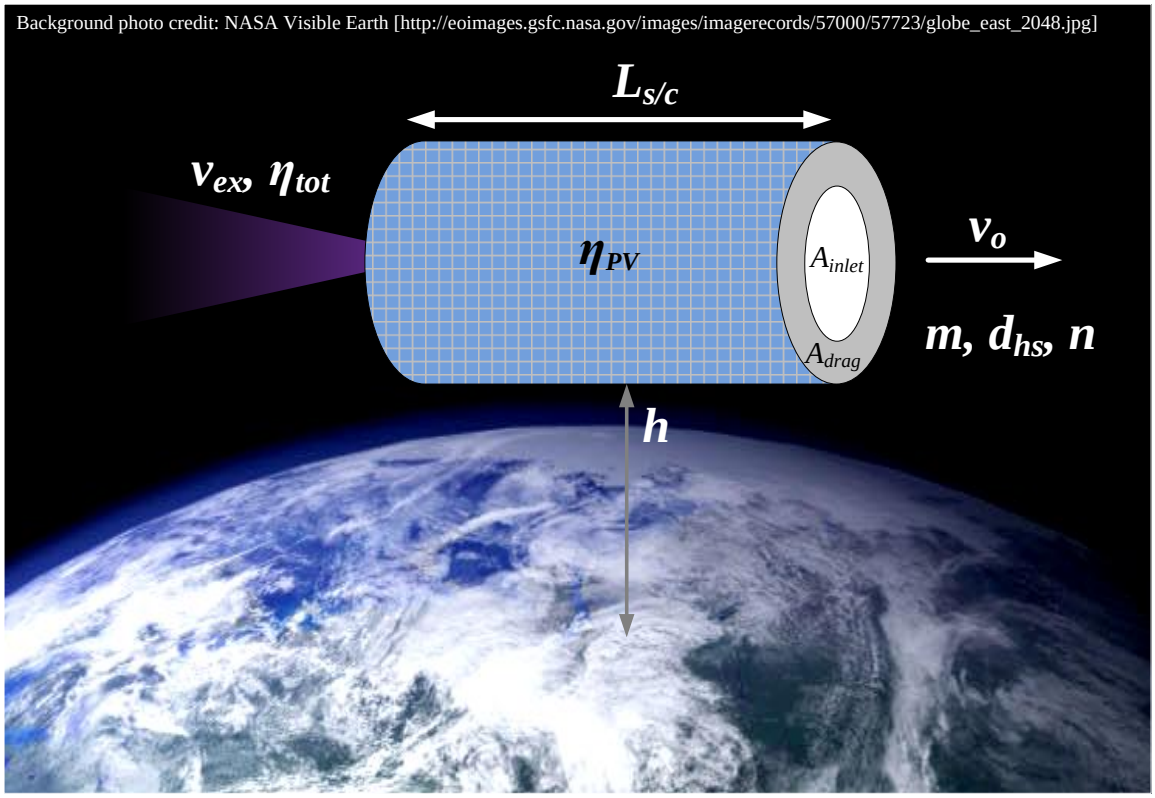

Figure 2.7: Notional diagram of an air-breathing satellite.

to optimize the capabilities of an air-breathing satellite, the model for a simple spacecraft is analyzed here to give a first-order estimate of the feasibility of creating an air-breathing spacecraft with current technology. Figure 2.7 shows a diagram of the simple air-breathing spacecraft analyzed, with important variables labeled. The procedure for determining the performance requirements of the air-breathing propulsion system is described below:

1. **Geometry:** The spacecraft geometry is assumed to have a well-defined length, $L_{s/c}$, and a surface area normal to the orbit trajectory, $A_{s/c}$. The normal surface area is divided into an inlet area, A_{inlet}, through which incident flow is collected, and a drag area, A_{drag}, which causes a drag force without collecting incident ambient gas.

$$A_{inlet};\ A_{drag};\ L_{s/c} \tag{2.22}$$

2. **Velocity:** The spacecraft is assumed to be in a circular orbit at an altitude, h, above the Earth's surface. The bulk velocity of the incident gas flow is equal to the spacecraft orbital velocity. Referring to the kinetic theory discussed above, the normal velocity, v_3 in Fig. 2.3, is the orbital velocity of the spacecraft, v_o in Fig. 2.7. Note that the radius of the Earth is approximately 6,378 kilometers, and that the altitudes of interest for an air-breathing spacecraft are in the range of roughly 100–400 kilometers. Thus, the Earth's radius is much larger than the orbit altitude, such that the orbit velocity is nearly constant (approximately 7.7–7.8 kilometers per second) in this altitude range.

$$v_o = \sqrt{\frac{\mathrm{G}M_\oplus}{R_e + h}} \tag{2.23}$$

3. **Flow Regime:** The gas behavior in the vicinity of the spacecraft is assumed to be in free-molecular flow, rather than a flow with transitional or hypersonic flow effects. To check that this assumption is valid, the Knudsen number, *Kn*, is calculated from the gas mean free path, λ_{mfp}, and the spacecraft length according to Eq. 2.1. To calculate the mean free path, the molecules of gas species k are treated as hard spheres characterized by a diameter $d_{HS,k}$. The number density of each gas species, n_k, is taken from the atmospheric data in the Draft International Standard ISO/DIS 14222 [42]. The mean free path is then determined from the number-density-weighted hard-sphere diameter of the atmospheric gas, $\overline{d_{HS}}$, according to Eq. 2.24. Thus, the Knudsen number is a function of gas composition as well as number density [58].

$$\lambda_{mfp} = \frac{1}{\sqrt{2}\pi \overline{d_{HS}}^2 \sum n_k}; \quad \overline{d_{HS}} \equiv \frac{\sum n_k d_{HS,k}}{\sum n_k} \tag{2.24}$$

4. **Mass Flow Rate:** It is assumed that the spacecraft operates in steady-state, such that the air-breathing propulsion system uses the gas that is incident on the inlet area as propellant. The incident mass flow, $\dot{m}_{in}$, is defined in Eq. 2.25 where the inlet efficiency, η_{inlet}, is the fraction of mass incident on the inlet area that is collected

by the spacecraft. A propulsion system that uses the maximum amount of gas flow requires a lower exit velocity to compensate for the drag. Thus, the spacecraft is assumed to used all of the collected mass flow as propellant in order to determine the *minimum* thruster exit velocity required.

$$\dot{m}_{in} \equiv nmv_o A_{inlet}\eta_{inlet} \tag{2.25}$$

5. **Drag:** The drag force, F_D, is calculated by treating the inlet area and drag area separately, and summing the force of the incident gas on each area. It is assumed that all of the gas molecules are initially at zero mean velocity (relative to the Earth). When collecting ambient gas, the spacecraft must accelerate all of the collected molecules to the orbital velocity. It is assumed that the gas molecules incident on the inlet area, whether collected or not, experience an average change in velocity equal to the spacecraft orbital velocity. For the drag area, it is assumed that incident molecules are elastically scattered by the spacecraft surface. Thus, the total change in momentum of the gas incident on the drag area is equal to twice the incident momentum (the most conservative assumption). The result of summing the force on the inlet and drag areas is given by Eq. 2.26. Note that this formulation is the same as choosing a drag coefficient in the range from 2 ($A_{inlet} \gg A_{drag}$) to 4 ($A_{drag} \gg A_{inlet}$), which is an appropriate range for a satellite in LEO with an elongated shape [59].

$$F_D = nmv_o^2 \left(2A_{drag} + A_{inlet}\right) \tag{2.26}$$

6. **Thruster Exhaust Velocity:** The minimum thruster effective exhaust velocity required is calculated by setting thrust equal to drag, and dividing by the inlet mass flow rate, as shown in Eq. 2.27. Note that this quantity is equivalent to the minimum

required specific impulse of the air-breathing thruster, since $v_{ex} = I_{sp} g_0$.

$$v_{ex} = \frac{F_D}{\eta_{inlet} \dot{m}_{in}} = \frac{v_o}{\eta_{inlet}} \left(2 \left(\frac{A_{drag}}{A_{inlet}} \right) + 1 \right) \tag{2.27}$$

An equivalent Direct Current (DC) acceleration voltage, V_{eq}, may also be determined from Eq. 2.28, assuming that there is no change in the composition of the propellant as it passes through the spacecraft. The average gas molecule mass, m, is calculated from the ISO/DIS 14222 data for species number densities, n_k, and from the species molecular masses, m_k.

$$V_{eq} = \frac{m v_{ex}^2}{2q}; \quad m \equiv \frac{\sum n_k m_k}{\sum n_k} \tag{2.28}$$

7. **Power Required:** The minimum electrical power that must be supplied to the propulsion system to compensate for drag, P_{req}, is calculated using the above relations and the total efficiency of the thruster, η_{tot}, according to Eq. 2.29.

$$P_{req} = \frac{\dot{m}_{in} v_{ex}^2}{2\eta_{tot}} = \frac{1}{2\eta_{tot}\eta_{inlet}} n m v_o^3 A_{inlet} \left(2 \left(\frac{A_{drag}}{A_{inlet}} \right) + 1 \right)^2 \tag{2.29}$$

8. **Spacecraft Power:** It is assumed that the spacecraft uses solar power in the form of photovoltaic cells that completely cover the cylindrical outer surface. The characteristic power available on the spacecraft, $P_{s/c}$, is then determined by the product of the insolation on orbit, the efficiency the photovoltaic cells, η_{PV}, and the photovoltaic area normal to the solar radiant flux. Assuming that the length of the spacecraft is always normal to the solar radiant flux, the normal photovoltaic area may be calculated using the inlet and drag area, the spacecraft length, and a geometric factor, k_G. For a cylindrical spacecraft geometry, $k_G = \sqrt{\pi} \approx 1.77$. In the vicinity of the Earth, insolation is approximately 1,367 watts per square meter [6], and so the characteristic spacecraft power may be calculated according to Eq. 2.30. Note that the photovoltaic

efficiency is not necessarily equal to the efficiency of a single cell. For example, even though Spectrolab's NeXt Triple Junction (XTJ) Solar Cells are 29.5% efficient [60], a solar panel smaller than 2.5 square meters using those cells only produces 345 watts per square meter, corresponding to a 25% efficiency [61].

$$P_{s/c} \approx 1367\,{}^{\mathrm{W}}/_{\mathrm{m}^2}\,\eta_{PV} k_G L_{s/c} \sqrt{A_{inlet} + A_{drag}} \tag{2.30}$$

9. **Feasibility:** The air-breathing feasibility parameter, Π_{AB}, is defined as the characteristic power of the spacecraft, $P_{s/c}$, divided by the power required for the air-breathing propulsion system, P_{req}, given by Eq. 2.31. A value of $\Pi_{AB} \geq 1$ is deemed to be feasible, and larger values of Π_{AB} represent margin over the minimum power required for the propulsion system. For a given spacecraft geometry, the feasibility parameter is primarily a function of altitude.

$$\Pi_{AB} \equiv \frac{P_{s/c}}{P_{req}} \tag{2.31}$$

2.4.2 Example

Based on the model given above, an example spacecraft is described. The example spacecraft is intended to be a "reasonable size" for a small air-breathing demonstration mission. This spacecraft is analyzed according to the procedure in the previous section to determine the altitudes where the air-breathing satellite can be operated, and the performance requirements for the air-breathing propulsion system. For simplicity, the spacecraft is assumed to have a cylindrically symmetric geometry.

The example spacecraft is designed to fit on a currently available launch vehicle, and for a small demonstration mission, the Pegasus launch vehicle manufactured by Orbital Sciences Corporation may be appropriate. The standard payload fairing for Pegasus is shown in Fig. 2.8 [8].

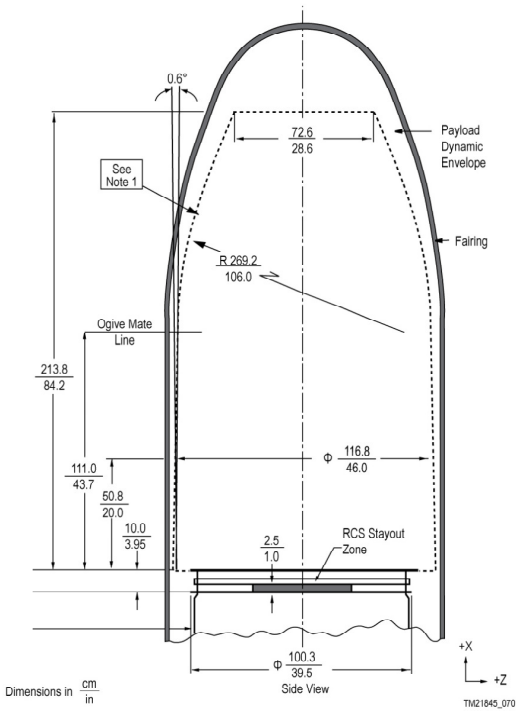

Figure 2.8: Pegasus® standard payload fairing [8].

To fit inside of the Pegasus payload fairing without requiring any moving parts, the example satellite has a 0.7-meter outer diameter and a 2.1-meter length. At this size, the spacecraft is in a free-molecular flow regime for altitudes above approximately 115 kilometers. The total frontal area of the spacecraft, $A_{drag} + A_{inlet}$, is equal to 0.385 square meters. The drag-to-inlet area ratio, A_{drag}/A_{inlet}, is arbitrarily chosen to be 0.5. The resulting example spacecraft is shown in Fig. 2.9. Note that a propellant tank is included because gas density on orbit fluctuates, and so the spacecraft may use the tank as ballast for the propellant supply. Recall that the outer surface of the spacecraft is assumed to be covered with solar cells for power generation.

The GOCE satellite is a similar size and shape as the example spacecraft, and operates down to an orbit altitude of about 260 kilometers. Information listed on GOCE's website states that GOCE produces 1300 watts of electrical power from a 9-square-meter solar array [62]. Assuming that a similar array can be used for the example air-breathing spacecraft mission, this gives an approximate value of 145 watts per square meter for a photovoltaic

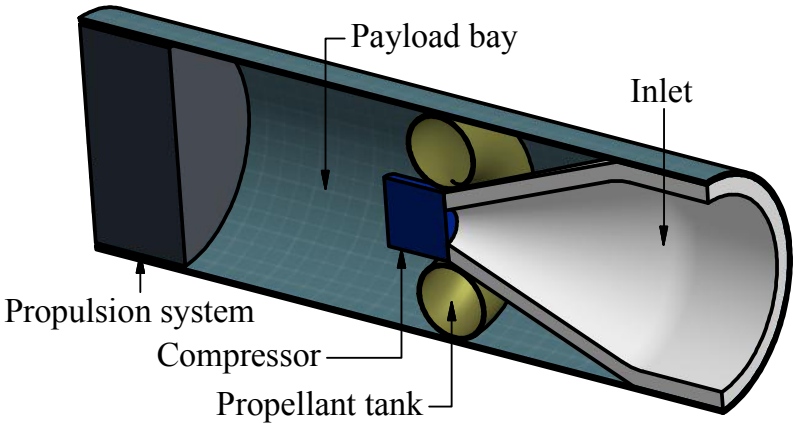

Figure 2.9: Cross-section of a notional air-breathing spacecraft, with $L_{s/c}$ = 2.1 meters, A_{drag}/A_{inlet} = 0.5, and a 0.7-meter outer diameter. The compressor moves air from the inlet to the propellant tank. Spacecraft volume allocated for a payload is shown. The propellant line from the tank to the propulsion system is not shown.

array in low-altitude LEO, corresponding to a 10.6% photovoltaic efficiency. This is a conservative estimate considering the 345-watts-per-square-meter capability of newer arrays produced by Spectrolab [61]. However, the specifications listed by GOCE are used due to their flight heritage near the altitudes of interest for an air-breathing spacecraft. Figure 2.10 shows an artist's rendering of the GOCE satellite operating in LEO.

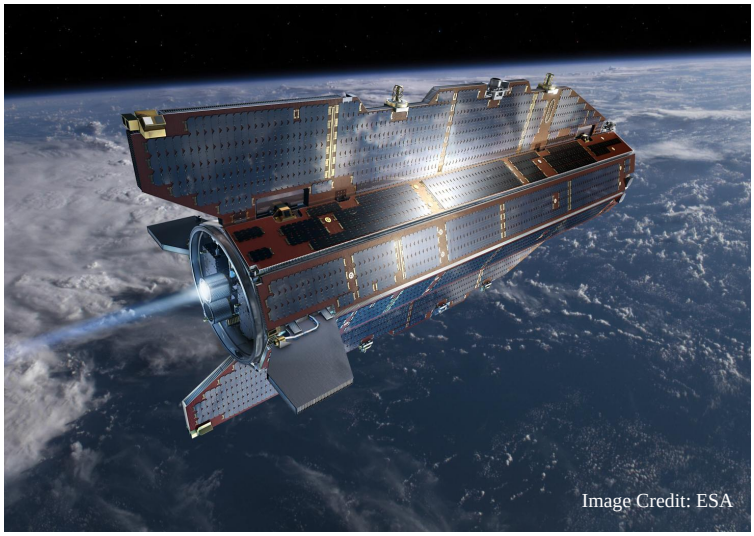

Figure 2.10: Rendering of the GOCE satellite during mission operations. GOCE is similar in size and shape to the example air-breathing spacecraft, and operates at an orbit altitude of 260 kilometers. GOCE continuously compensates for drag with a gridded ion thruster assembly that uses xenon propellant.

The results of the feasibility study taken with the example spacecraft properties are shown in Figs. 2.11 – 2.15. As expected, the drag increases significantly with decreasing altitude. Below about 150 kilometers, the drag is not strongly affected by solar and geomagnetic activity. For a mission at an altitude of 200 kilometers, the example air-breathing spacecraft would experience approximately 8.8 millinewtons of drag during periods of mean solar and geomagnetic activity, as shown in Fig. 2.11. To determine the performance requirements for the propulsion system, the thrust is set equal to the drag.

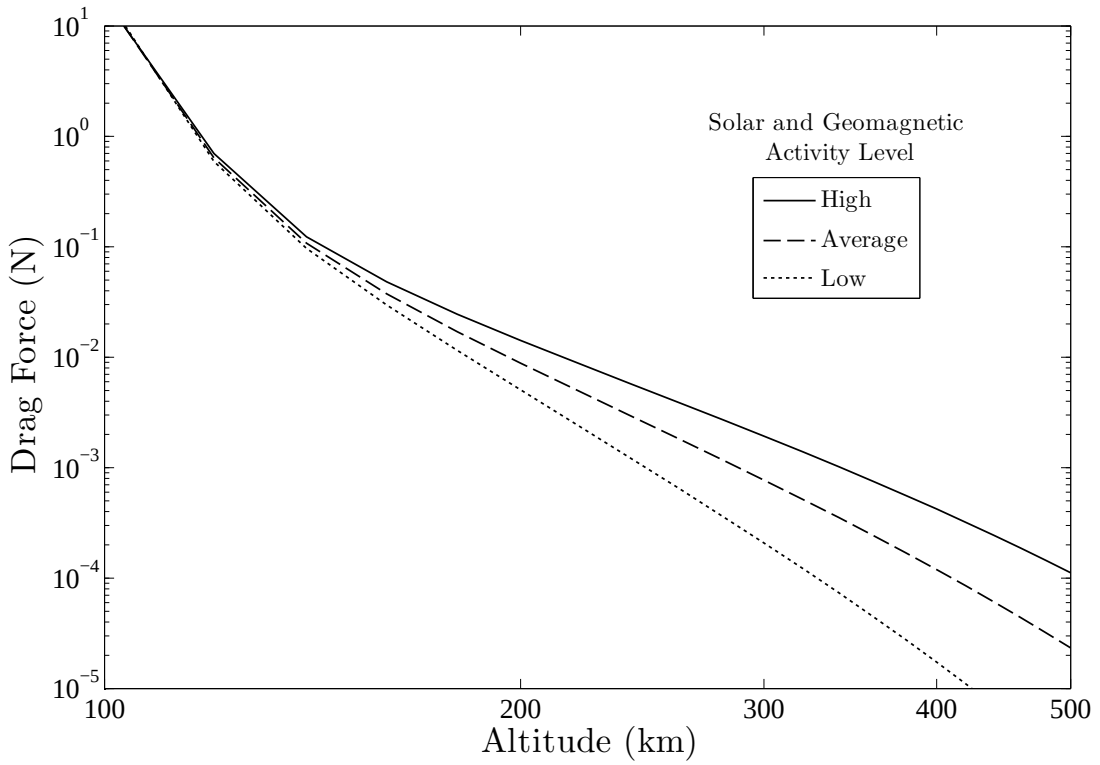

Figure 2.11: Drag on the example spacecraft. The thrust of an air-breathing propulsion system would need to be equal to the drag, which is roughly 1 to 100 millinewtons at altitudes of 300 to 150 kilometers, respectively.

The spacecraft inlet efficiency is assumed to be 0.90 (i.e. 90% of the gas molecules incident on the inlet area are collected). Figure 2.12 shows the inlet mass flow rate for the example spacecraft. The inlet mass flow rate follows a similar trend as the drag because both are linearly dependent on the atmospheric density, and because the orbital velocity

does not change significantly in this range of altitudes. In a 200-kilometer orbit, the example spacecraft collects 0.51 milligrams of atmospheric gas per second.

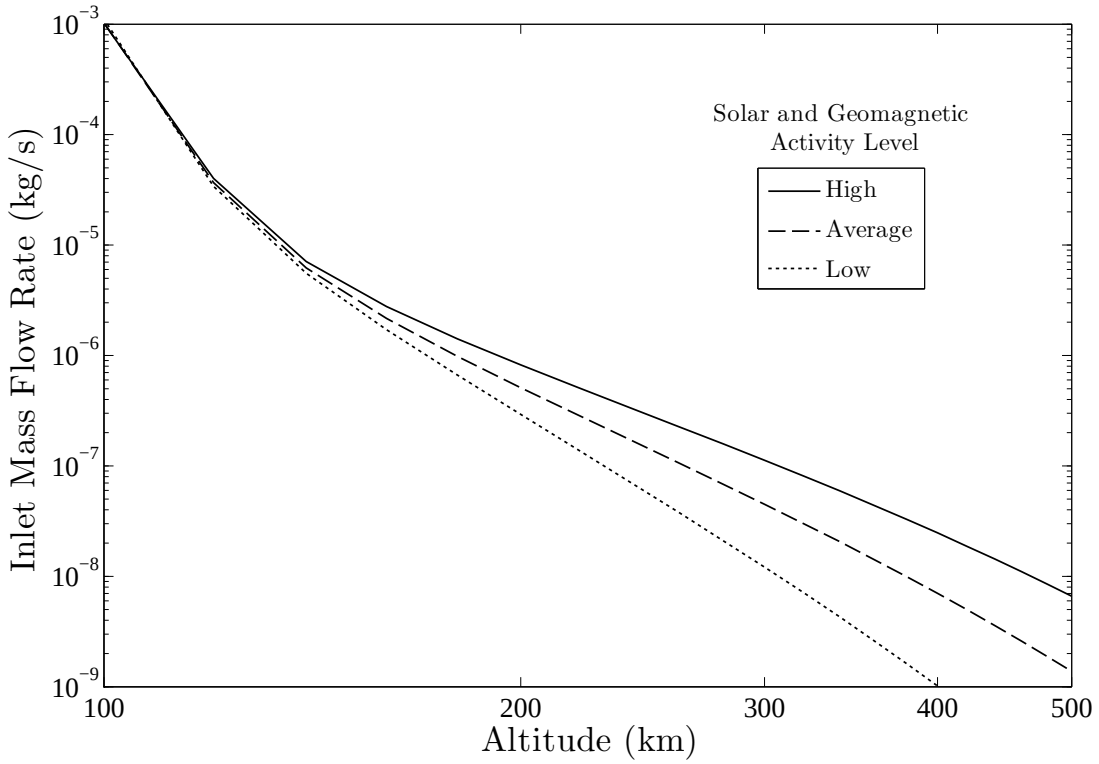

Figure 2.12: Mass flow rate for the example spacecraft. The inlet efficiency is assumed to be 0.9, and the inlet area is approximately 0.26 square meters. The inlet mass flow rate is in the 0.1 to 10 milligram-per-second range at altitudes from 300 to 150 kilometers, respectively.

The minimum specific impulse required from the propulsion system is determined from the drag and the mass flow rate. The results are plotted in Fig. 2.13. Note that the minimum specific impulse does not vary appreciably because it is primarily dependent on the fixed geometry of the spacecraft and the nearly constant orbital velocity. Thus, the minimum specific impulse required is also not affected by the level of solar and geomagnetic activity. The specific impulse is about 1750 $\pm$ 25 seconds at the altitudes of interest for an air-breathing spacecraft. At 200 kilometers, this corresponds to an equivalent DC acceleration voltage of approximately 33 volts for the average molecular mass of the atmosphere at that altitude.

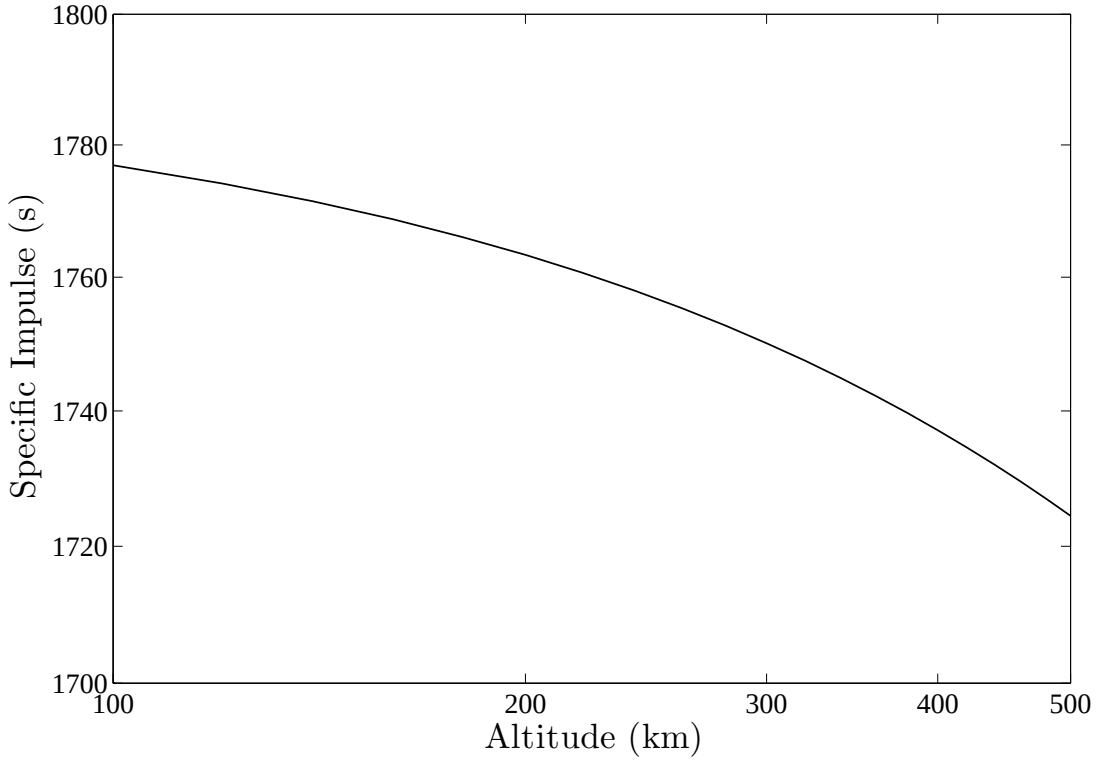

Figure 2.13: Minimum specific impulse required for the example air-breathing spacecraft propulsion system. The minimum specific impulse is only a function of the spacecraft geometry and the orbit velocity, and is therefore not affected by solar and geomagnetic activity.

The power required for the propulsion system to produce an amount of thrust equal to the drag is plotted in Fig. 2.14. Note that the power required is a function of the total efficiency of the propulsion system as well as the atmospheric properties. Thus, the level of solar and geomagnetic activity also affects the required power. The required power follows a similar trend as the drag and the mass flow rate. Thus, the power required for the air-breathing system is higher at lower altitudes because the drag increases significantly with decreasing altitude. At 200 kilometers, if the air-breathing propulsion system has a total efficiency of 0.25, then the example spacecraft must supply about 306 watts to the propulsion system in order to compensate for the drag.

The feasibility parameter is calculated from the power required to produce the thrust and the characteristic power of the example spacecraft. The results of the feasibility parameter

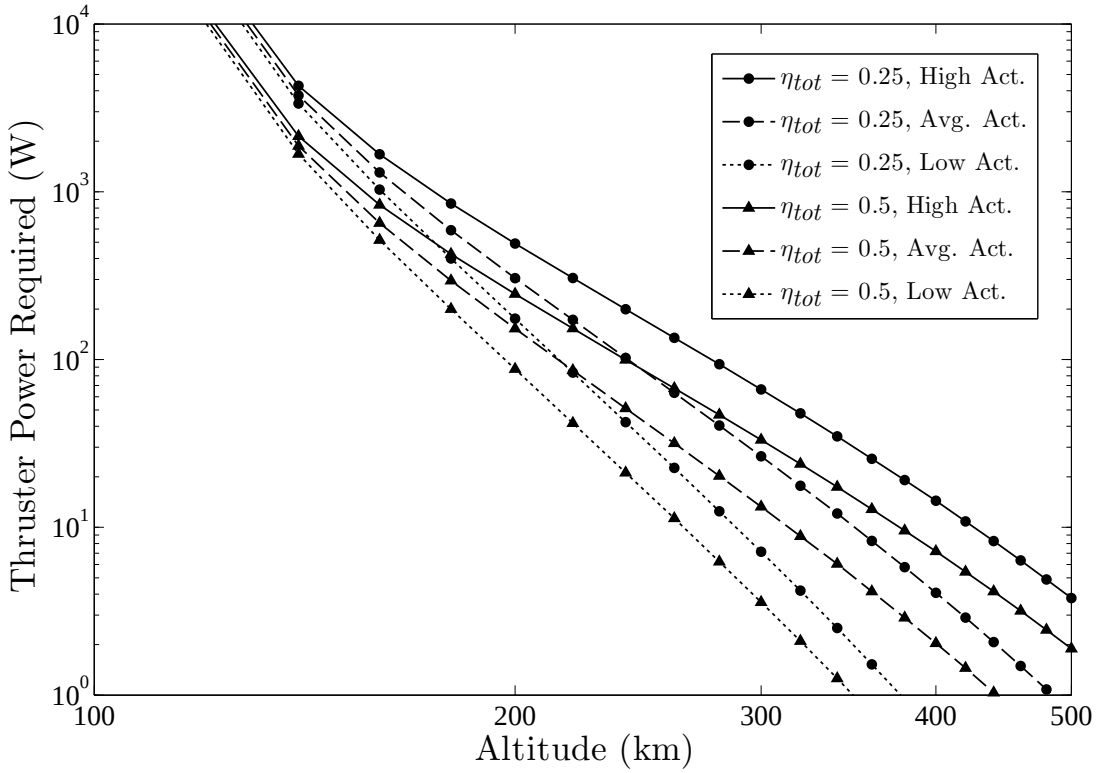

Figure 2.14: Power required for the example air-breathing propulsion system. Note that the power required is a function of both the thruster total efficiency and the level of solar and geomagnetic activity. For an η_{tot} =0.25, roughly 30 to 2000 watts are required at altitudes from 300 to 150 kilometers, respectively.

calculation are plotted in Fig. 2.15. Based on the geometry of the example spacecraft and the solar power generation properties of GOCE, the characteristic power of the spacecraft, $P_{s/c}$, is calculated to be about 334 watts. As stated above, the example air-breathing propulsion system would require approximately 306 watts of electrical power to operate at an altitude of 200 kilometers during periods of average solar and geomagnetic activity. Thus, the air-breathing spacecraft is deemed to be feasible in a 200-kilometer circular orbit if a propulsion system can be created with the previously described specifications.

As an aside, another performance metric for electric propulsion systems that is presented in the literature is the *thrust-to-power*. From the above model presented, the required thrust-to-power can be calculated from Eqs. 2.26 and 2.29, according to Eq. 2.32.

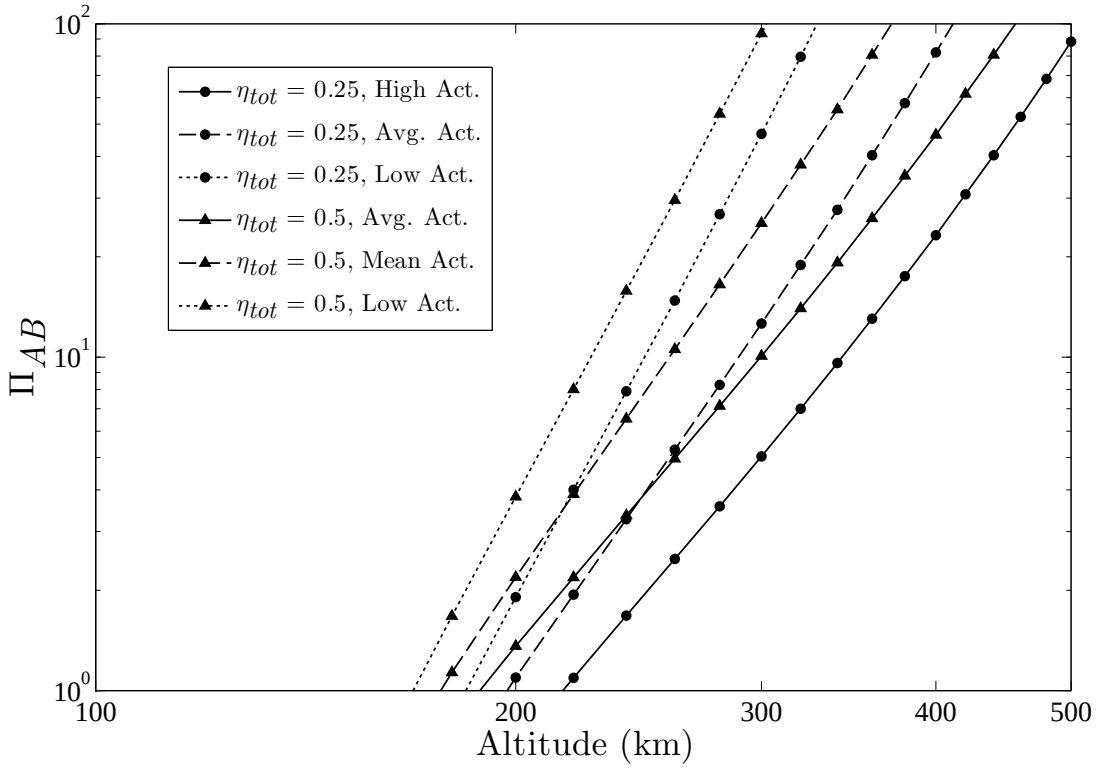

Figure 2.15: Feasibility parameter for the example air-breathing spacecraft, assuming k_G = 1.77, and a solar array power of = 145 W/m^2. Note that this air-breathing spacecraft is "more feasible" at higher altitudes.

$$\frac{F_T}{P_{req}} = \frac{nmv_o^2\left(2A_{drag} + A_{inlet}\right)}{\frac{1}{2\eta_{tot}\eta_{inlet}} nmv_o^3 A_{inlet}\left(2\left(\frac{A_{drag}}{A_{inlet}}\right)+1\right)^2} = \frac{2\eta_{tot}\eta_{inlet}}{v_o}\left(2\left(\frac{A_{drag}}{A_{inlet}}\right)+1\right)^{-1} \tag{2.32}$$

Note that the thrust-to-power is not a function of atmospheric density or composition. Also recall that the orbital velocity is nearly constant at the altitudes of interest. So, the thrust-to-power required for the air-breathing propulsion system is only a function of the spacecraft geometry and the thruster and inlet efficiencies. The example air-breathing spacecraft has a 90% inlet efficiency and a drag-to-inlet area ratio of 0.5. If the total efficiency of the propulsion system is 25–50%, then the required thrust-to-power is approximately 29–59 millinewtons per kilowatt.

2.4.3 Practicality

Many ideas may be deemed "feasible," but it is equally important to understand when a concept becomes practical. In the case of Berner and Camac [17], the goal was to accumulate large amounts of ambient gas in the shortest time possible, but that is not the case here. Consider that launch vehicle mass-to-orbit capability decreases with increasing orbit altitude. In practical terms, this means that for a given launch vehicle (i.e. cost) a more massive spacecraft can be launched into a lower-altitude orbit. For a given spacecraft size and mass, however, atmospheric drag decreases with increasing altitude. Thus, the lifetime of the satellite increases with increasing altitude. Here we consider the satellite lifetime beyond which an air-breathing system becomes practical. The satellite lifetime is determined for a spacecraft *without* an air-breathing propulsion system in order to demonstrate where an air-breathing system might achieve a practical benefit.

For the practicality study, it is assumed that the propulsion system of a competing non-air-breathing spacecraft has the same geometry as the air-breathing spacecraft described above, and that the drag force exerted on both spacecraft is equal. The non-air-breathing spacecraft is allowed a 10% initial propellant mass fraction, and its propulsion system has a total efficiency of 50% at a specific impulse of 3000 seconds. The non-air-breathing spacecraft's mission ends when the spacecraft runs out of propellant.

Figure 2.16 shows the lifetime for the example non-air-breathing spacecraft, assuming that it is still launched on a Pegasus launch vehicle. For the lifetime calculations, it is assumed that the non-air-breathing spacecraft continuously uses its stored propellant to compensate for drag. An air-breathing spacecraft would yield a practical benefit for a mission that requires a lifetime longer than the capability of the non-air-breathing spacecraft. For example, with all else being equal, an air-breathing propulsion system would be practical for keeping a spacecraft the size of the example spacecraft in a 200-kilometer circular, sun-synchronous orbit for longer than 3 years.

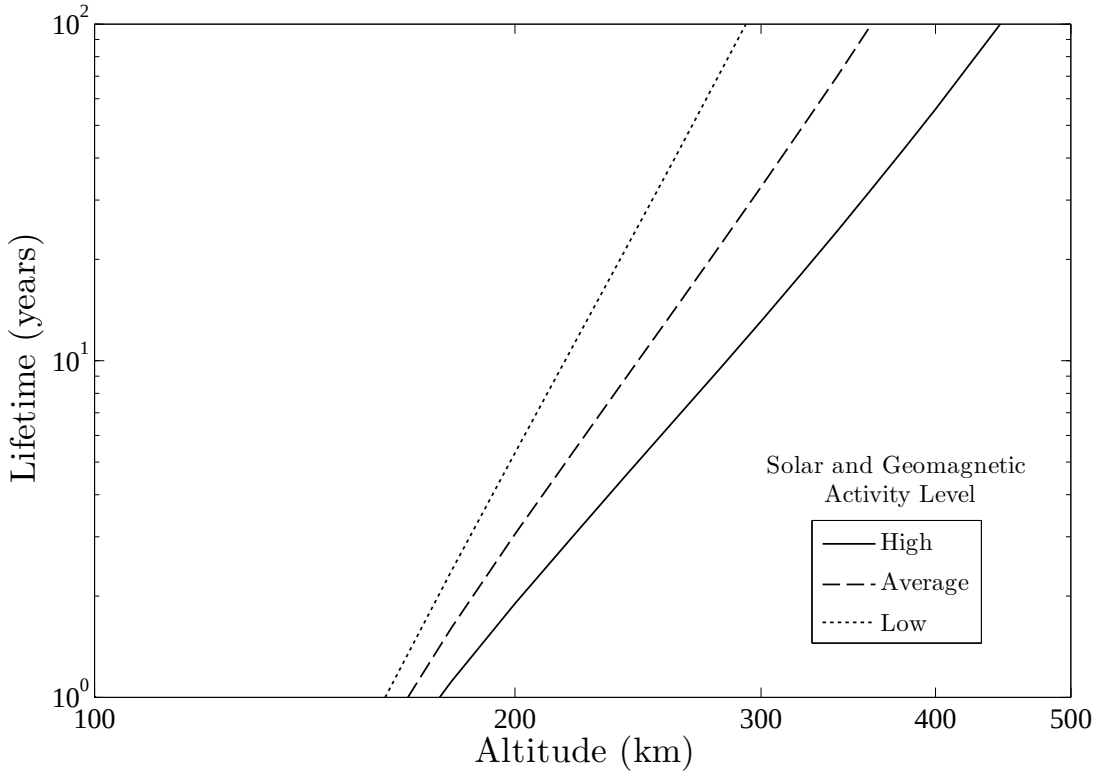

Figure 2.16: Lifetime of a non-air-breathing example spacecraft, assuming k_{fuel} = 0.1, I_{sp} = 3000 s, and η_{tot} = 0.5. An air-breathing system yields a practical benefit for lower altitudes and greater lifetimes than the τ_L-lines (i.e. above and to the left of the lines in the plot).

Based on the above feasibility analysis and practicality considerations, Table 2.2 summarizes the properties of a small demonstration mission for an air-breathing satellite.

Table 2.2: Example air-breathing spacecraft summary. The spacecraft is assumed to be operating in a sun-synchronous orbit during average solar and geomagnetic conditions.

Property	Value
Length	$L_{s/c} = 2.1$ m
Outer diameter	$OD_{s/c} = 0.7$ m
Total Mass	$M_0 = 325$ kg
Area Ratio	$A_{drag}/A_{inlet} = 0.5$
Inlet Efficiency	$\eta_{inlet} = 0.90$
Thruster Efficiency	$\eta_{tot} = 0.25$
Orbit Altitude	$h = 200$ km
Mass flow rate	$\dot{m}_{pr} = 0.51$ mg/s
Thrust	$F_T = 8.8$ mN
Minimum specific impulse	$I_{sp} = 1730$ s
Equivalent minimum voltage	$V_{eq} = 33$ V
Thruster power required	$P_{req} = 306$ W
Minimum lifetime	$\tau_L = 3$ years

2.5 Propulsion Requirements

The absolute lower limit on propulsion system performance is determined by Eq. 2.27, where a spacecraft with nearly zero drag area requires an effective exhaust velocity approximately equal to the orbital velocity. This theoretical lower limit corresponds to a specific impulse of about 800 seconds. The Earth's radius is much larger than the orbit altitudes in very low LEO. This means that the orbital velocity does not change significantly with altitude. Thus, the specific impulse required is essentially independent of orbit altitude, as shown by Fig. 2.13. Figure 2.1 showed that the normal mass flux at 150 – 300-kilometer altitudes is on the order of 10 – 0.1 milligrams per second per square meter of inlet area, respectively. Figure 2.11 suggests that the thrust required of the propulsion system will be on the order of 1s – 100s of millinewtons per square meter of total spacecraft frontal area. These numbers translate to the propulsion system exhaust jet containing 10s – 100s of watts of power for each square meter of ram area.

In order for air-breathing propulsion to be practical for the example used above, it would need to operate nearly continuously for just over 3 years, or about 27,000 hours. Ongoing experiments have shown that gridded ion thrusters can run for more than 42,000 hours [63], but this is with xenon propellant. Rather, a moderate specific impulse, long-lived plasma thruster that is capable of operating with oxygen and nitrogen propellant is the desired propulsion system for the air-breathing spacecraft.

2.5.1 Why RF?

Most developed EP systems use electrically-biased metal electrodes that are directly exposed to the plasma to apply a DC electric field that accelerates the propellant. These electrode materials may not be compatible with atmospheric gases during operation, possibly raising issues that are not present when operating with inert propellants. Recent experiments have shown that oxygen propellant will chemically react with EP thruster com-

ponents, in some cases causing metal parts to form oxide coatings [56]. Thrusters that use DC electric fields also require the use of thermionic cathodes to produce electrons. The cathode materials must be heated to very high temperatures to emit electrons, and they are "poisoned" when heated in an environment with a high partial pressure of oxygen [64], rendering them useless.

The use of RF power in space propulsion systems has been of particular interest to the EP research community due to its potential for improving thruster lifetime and the possibility for it to eliminate the need for thermionic cathodes [65]. As will be discussed in the next chapter, RF plasma systems are capable of ionizing a gas without directly exposing electrodes to the plasma. Satellite missions have successfully employed RF and microwave ion thrusters that use RF power to ionize the propellant gas [66, 67]. For example, the GOCE mission's propulsion system consists of gridded ion thrusters that use RF to ionize the propellant in the discharge chamber (though the exhaust plume-neutralizing cathodes are still DC thermionic hollow cathodes). The success of the propulsion system on the GOCE mission shows that RF is capable of operating in EP systems at low orbit altitudes, where the spacecraft is surrounded by a relatively high amount of oxygen.

Some other space propulsion systems have been suggested that employ only RF power and a magnetic field to ionize and accelerate the propellant. These systems are similar to the devices described by Jahn as *magnetic expansion thrusters* and *cyclotron-resonance thrusters*, and do not necessarily fit well under a single EP classification [68]. These RF thruster concepts are currently at varying levels of development [69–75].

Most EP systems have specific life-limiting mechanisms due to the erosion of thruster materials. This erosion is caused by the impact of high-energy exhaust with the thruster [76]. The use of atmospheric propellant may cause the erosion rates to be higher due to chemical interactions between the propellant and the thruster materials. Thus, the lifetime limitation of current flight-model EP systems is likely exacerbated when using atmospheric gases as propellant.

The energy of the propellant in the exhaust of some RF EP concepts previously mentioned is relatively low. In addition, these thrusters may be designed to have only inert materials in contact with the plasma. Only a few recent experiments have begun to measure the performance of some of these concepts [70, 71], but the data suggest that they may be capable of providing a useful amount of thrust. Because the exhaust energies are lower than in electrostatic thrusters, it is likely that the erosion of thruster materials can be reduced.

In addition to the potential for addressing the issue of limited thruster lifetime, RF technology may significantly reduce compatibility concerns by eliminating the need for thermionic materials. Alternative cathodes employing RF or microwaves have been operated in multiple laboratories, and microwave cathodes have successfully flown as neutralizers for the μ10 microwave ion thrusters on the Hayabusa mission, which returned a sample of asteroid material to Earth [67].

Currently, the two most mature electrostatic EP systems are gridded ion and Hall thrusters. Both suffer from a very low efficiency when operating at moderate specific impulse. In particular, Hall thrusters operating at low voltage suffer from poor propellant utilization efficiency (conversion of propellant atoms to thrust-producing ions), and the overall efficiency is lower when using alternative propellants [51,77]. Using an RF-augmented system may increase overall Hall thruster performance by increasing the propellant utilization efficiency. Recent studies have shown that the Hall thruster magnetic field configuration may be changed to drastically increase thruster lifetime [54]. Thus, it seems likely that an RF-augmented, magnetically-shielded Hall thruster would be the appropriate thruster for an air-breathing spacecraft.

2.6 Conclusion

This chapter demonstrated that an air-breathing satellite is feasible, and showed where such a system would be practical to implement over a non-air-breathing system. The performance characteristics of EP is in the range appropriate for an air-breathing orbital vehicle. In particular, the ability to operate with any gas species as a propellant, and EP's higher specific impulse than chemical rocket systems make it an attractive option for an air-breathing orbital mission. The capability of RF systems to eliminate the need for a thermionic cathode merits further investigation into their aptitude for improving EP performance. In particular, the cathode-less RF plasma with magnetic expansion thruster and the RF-augmented Hall thruster are attractive options for the propulsion system of an air-breathing satellite.

CHAPTER 3

RF Plasma Systems

The previous chapters presented the background and motivation for implementing RF technology in an EP system in order to provide in-space propulsion for an air-breathing satellite. This chapter discusses exactly what is meant by "RF plasma technology." The first section introduces basic RF concepts important for implementing any RF system, and the second section gives a brief treatment of physical processes in plasmas.

3.1 RF Engineering Principles

All Alternating Current (AC) signals radiate some energy into free space. This energy is radiated in the form of electromagnetic waves. The amount of energy radiated is very low at power-line AC frequencies (50-60 hertz). However, it has been found the energy radiated from a conductor at 10 kilohertz can be transmitted and received across large distances on Earth if a sufficiently large antenna is used. When frequencies above approximately 100 gigahertz are used with normal antennas, more of the energy is radiated as heat than radio waves. So, although there are no absolute theoretical constraints on the range of frequencies, *radio frequency* (RF) power refers to AC power in the frequency range that is practically useful on Earth, about 3 kilohertz to 300 gigahertz. Circuits that operate in the RF frequency range must be designed with careful consideration of the unique properties of RF power (e.g. RF is radiated from conductors, and so energy is not strictly confined to a circuit board) [78].

A large number of industries (primarily communication-related) have formed around the ability to control, transmit, and receive RF energy. For example, the plasma processing/semiconductor manufacturing industry uses RF technology to enable a wireless transfer of energy from an AC electrical outlet to the electrons in low-pressure gas reactors. It is important to note here that the plasma processing industry uses oxygen and nitrogen as working gases for manufacturing processes, such as nitriding metals and sputtering wafer material, showing that it is compatible with LEO atmospheric components.

In the United States, the Federal Communications Commission (FCC) regulates the use of electromagnetic radiation across the RF spectrum. The Code of Federal Regulations defines Radio Waves as "electromagnetic waves of frequencies arbitrarily lower than 3,000 GHz, propagated in space without artificial guide" [79]. The FCC is responsible for assigning and licensing the use of frequencies between 9 kilohertz and 275 gigahertz [80]. The FCC allocates certain frequencies for Industrial, Scientific, and Medical (ISM) uses, referred to as the ISM radio bands. Frequencies in the ISM bands can be used in the laboratory without creating the danger of interfering with communications networks. The frequency in the ISM bands that is most commonly used by the plasma processing industry is 13.56 megahertz, and so there are many low-cost, medium-power RF generators readily available at that frequency.

The frequency of RF typically referred to is the *circular frequency*, f, given in units of cycles per second or hertz. Electrical calculations that are dependent on the frequency, however, generally use the *angular frequency*, ω, which has units of radians per second. Circular frequency and angular frequency are related by Eq. 3.1.

$$\omega = 2\pi f \tag{3.1}$$

Electromagnetic radiation of a given frequency may generally be thought of as a traveling plane wave that moves through a material at the speed given by Eq. 3.2, where μ is

the magnetic permeability and ε is the electric permittivity of the material. In vacuum, the permittivity and permeability are that of free space, and the wave propagates at the speed of light, c, approximately 3.0×10^{-8} meters per second.

$$c = \sqrt{\frac{1}{\mu\varepsilon}} \tag{3.2}$$

Based on the speed and the frequency, the wavelength of the electromagnetic wave, λ, is determined by Eq. 3.3. The wavelength is an important characteristic length to consider when employing RF power because it is the length scale over which large voltage differences can be driven, even in a conductor. For 13.56 megahertz in free space, $\lambda \approx 22$ meters.

$$\lambda = \frac{c}{f} \tag{3.3}$$

When working with RF power, the *electrical length* is an important parameter. The electrical length is the ratio of the physical length of a conductor to the wavelength of the electromagnetic energy. The electrical length is a property that gives a general sense of the behavior of RF waves in the components and transmission lines of an electrical circuit. A conductor whose physical length is a significant fraction of an RF wavelength or larger is considered to be "electrically large" or "long," and a conductor whose physical length is a small fraction of the RF wavelength are considered to be "electrically small" or "short." In this dissertation, "a small fraction of a wavelength" refers to one-tenth of the RF wavelength (e.g. about 2 meters for 13.56 megahertz in free space). Note that the electrical length is a function of the RF frequency and the properties of the material that the RF energy is traveling through. Note also that the electrical length does not follow a well-defined rule. Rather, the electrical length is a concept that provides a guideline to understand how RF energy will behave in a particular system [81].

3.1.1 Impedance and Admittance

The electromagnetic wave may also be thought of as a traveling, AC voltage signal. An important quantity when considering an AC signal propagating through a space larger than one-tenth of the wavelength is the *characteristic impedance*. The characteristic impedance in a material, typically labeled Z_0, is determined by Eq. 3.4. Note that permeability is in units of inductance per unit length, and permittivity is capacitance per unit length, and the square root of their ratio is in units of resistance, ohms. In free space, $Z_0 \approx 377\ \Omega$.

$$Z_0 = \sqrt{\frac{\mu}{\varepsilon}} = \sqrt{\frac{\mu_0 \mu_r}{\varepsilon_0 \varepsilon_r}} \tag{3.4}$$

Z_0 comes from the necessity to satisfy generalized Ohm's law, given by Eq. 3.5. Characteristic impedance is not resistance, but simply the ratio of voltage to current of a time-varying signal propagating in a medium. Note that the characteristic impedance may be dependent on the frequency of the electromagnetic energy.

$$V(t) = Z(\omega) I(t) \tag{3.5}$$

Impedance is a complex quantity that has a real component called *resistance*, R, and an imaginary component called *reactance*, X, as shown in Eq. 3.6, where $j \equiv \sqrt{-1}$.

$$Z \equiv R + jX \tag{3.6}$$

The frequency dependence of impedance may be illustrated by applying an AC voltage across an ideal, lossless inductor. Inductors are described by a property called the *inductance*, L, and a lossless inductor identically has zero resistance. The impedance of the lossless inductor therefore consists only of the inductive reactance, which is a linear function of frequency, as shown in Eq. 3.7.

$$Z_{ind} = j\omega L \tag{3.7}$$

Similarly for an ideal lossless capacitor with *capacitance*, C, the impedance is a purely imaginary quantity called the capacitive reactance, also a function of frequency, as shown in Eq. 3.8.

$$Z_{cap} = \frac{1}{j\omega C} = \frac{-j}{\omega C} \tag{3.8}$$

Pure resistances or inductances add when connected in series, but the reciprocal of capacitances adds in series. This is clear when looking at Eqs. 3.6– 3.8, and understanding that it is the *impedance* that adds in series, as shown by Eq. 3.9.

$$Z_{equiv} = \sum_{series} Z_s \tag{3.9}$$

To analyze parallel circuit components with the same arithmetic ease as series components, the *admittance*, Y, may be used. The admittance is the reciprocal of the impedance, as shown by Eq. 3.10.

$$\frac{1}{Z} \equiv Y \equiv G + jB \tag{3.10}$$

For a purely resistive circuit component, the admittance is equal to the reciprocal of resistance, $Y = G = 1/R$, where G is called the *conductance*. For a purely reactive circuit component, the admittance is equal to the reciprocal of reactance, $Y = B = 1/X$, where B is called the *susceptance*. The admittance of circuit components in parallel add, as shown by Eq. 3.11.

$$Y_{equiv} = \sum_{parallel} Y_p \tag{3.11}$$

Admittance is a useful property to consider if circuits with parallel components are to be quickly understood or designed. Note that admittance, conductance, and susceptance are all in units of $1/$ohms, also known as "mhos" or siemans.

3.1.2 Transmission Lines

As previously described, RF energy has an associated wavelength, and the guideline for determining whether a circuit is "electrically large" is if its length scale is larger than one-tenth of a wavelength. Coaxial cable is commonly used to transmit RF power between points in a circuit. In a coaxial cable, the RF wave propagates through the dielectric material between the inner conductor and the outer conductor. Two common materials used as dielectric material are polytetrafluoroethylene (PTFE), also known as "Teflon," and polyethylene. These materials have relative permittivities, ε_r, that are greater than unity, and so the wavelength of the RF wave is shorter in these materials than in vacuum.

Relative permittivity is defined as $\varepsilon_r \equiv \varepsilon/\varepsilon_0$, where ε is used with Eqs. 3.2 and 3.3 to determine the wavelength. For PTFE, $\varepsilon_{r,PTFE} = 2.1$, so the wavelength of 13.56 megahertz RF energy in PTFE, λ_{PTFE}, is approximately 15.3 meters. For polyethylene, $\varepsilon_{r,PE} = 2.25$, and λ_{PE} is approximately 14.7 meters. Thus, the lengths associated with the one-tenth of a wavelength guideline are shorter in coaxial cables than in vacuum. PTFE is vacuum compatible and has a higher melting temperature than polyethylene, but it is also more lossy and more expensive. So, an engineering trade must be considered when choosing which coaxial cable to implement.

The electrical length of a transmission line is useful when considering how to model the transmission line in an electrical circuit. An electrically short cable can be modeled as a set of discrete circuit components called a *lumped element model*, shown in Fig. 3.1. The behavior of the RF energy through an electrically short cable can thus be simply represented in a circuit schematic. For a lossless coaxial cable, the series resistance and parallel conductance are identically zero.

When many short cables are connected in series, an electrically long cable may be created. A model of a long cable can then be implemented by placing many of the lumped-element cable sections in series. Such a circuit is considerably more difficult to analyze than the one in Fig. 3.1. Instead, an electrically long cable may be described by properties

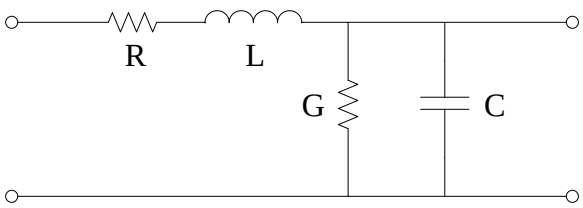

Figure 3.1: Model of an electrically short (i.e. shorter than one-tenth of the RF wavelength) section of transmission line.

per unit length, as depicted in Fig. 3.2. In the limit where the discrete sections of the coaxial cable are infinitely short (i.e. Δx approaches zero), the analysis may be simplified by using a *distributed-element* model.

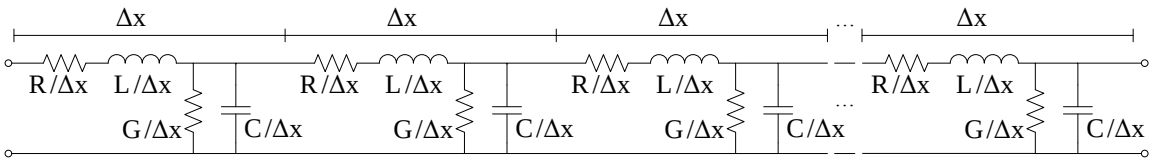

Figure 3.2: Simple model of an electrically long (i.e. longer than one-tenth of the RF wavelength) transmission line.

In a distributed-element model, the resistance, inductance, conductance, and capacitance of a cable are defined per unit length. For a fixed RF driving frequency, ω, the sinusoidal, steady-state voltage and current along a one-dimensional, uniform transmission line then follow Eqs. 3.12 and 3.13, respectively.

$$\frac{dV}{dx} = -(R + j\omega L)I(x) \tag{3.12}$$

$$\frac{dI}{dx} = -(G + j\omega C)V(x) \tag{3.13}$$

These two equations are known as the "transmission line equations" or "Telegrapher's Equations" in phasor form, and they describe a traveling wave in the transmission line [82]. From these equations, the *characteristic impedance*, Z_0, for the transmission line can be calculated from the electrical properties, as shown by Eq. 3.14.

$$Z_0 = \sqrt{\frac{R + j\omega L}{G + j\omega C}} \tag{3.14}$$

The cables used for RF transmission are designed to be low-loss. At frequencies greater than 10 kilohertz, typically $\omega L \gg R$ and $\omega C \gg G$. Thus, the approximation $Z_0 \approx \sqrt{L/C}$ is generally used for transmission lines in RF systems. Although transmission lines can be made in many shapes, one of the most commonly available profiles is the *coaxial cable*. A coaxial cable consists of a center conductor that is surrounded by an insulating dielectric material, and concentrically surrounded by an outer conductor, as shown in Fig. 3.3.

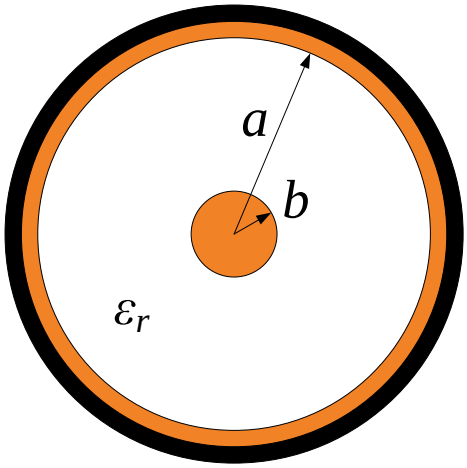

Figure 3.3: Cross-section of a typical coaxial cable.

The electrical properties of coaxial cables are defined according to the geometry of the cross-section and the material properties of the dielectric. The characteristic impedance for a coaxial cable is given by Eq. 3.15, where the variables refer to Fig. 3.3.

$$Z_{0,\,coax} = \frac{1}{2\pi}\sqrt{\frac{\mu}{\varepsilon}}\ln\left(\frac{a}{b}\right) \approx \frac{60}{\sqrt{\varepsilon_r}}\ln\left(\frac{a}{b}\right) \tag{3.15}$$

Typically, the relative permeability of the dielectric material is unity, $\mu_r = 1$, and so Z_0 is only dependent on ε_r. The RF industry has adopted fifty ohms, 50-Ω, as the standard characteristic impedance for a majority of coaxial cables due to a compromise between

reducing cable attenuation (theoretical minimum at 77-Ω for air dielectric) and peak power handling (theoretical maximum at 30-Ω for air dielectric) [81].

Real transmission lines are not infinitely long, and are terminated at both ends either by a *power supply* or a *load*. RF power supplies are designed to have an output impedance that is equal to the transmission line characteristic impedance. However, the load impedance may be quite different than the characteristic impedance of the power supply and transmission line. When this is the case, the transmission line acts as a transformer for the load impedance. For a finite-length transmission line, the load impedance is transformed according to Eq. 3.16, where k is the wave number, and l is the distance from the transmission line input to the load [81].

$$Z_{in} = Z_0 \frac{Z_L + jZ_0 \tan kl}{Z_0 + jZ_L \tan kl}; \qquad k = \frac{2\pi}{\lambda} \tag{3.16}$$

Note for a single input RF frequency, the input impedance is equal to the load impedance if the transmission line length is an integer multiple of a half-wavelength. Some experiments, such as that described by Kieckhafer and Walker [83], use a half-wavelength-long transmission line between the matching network and the load in order to avoid an impedance discontinuity at one end of the transmission line.

3.1.3 Impedance Matching

If the load impedance is not equal to the transmission line characteristic impedance, then an impedance discontinuity exists at the connection between the transmission line and the load. Ohm's law must be satisfied everywhere in the system, and Kirchoff's current law applies at the load end of the transmission line. Since the RF power is a traveling wave, the impedance discontinuity at the load end will cause a fraction of the incident RF power to be reflected back toward the power supply. Equations 3.17 – 3.19 give Ohm's law in the system, the boundary condition at the load, and Kirchoff's current law at the load,

respectively, where V_f is the amplitude of the RF voltage traveling from the supply to the load (i.e. in the "forward" direction), I_f is the amplitude of the current associated with the forward voltage, Z_0 is the characteristic impedance of the transmission line, V_r and I_r are the reflected voltage and current amplitudes in the transmission line, respectively, V_L is the voltage across the load, I_L is the current through the load, and Z_L is the impedance of the load. These equations refer to the circuit depicted in Fig. 3.4.

$$V_f = I_f Z_0,\ V_r = I_r Z_0,\ V_L = I_L Z_L \tag{3.17}$$

$$V_L = V_f + V_r \tag{3.18}$$

$$I_L = I_f - I_r \tag{3.19}$$

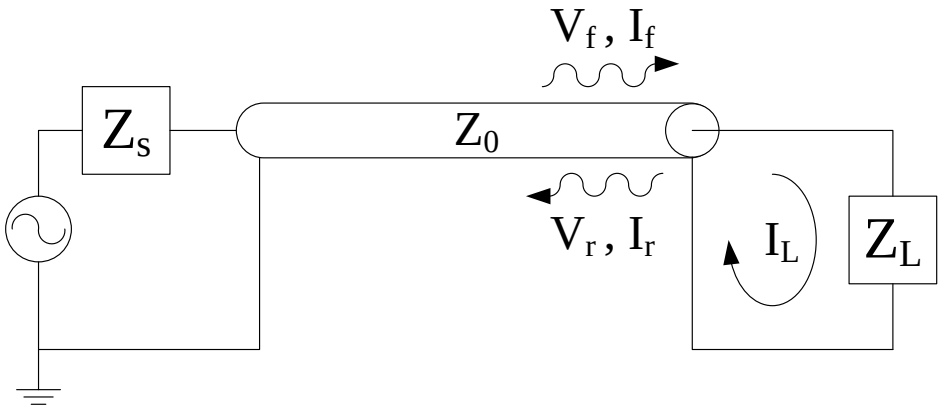

Figure 3.4: Schematic of RF power behavior at the load end of a transmission line.

Combining Equations 3.17 – 3.19 yields Eq. 3.20. Rearranging Eq. 3.20 yields the reflection coefficient, Γ. The reflection coefficient is related to the difference between the characteristic impedance of the system and the load impedance according to Eq. 3.21.

$$V_f + V_r = \frac{Z_L}{Z_0} V_f - \frac{Z_L}{Z_0} V_r \tag{3.20}$$

$$\Gamma = \frac{V_r}{V_f} = \frac{|V_-|}{|V_+|} = \frac{Z_L - Z_0}{Z_L + Z_0} \tag{3.21}$$

Reflected power causes an RF system to be less efficient because power that is reflected cannot be delivered to the load. The reflected power instead must be dissipated by the power supply or cable. Real transmission lines are not perfectly lossless. Thus, reflected power causes increased dissipation in the transmission line, which can lead to cable heating. Reflected power also creates locations of increased voltage in the transmission line. When there is a significant amount of reflected power, the voltage in the cable may be high enough to cause electrical breakdown, even while operating below the cable power rating.

In a real system, the RF power supply is typically placed at some finite distance from the load. Thus, a transmission line must be used to transmit the RF power from the supply to the load. In order to eliminate an impedance discontinuity at the load, a circuit of discrete components must be implemented at the connection between the transmission line and the load. This circuit is generally referred to as a *matching network* because its purpose is to match the load impedance to the transmission line characteristic impedance. Some common examples of simple matching network configurations are shown in Fig. 3.5.

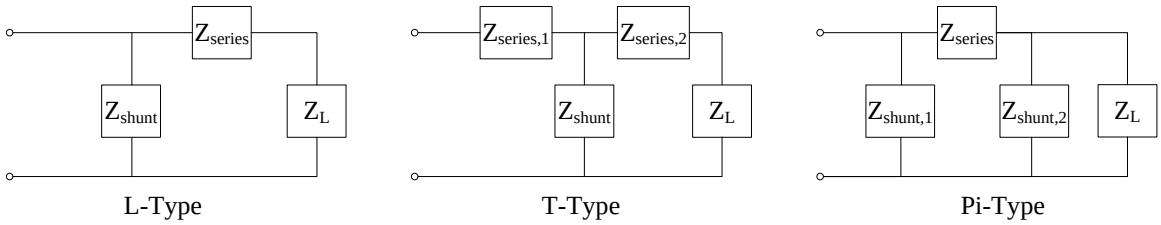

Figure 3.5: Common matching network types. The types are named according to the layout of the circuit components.

The goal of a matching network is to maximize power transfer from the transmission line to the load. So, matching networks typically use low-loss reactive components (i.e. *high Q*, where $Q = X/R$) to transform the load impedance to the standard 50 Ω. Using a smaller number of matching components simplifies the design and analysis of the matching network, and also reduces the probability of exciting internal self-resonance modes. The associated equivalent impedances of the matching networks and loads depicted

in Fig. 3.5 are given by Eqs. 3.22 – 3.24, respectively.

$$Z_{eq,L} = \left(\frac{1}{Z_{shunt}} + \frac{1}{Z_{series} + Z_L} \right)^{-1} \tag{3.22}$$

$$Z_{eq,T} = Z_{series,1} + \left(\frac{1}{Z_{shunt}} + \frac{1}{Z_{series,2} + Z_L} \right)^{-1} \tag{3.23}$$

$$Z_{eq,\Pi} = \left(\frac{1}{Z_{shunt,1}} + \left(Z_{series} + \left(\frac{1}{Z_{shunt,2}} + \frac{1}{Z_L} \right)^{-1} \right)^{-1} \right)^{-1} \tag{3.24}$$

3.1.4 Smith Chart

The Smith chart is a commonly used tool for designing RF circuits [82]. Although images of the Smith chart sometimes look overwhelmingly complicated to the untrained eye, it is actually a quite simple and very powerful set of coordinates that can be used to quickly understand and design RF circuits. The Smith chart is typically used to plot impedance. Impedance is a complex quantity, and so the Smith chart displays the real and imaginary components of impedance. The horizontal axis is the real axis, and circles of constant real resistance are tangent to the right side of the chart. As labeled in Fig. 3.6, the right side of the real axis represents an open circuit, and the left side of the real axis represents a short circuit. The Smith chart is normalized to the system characteristic impedance, such that the center of the chart is equal to the characteristic impedance (typically 50-Ω), and therefore represents a matched condition. Note that inductance has a positive imaginary impedance, while capacitance has a negative imaginary impedance.

The Smith chart may also be plotted in admittance coordinates, as displayed in gray in Fig. 3.6. Note that the admittance coordinates are the same as the impedance coordinates, but rotated by 180 degrees. Thus, positive susceptance is below the real axis, in the opposite arrangement as reactance. Having both the impedance and admittance coordinates displayed on the same plot allows for quick graphical calculations of the components required to match any given load impedance.

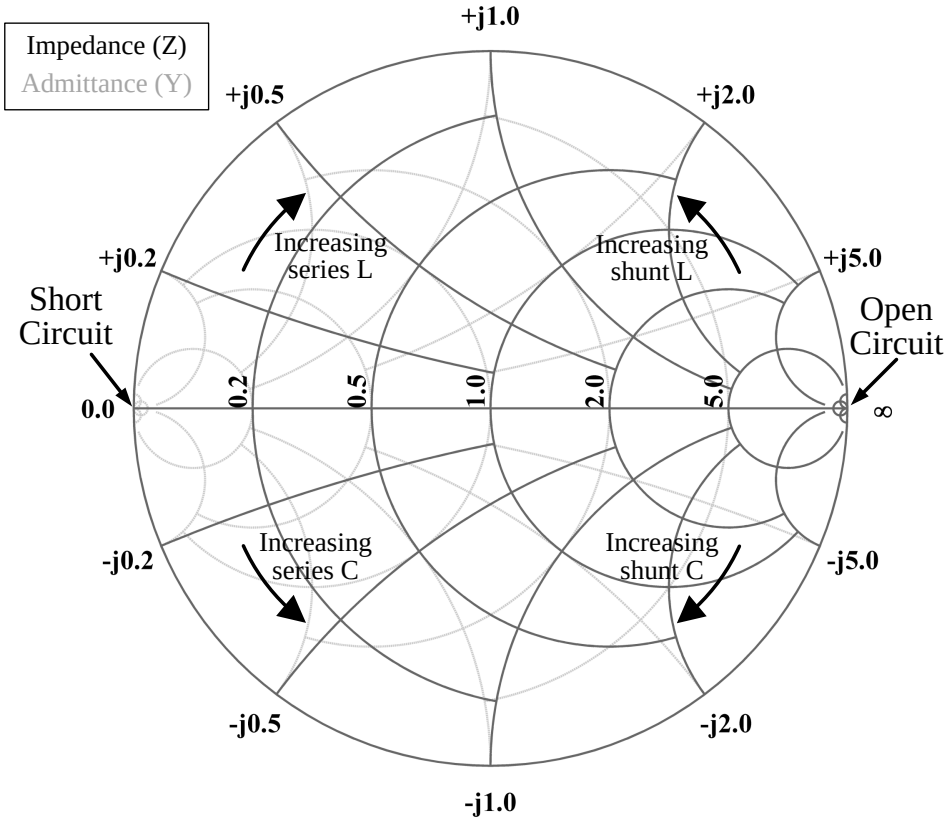

Figure 3.6: Smith chart showing both impedance and admittance coordinates.

As an example, arbitrarily taking a load impedance $Z_L = (5 + 45j)\Omega$ in a system with a 50-Ω characteristic impedance (i.e. $Z_0 = 50\,\Omega$), Fig. 3.7 shows how the Smith chart may be used to design a matching network. In the example, an L-type configuration is used with two ideal capacitors to transform the load impedance to the characterisic impedance. Referring to Fig. 3.7 and starting at the load, capacitor "A" is connected in series, and adds $-1/\omega C_A$ to the reactance of the load impedance. Switching to the admittance coordinates, capacitor "B" is connected in parallel, and adds ωC_B to the susceptance. In this example, the coordinates on the Smith chart show that $-j/\omega C_A = (0.3j - 0.9j) \times 50\,\Omega = 30j\,\Omega$, and $j\omega C_B = (0.0j - 3.0j) \times (1/50)\,\Omega^{-1} = 0.06j\,\Omega^{-1}$. Thus, in a 13.56 MHz system, the matching capacitors must have the values $C_A = 391$ pF and $C_B = 704$ pF in order to match the load impedance, Z_L, to 50 Ω.

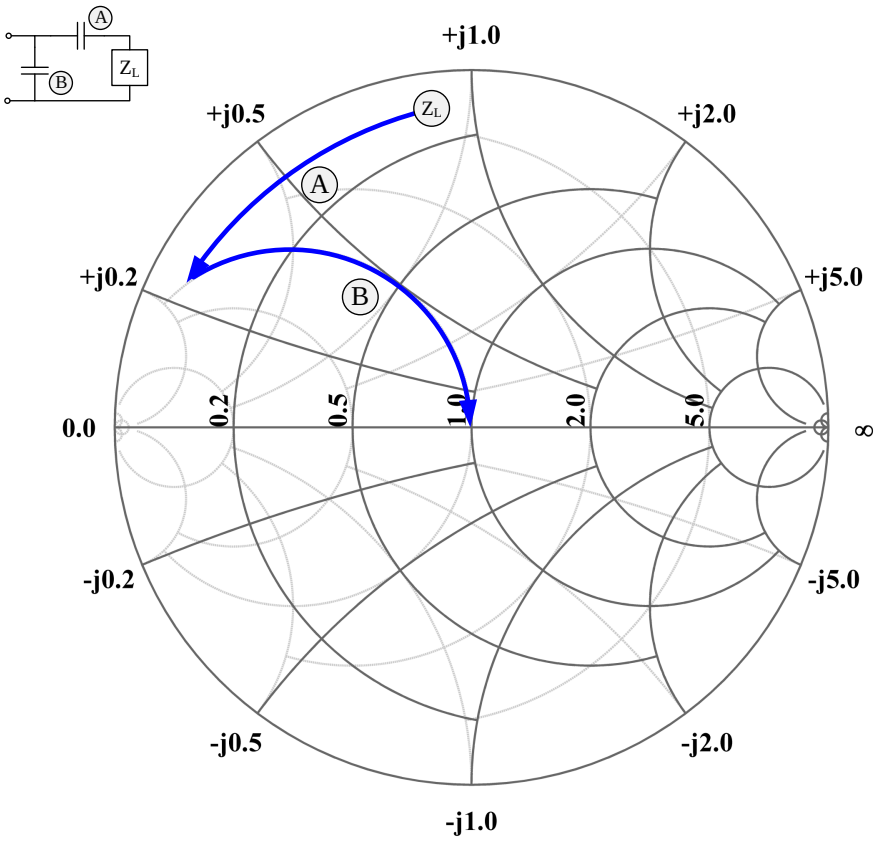

Figure 3.7: Smith chart showing matching network design procedure.

3.2 Plasma

Simply stated, plasma is an ionized gas that collectively reacts to externally applied electric and magnetic fields. Typically thought of as being "the fourth state of matter," the characteristic property of a plasma is that a significant portion of the gas is electrically charged. It is this electric charge that allows the particles to interact with electric and magnetic fields thought the Lorentz force, given by Eq. 3.25, where m is the particle mass, $\vec{v}$ is the particle velocity, t is time, q is the particle charge, $\vec{E}$ is the electric field, and $\vec{B}$ is the magnetic field.

$$m\frac{d\vec{v}}{dt} = q(\vec{E} + \vec{v} \times \vec{B}) \tag{3.25}$$

The forces acting on charged particles are a function of mass, charge, and velocity. There can be a large disparity in the the mass and temperature of the ions and electrons.

So, the time-dependent behavior of a plasma may be very complicated. The different time scales associated with different physics are typically expressed as frequencies. A higher characteristic frequency corresponds to a faster time scale.

By definition, a plasma also has approximately an equal number of positive and negative charges, such that the sum of charge over the entire plasma is nearly equal to zero. This property is referred to as *quasineutrality*, and this is expressed by $qn_i \approx en_e$. Although the plasma is quasineutral, the ions and electrons are able to move relative to each other, creating spontaneous regions of net charge density. The charge separation creates an electric field that can be determined from Poisson's equation, Eq. 3.26, where ρ_q is the charge density and ε_0 is the permittivity of free space.

$$\nabla \cdot \vec{E} = \frac{\rho_q}{\varepsilon_0} \tag{3.26}$$

This electric field exerts a force on the charged particles, $\vec{F}_{el}$, causing an acceleration determined by Eq. 3.27.

$$\vec{F}_{el} = q\vec{E} \tag{3.27}$$

Because the ions are much heavier than the electrons, one may assume that the ions are stationary. Thus, the electric field force acts only to change the velocity of the electrons, according to Eq. 3.28, where m_e is the electron mass, $\vec{v}_e$ is the electron velocity, and e is the elementary charge.

$$m_e \frac{d\vec{v}_e}{dt} = -e\vec{E} \tag{3.28}$$

To simplify the analysis, the behavior can be examined in one dimension, according to Eqs. 3.29 – 3.31, where x is the spatial dimension, and n_e is the electron number density.

$$\frac{dE}{dx} = \frac{\rho_q}{\varepsilon_0} \tag{3.29}$$

$$\frac{dE}{dt} = \frac{dE}{dx}\frac{dx}{dt} = v_e \frac{en_e}{\varepsilon_0} \tag{3.30}$$

$$\frac{d^2 v_e}{dt^2} = \frac{e}{m_e}\frac{dE}{dt} = v_e \left(\frac{e^2 n_e}{m_e \varepsilon_0}\right) \tag{3.31}$$

Equation 3.31 describes oscillatory behavior, which in the plasma represents the "sloshing" of electrons about the ions. The time scale of this behavior is described by a characteristic frequency called the *electron plasma frequency*, ω_p, given by Eq. 3.32.

$$\omega_p = \sqrt{\frac{q^2 n_e}{m_e \varepsilon_0}} \tag{3.32}$$

The oscillatory behavior of plasma naturally arises from thermal motion of the charged particles. This example illustrates the time-dependent nature of plasma physics. Note that this analysis could also be performed for ions to obtain an ion plasma frequency, ω_{pi}. In a quasineutral plasma, the electron plasma frequency is typically much greater than the ion plasma frequency because $\omega_{pe}/\omega_{pi} \approx \sqrt{m_i/m_e}$.

The collective nature of a plasma acts to shield out external electric fields from the bulk population. The characteristic length over which the plasma is able to collectively re-arrange charges is called the *Debye Length*, λ_D, and is given by Eq. 3.33, where k_B is the Boltzmann constant, and T_e is the electron temperature.

$$\lambda_D = \sqrt{\frac{k_B T_e}{n_e e^2}} \tag{3.33}$$

In an infinitely large plasma, spontaneous electric fields may develop over length scales of a few Debye lengths. In laboratory plasma systems, some part of the plasma interacts

with a material surface. The plasma forms a *sheath* around these surfaces. The sheath is not quasineutral, and the thickness of the sheath is generally on the order of a few Debye lengths. Note that the Debye length is a function of the electron temperature and density.

The characteristic speed for the plasma can be found by multiplying the ion plasma frequency by the Debye length. This speed is referred to as the *Bohm speed* or the *ion acoustic speed*, and is shown in Eq. 3.34, where m_i is the mass of an ion.

$$v_B = \sqrt{\frac{k_B T_e}{m_i}} \tag{3.34}$$

If the plasma is not bounded by a material surface, then the Bohm speed represents the speed at which ions and electrons collectively propagate through free space. The Bohm speed is also known as the *ambipolar speed*.

The plasmas used in space propulsion systems are generally operated at low pressure. Electrostatic propulsion systems in particular use *non-thermal*, *low-temperature* plasmas. These plasmas are *non-thermal* because they are not in thermodynamic equilibrium, and so the ion and electron energy distributions are characterized by much different temperatures. These plasmas are *low-temperature* because the isotropic part of the ion energy distribution is at a temperature not much greater than room temperature. This type of plasma is common in everyday life, as it is the same type of plasma that powers fluorescent light bulbs, neon signs, and flat-panel displays. Non-thermal, low-temperature plasmas are characterized by weak ionization (i.e. only a small fraction of the gas is ionized). Therefore, the behavior of the uncharged gas, typically referred to as the *neutrals*, also has a strong effect on the plasma properties.

The neutrals are not influenced by electric or magnetic fields. So, they only interact with the electrons, ions, and other neutrals in the plasma through collisions. The length scale that is relevant for neutral behavior is the *mean free path* mentioned previously, which is the average distance that a gas particle will travel before it experiences a collision with

another gas particle. Typically, the individual gas particles are modeled as hard-spheres or "billiard balls." The mean free path for a homogeneous, single-species, neutral ideal gas is given in Eq. 3.35, where n_g is the neutral gas density and σ_m is the cross-section for a momentum-exchange collision. If the length scale of an unbounded system of gas particles is much smaller than the mean free path, then the particles are not likely to participate in collisions before leaving the system.

$$\lambda_{mfp} = \frac{1}{n_g \sigma_m} \tag{3.35}$$

The expected time between collisions for the neutral gas particles determines the characteristic time scale for the neutral gas, which is expressed as the *collision frequency*, ν_m. The collision frequency is a function of the number density of the gas, n_g, the hard-sphere cross-sectional area of the colliding particles, σ_m, and the relative velocity of the interacting particles, v, according to Eq. 3.36. Note that the product of the cross-section and the velocity is expressed in angle brackets because the cross-section is a function of the interaction velocity.

$$\nu_m = \frac{v}{\lambda_{mfp}} = n_g \langle \sigma_m v \rangle \tag{3.36}$$

The neutral gas is typically assumed to have an isotropic, Maxwellian velocity distribution. Thus, the temperature of the gas defines the mean speed of the neutrals, according to Eq. 3.37, where T_g is the temperature of the gas, and m_g is the mass of each gas particle. This velocity is referred to as the *thermal velocity*, v_{th}.

$$v_{th} = \sqrt{\frac{8 k_B T_g}{\pi m_g}} \tag{3.37}$$

The full equation of motion for the charged particles in the absence of a magnetic field is given by Eq. 3.38.

$$mn \frac{dv}{dt} = nqE - \nabla \cdot n - mn\nu v \tag{3.38}$$

Assuming that the particles are isothermal and at steady-state, Eq. 3.38 can be re-arranged as Eq. 3.39.

$$v = \frac{q}{k_B T} E - \frac{k_B T}{m\nu} \frac{\nabla n}{n} \tag{3.39}$$

The transport of particles due to density gradients can then be described by the diffusion coefficient, D, given by Eq. 3.40.

$$D = \frac{k_B T}{m\nu_m} \tag{3.40}$$

Charged particle transport due to electric fields can be described by the mobility, μ, given by Eq. 3.41.

$$\mu = \frac{q}{m\nu_m} \tag{3.41}$$

Typically, it is assumed that collisions within the plasma cause the electrons to have an energy distribution, $f(\varepsilon)$, that is Maxwellian and described by a temperature, T_e, according to Eq. 3.42, where k_B is the Boltzmann constant.

$$f(\varepsilon) = \frac{2}{\sqrt{\pi}} (k_B T_e)^{-3/2} \varepsilon^{1/2} \exp\left(\frac{-\varepsilon}{k_B T_e}\right) \tag{3.42}$$

In most low-pressure, low-temperature plasma systems, collisions between electrons and neutrals are responsible for most of the ionization events, termed *electron-impact ionization*. The fraction of the electron population at higher energy increases with increasing temperature. It is these higher-energy electrons that can participate in ionization events, as shown in Fig. 3.8.

The cross-sections for collisional processes are also a function of the interaction energy. The rate constant of an electron-impact process l, k_l, accounts for these competing effects. Rate constants are calculated using Eq. 3.43. Figure 3.9 shows how the rate constants in argon are a function of the electron temperature.

$$k_l = \int_0^\infty f(\varepsilon) \left(\frac{2\varepsilon}{m_e}\right)^{1/2} \sigma_l(\varepsilon)\, d\varepsilon \tag{3.43}$$

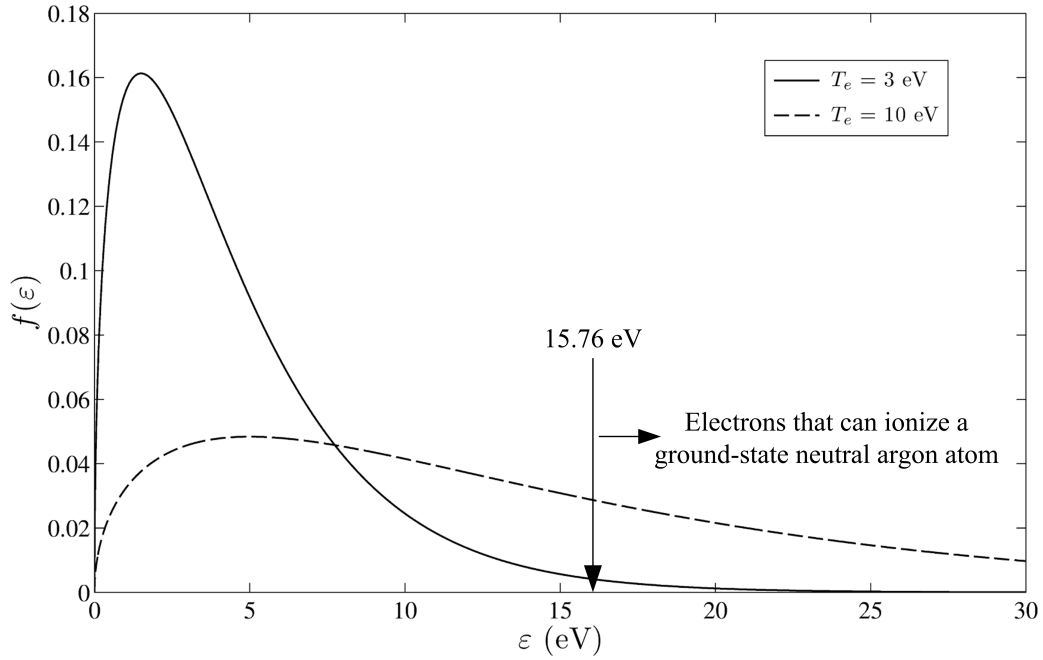

Figure 3.8: Maxwellian electron energy distributions for 3 eV & 10 eV electron populations. At higher electron temperatures, a higher fraction of electrons can participate in ionization.

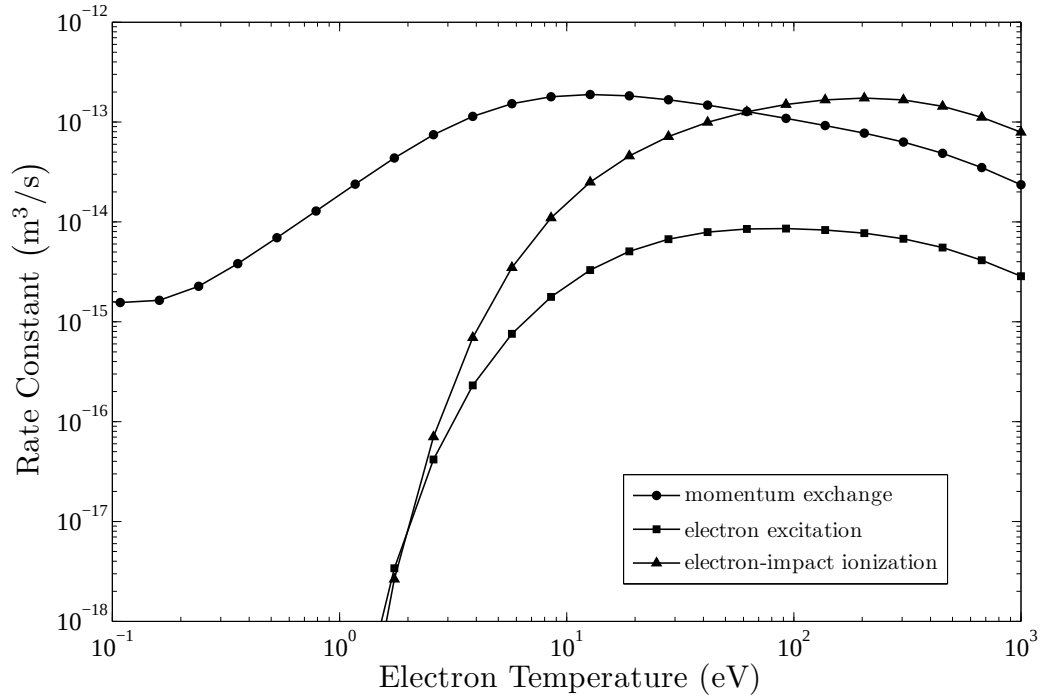

Figure 3.9: Argon rate constants versus electron temperature. Note that the rate constants eventually decrease with increasing electron temperature because cross-sections are dependent on the interaction energy.

3.2.1 Magnetic Field Interactions

As previously discussed, both electric and magnetic fields can be used to exert a force on a charged particle. Although magnetic fields do not influence stationary charged particles, the probability of a stationary particle existing within a plasma is zero. Another important equation when considering charged particle motion in a magnetic field is Eq. 3.44, which states that no magnetic monopoles may exist in nature. Physically, this means that a static magnetic field cannot deposit power into the plasma.

$$\nabla \cdot \vec{B} = 0 \tag{3.44}$$

As shown previously in Eq. 3.25, a magnetic field can only impose a force that is perpendicular to both the charged particle direction of motion and the magnetic field direction. Therefore, in the absence of an electric field, a single charged particle in a uniform magnetic field will travel unimpeded parallel to the magnetic field, but will only travel in circles perpendicular to the magnetic field. This means that the average motion of the plasma across the magnetic field can be severely restricted compared to motion along the magnetic field, and so the properties of a magnetized plasma can be highly anisotropic. For ease of analysis, the coordinate system for the magnetized plasma is typically transformed to be aligned with the magnetic field. Thus, rather than using the Cartesian velocity components, (v_x, v_y, v_z), the plasma is typically described by the velocity components that are parallel and perpendicular to the magnetic field, ($v_\parallel$, $v_\perp$).

Plasma is a diamagnetic material. Thus, the circular motion of the charged particles about the magnetic field lines acts to oppose the applied magnetic field. The circular motion has an associated characteristic time scale called the *cyclotron frequency* or *gyrofrequency*, ω_c, that is calculated according to Eq. 3.45.

$$\omega_c = \frac{qB}{m} \tag{3.45}$$

The circular motion also has a length scale called the *Larmor radius* or *gyroradius*, r_L, that is calculated according to Eq. 3.46.

$$r_L = \frac{v_\perp}{\omega_c} \tag{3.46}$$

If the length scale of the plasma system transverse to the magnetic field is larger than a few gyroradii, and the plasma resides in the magnetic field for more than a few cyclotron periods, then the plasma in the system is said to be *magnetized*. Typically, the perpendicular velocity is assumed to be equal to the thermal velocity, and the ions are assumed to be singly-charged. With these assumptions, the gyroradius is proportional to $\sqrt{mT}/B$. Since the ions are much more massive than the electrons, the ion gyroradius is typically much larger than the electron gyroradius, even in a non-thermal plasma (i.e. $r_{L,i} \gg r_{L,e}$). This means that the plasma electrons may be magnetized in a system where the ions remain non-magnetized.

Theoretically, The guiding center of motion for a charged particle in a uniform magnetic field cannot cross the magnetic field lines. However, there are many particles in a real plasma, and collisional interactions can "bump" the charged particles across the magnetic field. If collisional interactions occur at a faster rate than the electron cyclotron frequency (i.e. $\nu_m \gg \omega_c$), then the effects of the magnetic field are unimportant for charged particle transport. The same is true if the length scale of the system perpendicular to the magnetic field is much smaller than the electron gyroradius.

The diffusion coefficient and mobility previously given by Eqs. 3.40 and 3.41 described charged particle transport in the absence of a magnetic field. These equations still hold when describing motion parallel to magnetic fields. In order to describe particle transport perpendicular to a magnetic field, the equations must be modified according to Eq. 3.47.

$$(D,\, \mu)_\perp = \frac{(D,\, \mu)}{1 + \left(\frac{\omega_c}{\nu_m}\right)^2} \tag{3.47}$$

Because the individual coefficients may be very different for ions and electrons, the perpendicular coefficients are typically combined to give a coefficient that describes the net transport of both ions and electrons across the magnetic field lines, called the *cross-field ambipolar diffusion coefficient*, $D_{\perp,a}$, and given by Eq. 3.48.

$$D_{\perp,a} = \frac{\mu_{\perp,i} D_{\perp,e} + \mu_{\perp,e} D_{\perp,i}}{\mu_{\perp,i} + \mu_{\perp,e}} \tag{3.48}$$

Assuming the ion mobility is much greater than the electron mobility, the cyclotron frequency is much greater than the electron collision frequency, and the electron temperature is much greater than the ion temperature, an expression for the cross-field diffusion of electrons is given by Eq. 3.49 [84].

$$D_{\perp,e} = 1.66 \times 10^{-12} \frac{n_e}{T_e^{1/2} B^2} \text{ in } \frac{\text{m}^2}{\text{s}} \tag{3.49}$$

One active area of EP research is the use of a magnetic field that is aligned with the thrust axis. This arrangement is sometimes referred to as a *magnetic nozzle* because the behavior in such devices is described similarly to a converging/diverging gasdynamic nozzle [85]. The issue that is of greatest concern for magnetic nozzles is the detachment of the plasma from the magnetic field [86, 87]. As previously discussed, Eq. 3.44 states that a static magnetic field cannot impart energy to a plasma. Equation 3.44 also states that magnetic fields only exist as closed surfaces. Thus, in an EP system with a magnetic field parallel to the thrust axis, the magnetic field must curve around and impinge somewhere on the spacecraft. A detailed study of the physics in the diverging part of the magnetic field is beyond the scope of this dissertation. However, the assumptions that must hold in order for a plasma to be magnetized are noted here. Besides the collision frequency and length scale considerations previously mentioned, the magnetic field must change slowly relative to the streaming motion of the charged particles in the plasma. This assumption is given by Eqs. 3.50 and 3.51, where s is the distance coordinate along the charged particle trajectory.

$$\frac{\partial B}{\partial t} \ll \frac{1}{\omega_c} \tag{3.50}$$

$$\vec{v}\frac{\partial B}{\partial s} \ll \frac{1}{\omega_c} \tag{3.51}$$

The effects of high curvature, low magnetic field strength, low pressure, and low plasma temperature may cause complicated drift motions to exist in the exit and detachment regions of magnetic nozzle devices. In regions of the plasma where the magnetic fields are sharply curved, there are drift motions associated with ∇B drift and curvature drift that may cause the plasma to exhibit anomalous transport behavior. Most of these drift motions will enhance the plasma's cross-field mobility.

3.2.2 RF Plasma

In order to impart energy to the plasma, an electric field is applied to exert a force on the electrons and ions. Accelerated electrons interact with the heavy particles through collisions, which cause momentum transfer, excitation of higher electron energy modes, and ionization. These collisional processes occur at rates related to the densities of the interacting particles, and the rate constants may calculated using Eq. 3.43. The electric field may be applied either by a DC electric field, or an oscillating voltage or current, for example at a frequency ω. For plasmas excited by the application of RF voltages and currents, stochastic or collisionless heating in the sheath can also impart energy to the electrons [88].

The properties of the plasma can be affected by the coupling mode by which RF energy is imparted to the electrons. Three main coupling modes are typically described in the literature: capacitive coupling, inductive coupling, and wave coupling. Textbooks discuss the details of the physical mechanisms present in each, for example by Lieberman and Lichtenberg [88].

Capacitively coupled plasmas are characterized by high voltage sheaths, high electron temperatures, and low plasma densities. Electrode materials are typically in direct contact with the plasma, and so ion bombardment can sputter electrode materials into the bulk plasma. This may cause two undesired effects: 1) erosion or slow disintegration of the discharge driving electrodes, and 2) introduction of undesired material into the discharge or plasma process.

Inductive plasmas couple energy into the electrons through an oscillating magnetic field. A large, time-varying current is driven through an antenna, and the axial magnetic field produced by this current couples to the plasma through an azimuthal electric field that is created due to Faraday's law, given in Eq. 3.52.

$$\nabla \times \vec{E} = -\frac{\partial \vec{B}}{\partial t} \tag{3.52}$$

Inductively coupled plasmas typically have higher plasma densities and much colder electron population than capacitive plasmas. The antenna for an inductively coupled plasma is generally not in contact with the plasma, eliminating many of the sputtering and erosion problems of capacitive plasmas. However, due to lower voltage sheaths, it is generally more difficult to initiate an inductive discharge.

As previously discussed, plasma naturally has oscillatory behavior at frequencies dependent on the properties of the plasma. Wave-heated plasma sources use this oscillatory behavior to couple power into the ions and/or electrons by exciting resonances at the natural oscillation frequencies. Textbooks describe the multitude of waves that naturally occur in plasmas, for example by Stix [89].

Helicon plasma sources generate one example of a wave-heated plasma. Helicon waves are bounded, right-handed, circularly polarized electromagnetic waves that propagate along a magnetic field [90]. Helicon plasma sources generally consist of a cylindrical insulating dielectric tube surrounded by an antenna and solenoid magnets. A gas fills the tube, typi-

cally to a pressure of approximately one millitorr. RF power is applied to the antenna, typically at 13.56 megahertz, and the solenoids apply a magnetic field parallel to the center axis of the tube. The shape of the antenna is designed specifically to excite helicon wave modes in the ionized gas. Particle-wave interactions from Landau damping and Trivelpiece-Gould coupling deposit the RF power into the plasma species [91].

Helicon plasma sources have been studied since the 1960's, with early studies focusing on their ability to efficiently produce high-density, low-temperature plasma for materials processing [92, 93]. The theory of helicon wave propagation assumes that the RF driving frequency is high enough such that ion motion can be neglected, but low enough such that electron cyclotron motion can be neglected. The axial wavelength of the helicon wave, λ_z, is determined by the axial magnetic field strength, B_z, the RF driving frequency, f_{RF}, and the density of the plasma, n_e, according to Eq. 3.53, where e is the elementary charge and μ_0 is the magnetic permeability of free space.

$$\lambda_z = \left(\frac{2\pi B_z}{e\mu_0 n_e f_{RF}} \right)^{1/2} \tag{3.53}$$

Note that the RF driving frequency is set by the power supply. Typically, a half-wavelength-long antenna is employed with the intent to ionize the gas in the dielectric tube to a density based on the applied axial magnetic field strength. Although most helicon experiments use a cylindrical geometry, previous work also demonstrated the operation of an annular helicon plasma source [94]. Theoretical considerations of annular helicon waves suggest that the maximum power deposition requires careful antenna design and choice of frequency [95].

CHAPTER 4

Thrusters

In order to investigate whether air-breathing EP may benefit from the implementation of RF plasma technology, measurements of the performance of two thrusters were taken at the Plasmadynamics and Electric Propulsion Laboratory (PEPL) at the University of Michigan. The thrusters were chosen based on the likelihood that they have the appropriate performance characteristics for an air-breathing propulsion system. This chapter describes the two thrusters that were tested. The first thruster is the Radio frequency Plasma Thruster (RPT). The RPT is designed primarily based on helicon plasma source scaling. The second thruster is the Helicon Hall thruster (HHT). The HHT is a two-stage thruster that employs an RF ionization stage intended to increase the performance of a Hall thruster operating at high thrust-to-power. This chapter describes the two thrusters in detail.

4.1 Radio frequency Plasma Thruster

Much development work toward using helicon plasma sources in EP systems has been performed. Some of this work involves the use of a helicon source alone as a thruster [71, 73, 96, 97], while other efforts attempt to use the helicon source as an ionization stage with a separate acceleration stage [69, 98, 99]. Helicon sources operating with argon have been measured to produce ion beams at energies that correspond to an approximately 30-volt ion acceleration [75, 100, 101]. Recalling the results from Chapter 2, this means that the exhaust velocity of a helicon plasma source is in the range desired for an air-breathing

propulsion system. Although most helicon experiments focus on the use of argon in order to simplify analysis of the physics, measurements also suggest that helicon plasma sources are able to accelerate other gases, including nitrogen [102]. One major benefit of helicon plasma sources is that they do not require a thermionic cathode to operate. As previously discussed, this mitigates any materials compatibility issues that would be present in other types of EP thrusters operating as an air-breathing propulsion system.

The Radio frequency Plasma Thruster (RPT) is a propulsion device that is designed to excite a helicon wave in the propellant gas. The helicon wave is only excited in an axial magnetic field. Equation 3.53 implied that a stronger magnetic field enables the production of higher plasma densities. A stronger axial magnetic field also insulates the plasma from the thruster, potentially improving thruster lifetime. However, in order to produce thrust, the plasma generated by the RPT must detach from a diverging axial magnetic field in the exhaust region. How the magnetic field shape and strength affects plasma detachment and thruster efficiency is an active area of research [85–87]. So, the RPT is designed to be capable of producing a wide range of magnetic fields.

4.1.1 Preliminary Investigations

In order to determine whether a helicon source may be appropriate for use as a plasma thruster with atmospheric gases, a helicon source was first constructed at PEPL to take measurements of plasmas created with argon, nitrogen, and air. This helicon source is shown operating with argon in Fig. 4.1.

Most helicon experiments operate with argon. It is commonly known that the presence of a "blue core" in the plasma column indicates that helicon-mode operation has been achieved. The "blue core" refers to light in the blue wavelengths of the visible spectrum, which is produced by intense emission from argon ions (Ar II) that are created by the helicon wave coupling to the plasma [103, 104]. Figure 4.2 shows photographs and emission spectra of argon operation with and without a blue core. The appearance of a blue core gave

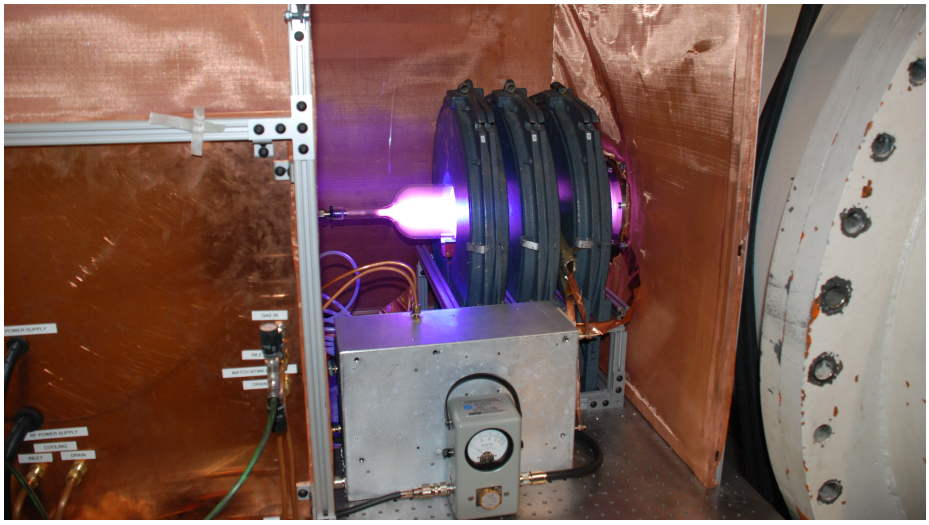

Figure 4.1: Setup of the helicon plasma source used for preliminary investigations. The source is operating in helicon-mode with argon in the photograph.

a strong indication that helicon waves were excited in the preliminary helicon experiments at PEPL. One method for confirming that helicon waves are present is by using a B-dot probe to measure the RF-magnetic-field fluctuations induced in the plasma by the helicon wave [105].

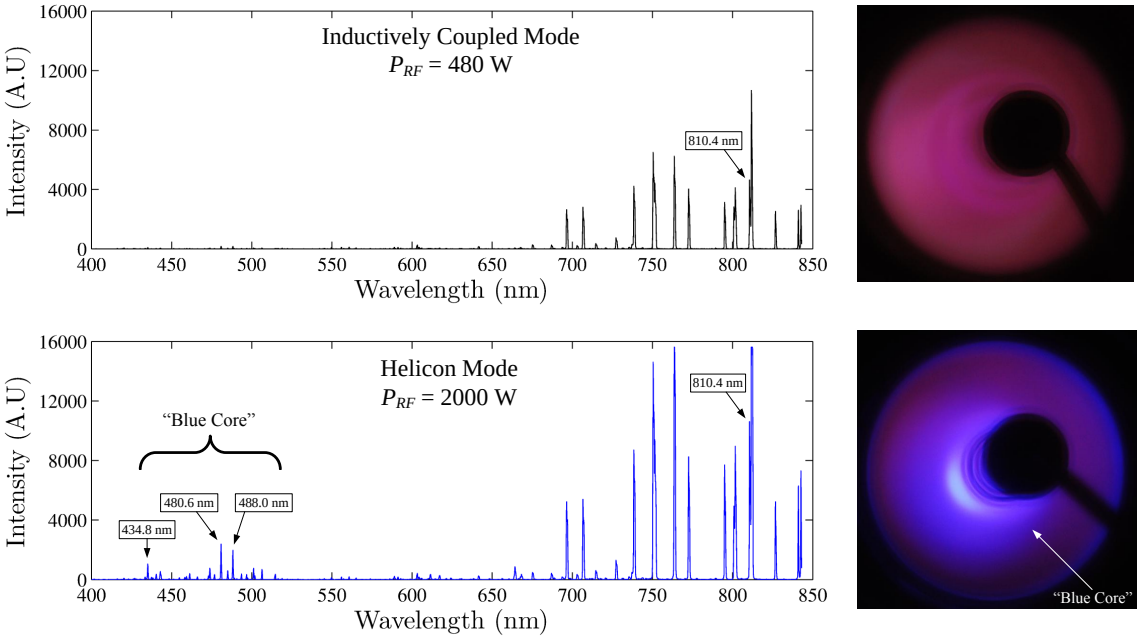

Figure 4.2: Optical emission spectra and photographs of helicon "blue core" in argon. Known argon ion lines are identified [106]. Photographs look along the center axis of the glass tube shown in Fig. 4.1, along the center axis of tube.

Although less pronounced than with argon, visible changes in the plasma indicated that higher coupling modes may also be achieved with nitrogen. Changes in the shape of the plasma when operating with nitrogen at higher powers correlated with the appearance of additional peaks in the emission spectra, as shown in Fig. 4.3. This gave an indication that a higher ion density was being produced. As was previously discussed, the appearance of a blue core in an argon helicon plasma is due to the emission spectrum of argon ions. The most intense emission lines of diatomic nitrogen ions are in the ultraviolet part of the spectrum [107]. Thus, any core structure may not have been readily visible.

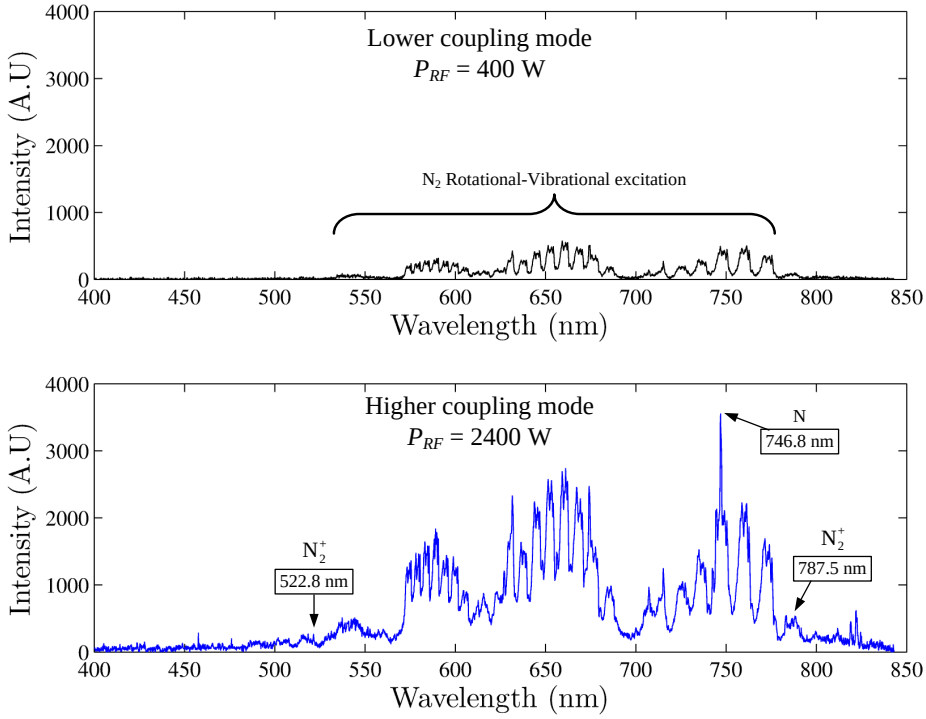

Figure 4.3: Optical emission spectra looking along center axis of tube during nitrogen operation at low (top) and high (bottom) power. Rotational-vibrational modes of neutral N_2 are excited at both low and high powers. Molecular nitrogen ion lines appear at high power. A strong neutral atomic nitrogen line may indicate dissociative recombination of N_2^+ [107–111].

4.1.2 RPT Design

The RPT is designed to test whether a helicon plasma source can be an effective thruster for the purpose of enabling a long-lived, air-breathing spacecraft. Using the air-breathing

spacecraft and atmospheric model from Chapter 2, a spacecraft with a one-square-meter inlet area in a circular orbit between 170 and 230 kilometers has an inlet mass flow rate of approximately 1 to 7 milligrams per second. This corresponds to a number flow rate, $\dot{n}$, of about 3.0×10^{16} to 1.8×10^{17} per second. Because most helicon plasma sources in the laboratory operate at a pressure of approximately 1 millitorr, the diameter of the tube is sized such that the operating pressure in the tube is one millitorr. When testing in the laboratory, the propellant flows from a compressed gas cylinder, and so the inlet temperature of the gas, T_g, is approximately room temperature, 290 degrees kelvin. Thus, the diameter of the helicon source tube should be 4 to 11 centimeters to operate at the number density of a typical helicon experiment with either argon or nitrogen propellant.

The magnetic field strength and antenna length are chosen based on the helicon wavelength scaling from Eq. 3.53 and the approximate number density in the source tube. Taking the RF driving frequency to be 13.56 megahertz, and assuming that 10% of the propellant will be ionized at any given time, the helicon wavelength, λ_z, follows the scaling given by Eq. 4.1, where B_z is the axial magnetic field strength.

$$\lambda_z[m] = 0.83\sqrt{B_z[T]} \tag{4.1}$$

A 10% ionization fraction is high for conventional low-temperature plasmas. However, this is not an unreasonable estimate for designing the RPT based on Langmuir probe measurements in other helicon plasma sources [84]. Equation 3.53 showed that higher plasma densities can be achieved for a given helicon wavelength with a higher magnetic field. Previous studies have also suggested that longer antennas may have higher coupling efficiencies. However, the solenoid coils that produce the magnetic field are made of copper, and due to the relatively large diameter of the source tube, an engineering trade study must be made to compromise between the magnetic field strength, the weight of the magnet assembly, and the price of the copper magnet wire. For the RPT, the compromise is made

at a magnetic field strength of 0.1 tesla, or 1000 gauss. At this magnetic field strength, the dominant m = +1 helicon mode has an axial wavelength of 26 centimeters.

Table 4.1: RPT Design Summary.

Property	Value
Inlet	$A_{inlet} = 1$ m^2
Altitude	$h = 170$–230 km
Mass Flow Rate	$\dot{m}_{pr} = 1$–7 mg/s
Operating Pressure	$P_{tube} = 1$ mTorr
Driving Frequency	$f_{RF} = 13.56$ MHz
Helicon Wavelength	$\lambda_z = 26$ cm
Magnetic Field	$B_z = 0.1$ T

4.1.3 RPT Assembly

The RPT is an assembly of six solenoid coils surrounding a quartz tube and an antenna, and surrounded by a low-carbon steel case. A cross-section of the RPT is shown in Fig. 4.4.

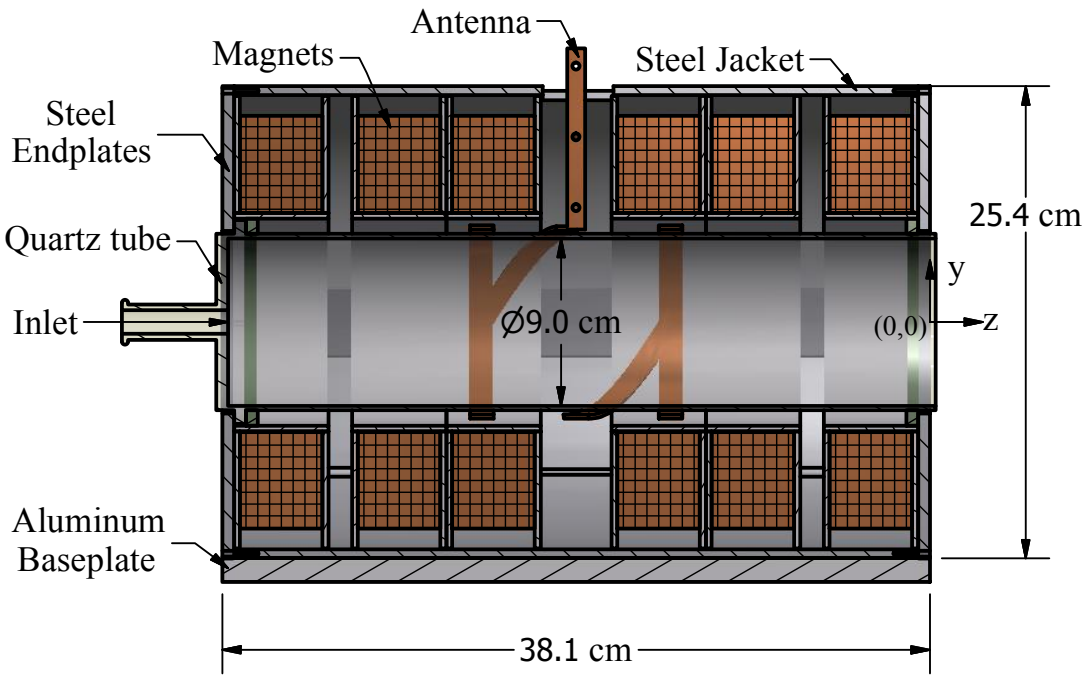

Figure 4.4: Cross-section of the RPT with major components and dimensions labeled.

The RPT is designed to be a cohesive unit, such that all the components, including the magnets, quartz tube, and antenna, are fixed in place relative to each other. This design feature is unique to the RPT among other RF/helicon thruster experiments [70, 71, 112]. The RPT is also designed as a rapidly reconfigurable experiment, such that the internal components can be replaced with relative ease. An exploded view of the RPT components is shown in Fig. 4.5.

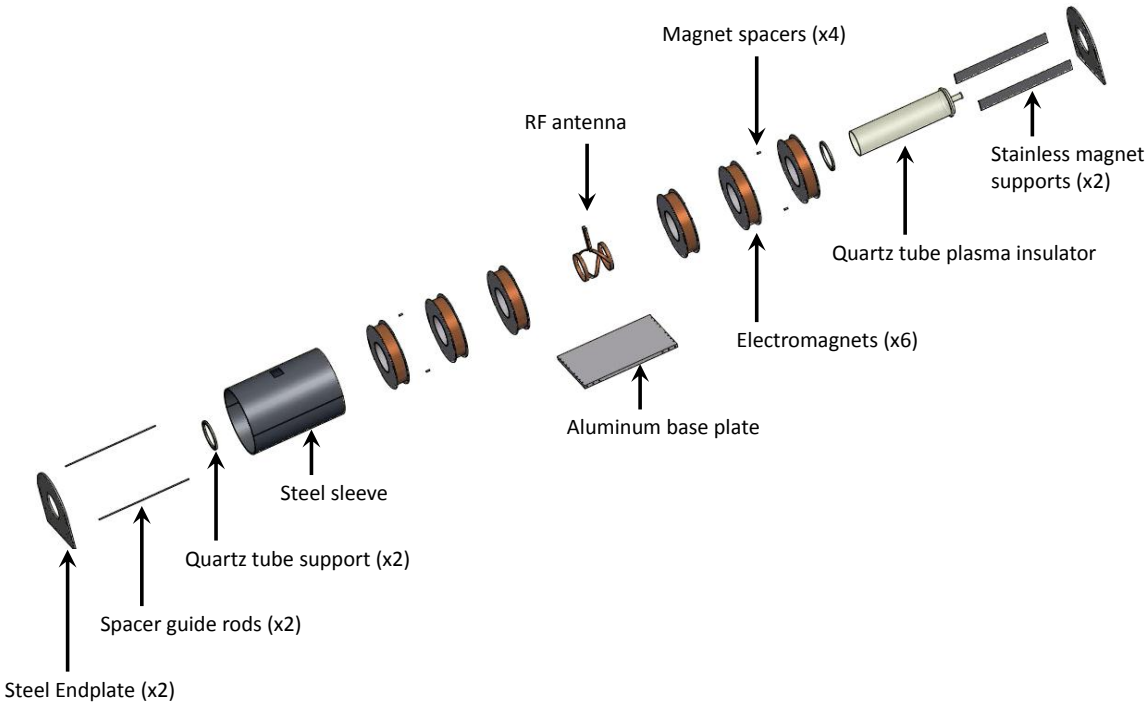

Figure 4.5: Exploded view of the RPT. A flexible mica sheet that surrounds the antenna is not shown.

The low-carbon steel case enhances the magnetic capabilities of the RPT. The steel case increases the magnetic field strength and uniformity in the quartz tube, and also enables a steep magnetic field gradient to be generated at the exit of the quartz tube. The magnet assembly, including the solenoids and the steel case, is capable of producing a uniform axial magnetic field up to 0.11 tesla in the quartz tube. Although the performance measurements reported in this dissertation refer to simulated magnetic field strengths, measurements of the magnetic field profile were collected at atmospheric pressure for multiple solenoid cur-

rents with a Lake Shore Cryotronics Model 460 3-channel Gaussmeter, and the measured magnetic fields were less than $\pm 1\%$ different from the simulated fields [96].

The RPT quartz tube has an inner diameter of 9.0 centimeters and an internal length of 38.1 centimeters, and it electrically isolates the plasma from the antenna and magnets. The antenna is a bifilar, half-turn helical antenna (also known as a "Twisted Nagoya" antenna) that is intended to excite the m = +1 helicon wave [113]. Shown in Fig. 4.6, the antenna is machined from a single piece of copper, and it has two copper leads that extend from the RPT body. The leads are welded directly to the antenna where a short section in the center of one of the helical sections is removed. Although not shown in the exploded view, multiple layers of flexible mica sheet hold the antenna tightly in the center of the magnet assembly.

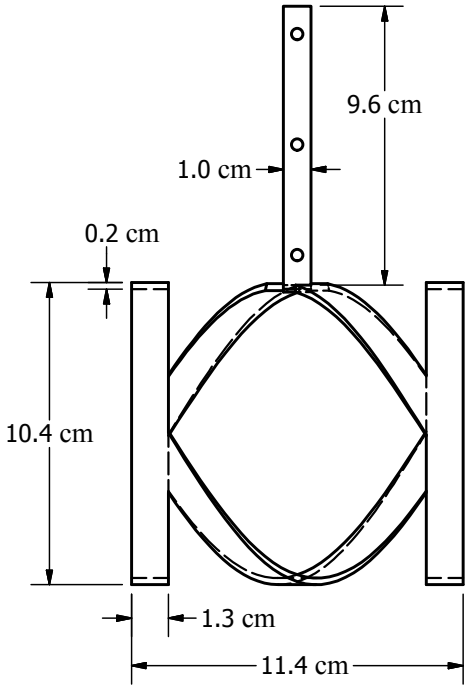

Figure 4.6: RPT antenna details.

4.2 Helicon Hall Thruster

Hall thrusters were first employed in space by the former Soviet Union in the 1970's, but it was not until the early 1990's that significant Hall thruster development work occurred in the United States [114]. Current Hall thruster research activities primarily focus on improving thruster lifetime [54], using propellants other than the traditional xenon [115, 116], increasing the power and thrust density [117, 118], and extending the range of performance [119, 120]. The success seen by many of these research efforts show that Hall thrusters are a robust and versatile technology.

As previously discussed, an air-breathing thruster would be practical to implement on a mission with a long lifetime. However, Hall thrusters have well-characterized life-limiting mechanisms due to the erosion of thruster materials. Recent experiments have shown that a Hall thruster can be operated in such a way that the erosion is dramatically reduced, implying that Hall thruster lifetime can be significantly increased [55]. Although this work has only been performed with xenon, the concept may also be possible with other gases. If Hall thruster lifetime can be extended with nitrogen and oxygen in particular, then Hall thrusters are a much more viable propulsion option for an air-breathing spacecraft.

The Helicon Hall Thruster (HHT) was designed to improve the total efficiency of a Hall thruster operating at high thrust-to-power with xenon. For Hall thrusters, "high thrust-to-power" is synonymous with low-voltage operation. At the lowest feasible altitudes for an air-breathing spacecraft, the acceleration voltage required to compensate for drag is very low for a typical Hall thruster. Thus, the HHT is designed to operate closer to the operating parameters of an air-breathing EP system than a typical Hall thruster.

The performance characteristics of Hall thrusters operating with alternative propellants are not well-characterized. The efficiency and thrust of a traditional Hall thruster is much lower when operating with alternative propellants simply due to the higher ionization energy and lower mass of the lighter propellant species. In order to investigate whether the performance characteristics of a Hall thruster operating with atmospheric gases can be im-

proved, the HHT was operated with argon and nitrogen propellant. The HHT Hall acceleration stage was operated with the RF ionization stage to determine if the overall efficiency can be increased at high thrust-to-power. This section briefly describes the principle of HHT operation, and discusses the novel design features of the HHT.

4.2.1 HHT Principle of Operation

The HHT is a two-stage Hall thruster concept that is designed to utilize the efficient ionization of a helicon plasma source with the acceleration mechanism of a Hall thruster. In particular, the HHT was designed to excite annular helicon wave modes in the plasma in the upstream section of the discharge chamber of a Hall thruster [121]. Figure 4.7 shows an illustration of the HHT cross-section with the major components labeled.

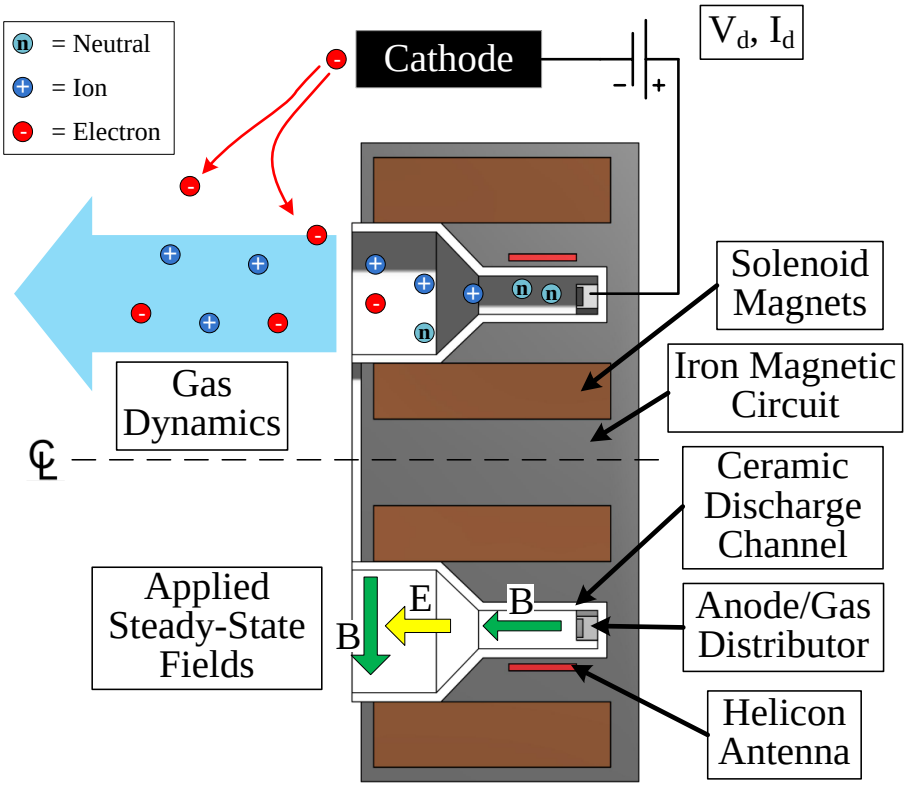

Figure 4.7: HHT notional sketch. The first stage of the HHT uses an axial magnetic field and antenna to excite helicon waves in the propellant. The second stage uses a radial magnetic field in a traditional Hall accelerator configuration.

In the first stage, RF power is applied to the helicon antenna to ionize the neutral propellant flowing out through the gas distributor. An applied axial magnetic field in the same region allows the antenna to couple annular helicon waves into the ionized propellant just downstream of the gas distributor. The excitation of helicon waves is intended to increase both the ionization efficiency and the propellant utilization efficiency.

In the second stage, a radial magnetic field and a voltage applied between the anode and an external hollow cathode create a traditional Hall accelerator. Electrons emitted from the hollow cathode neutralize the ion beam exiting the discharge channel. Some electrons also travel into the discharge channel, where they become trapped by the radial magnetic field. These trapped electrons concentrate the axial electric field into a thin region of the discharge channel. Note that the topology of the magnetic field is critical to the efficient operation of the HHT.

4.2.2 HHT Assembly

The HHT was designed mainly at ElectroDynamic Applications, Inc., with partners from Aerojet [119, 122]. Figure 4.8 shows a photograph of the assembled HHT. The Hall acceleration stage of the HHT is designed to use auxiliary electrodes with the external hollow cathode. The auxiliary electrodes are not shown in the notional diagram in Fig. 4.7, but they are in place in the photograph in Fig. 4.8.

4.2.3 Previous Work

The first two-stage performance measurements of the HHT operating with xenon propellant suggested that the performance was improved when applying higher levels of RF power to the helicon antenna [122]. Upon further investigation, the possibility arose that the RF power delivery system was improperly implemented, and that the thrust measurements may have been affected by Electromagnetic Interference (EMI). So, a follow-on study was performed with a different RF power delivery system to confirm the original results.

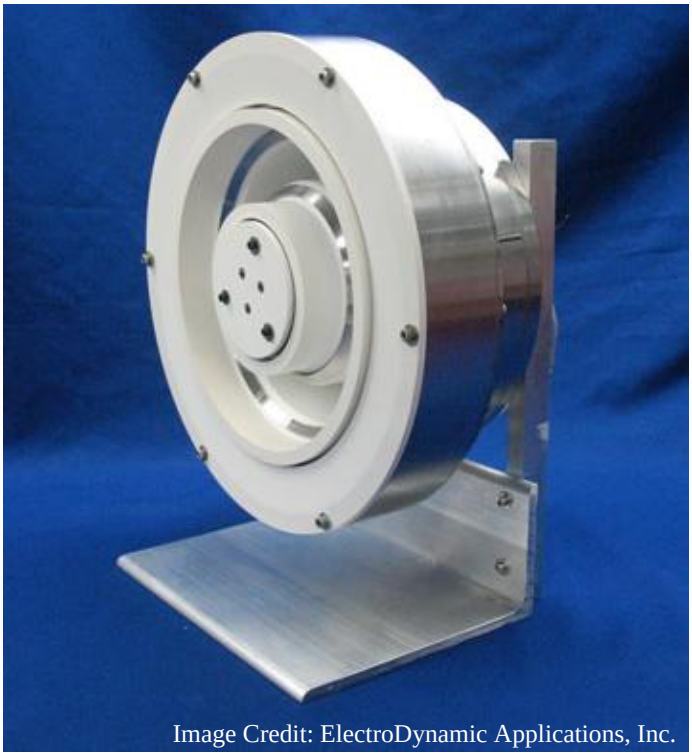

Figure 4.8: Photograph of HHT.

During the follow-on study, the auxiliary electrodes were removed, and the propellant distributor was used as the Hall accelerator anode. The results presented in this dissertation were taken during the follow-on study. The follow-on study repeated and further investigated some of the original xenon operating conditions. The performance of the HHT operating with argon and nitrogen was also measured during the follow-on study.

CHAPTER 5

Experiment Setup

The RPT and HHT are experimental space propulsion systems, and so all experiments are performed in a vacuum chamber to simulate the space environment. A very low background pressure and far-removed chamber walls are desired to reduce any facility effects that would not be present in space. Because both thrusters under investigation use RF power, the RF engineering principles described in Chapter 3 were followed when implementing the RF power delivery system. This chapter describes the vacuum facility, the RF power delivery system, and the diagnostics used to characterize the RPT and HHT.

Plasma properties in the exhaust plume were measured concurrently with thrust and telemetry. The performance parameters of thrust, specific impulse, and efficiency were determined by the propellant mass flow rate, the force measured by an inverted-pendulum thrust stand, the net RF power measured by a dual-directional coupler, the and thruster telemetry data. The plasma plume properties of interest include the total ion beam current, the ion beam average kinetic energy, and the exhaust plume divergence. These properties are determined measured with a nude Faraday probe, a Retarding Potential Analyzer (RPA), and a commercial Langmuir probe.

5.1 Test Facility

All experiments were performed in PEPL's Large Vacuum Test Facility (LVTF) at the University of Michigan. The LVTF is a 6-meter diameter by 9-meter long cylindri-

cal, stainless-clad steel vacuum chamber. Seven CVI TM-1200 nude (reentry) cryopumps maintain the pressure in the LVTF with a combined pumping speed of 500,000 liters per second on air or 245,000 liters per second on xenon. The pressure in the LVTF is measured by a nude Bayert-Alpert ionization gauge. A Varian model XGS-600 gauge controller powers the ionization gauge and reads out the measured pressure. The corrected chamber pressure, p, is calculated from Eq. 5.1, where p_{ob} is the pressure indicated by the XGS-600, p_b is the base (no load) pressure, and C_{gas} is the gas correction factor.

$$p = \frac{p_{ob} - p_b}{C_{gas}} + p_b \tag{5.1}$$

The gas correction factor is 1.20 for argon, 2.87 for xenon, and 1.00 for nitrogen. During the experiments reported in this dissertation, the LVTF base pressure was measured to be 7.4×10^{-8} Torr.

5.2 RF Power System

As the previous discussion of RF engineering principles implied, the details of the implementation of the RF power delivery system are critical to properly characterize the thruster efficiency. A diagram of the RF electrical setup in the LVTF is shown in Fig. 5.1.

The goal of the RF power transmission system is to transfer as much energy as possible from the RF generator to the plasma. As previously discussed, any RF power system with a standard 50-Ω characteristic impedance that delivers power to a non-50-Ω load requires a matching network to transform the load impedance to 50 Ω. Otherwise, a large impedance discontinuity at the load will cause most of the incident RF power to be reflected back the transmission line toward the generator. The impedance of an antenna-and-plasma load is generally different for different thruster operating conditions and coupling modes (e.g. capacitive, inductive, helicon). Thus, a manually-tunable matching network was implemented to compensate for the anticipated range of load impedances.

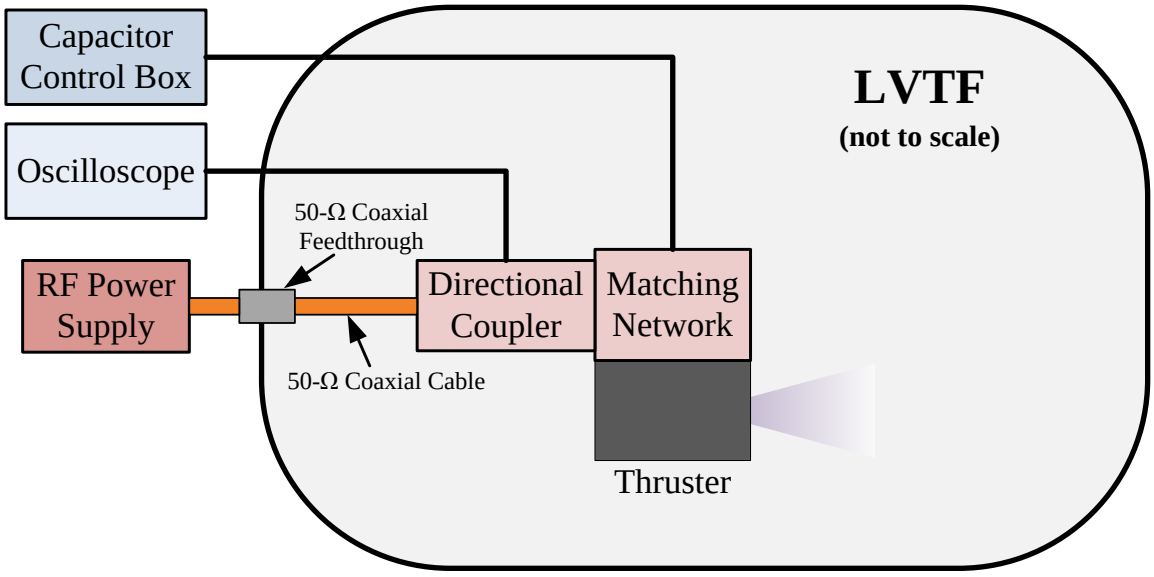

Figure 5.1: Diagram of the RF power system in LVTF. A 50-Ω system is maintained from the RF power supply to the matching network. The matching network directly connected to the thruster antenna, but manually controlled with an external control box.

For the RF power system implemented in the LVTF, a Comdel model CPS-3000 RF generator supplies power at a fixed frequency of 13.56 megahertz and a 50-Ω output impedance. The maximum output power of the CPS-3000 is 3000 watts. The CPS-3000 has an internal protection circuit that automatically limits the forward power output when reflected power exceeds 600 watts. Standard 50-Ω RG-213 coaxial cable carries the RF power from the CPS-3000 output port to a hermetically-sealed, 50-Ω bulkhead connector at the LVTF wall that acts as a vacuum feedthrough. Inside the LVTF, a 5-meter length of 50-Ω RG-393 coaxial cable transmits the RF power from the feedthrough to the thrust stand support structure. To minimize forces on the thrust stand due to thermal expansion of the RF cable, the final connection to the the matching network is made with a 0.66-meter length of RG-393 that is arranged perpendicular to the thrust axis. Thus, a 50-Ω system is maintained from the RF generator to the matching network on the thrust stand. This is a feature that is unique to the RF power delivery system at PEPL.

No coaxial cable is perfectly lossless, and so a small amount of the RF power will be dissipated in the cable, leading to cable heating. At any given forward power, the amount

of power dissipated in a coaxial cable increases with increasing reflected power [123]. Thus, an RF power delivery system aims to minimize reflected power not only to increase the efficiency of the system, but also to prevent the coaxial cable from overheating. To ensure that the cable does not approach its maximum temperature rating of 200 degrees celsius, three thermocouples are placed on the outside of the RG-393 RF power cable, and the measured temperatures are monitored throughout the experiment. The thermocouple measurements were slightly affected by EMI when RF power was turned on with either the RPT or HHT. However, the thermocouples returned to normal operation when the RF power was shut off.

Without a matching network, very little power will be delivered to the plasma because the impedance of the antenna-and-plasma system is typically quite different than 50 Ω. In most RF systems, the forward and reflected power are measured inside the generator or in a 50-Ω transmission line section upstream of the matching network input port. The power that is transmitted downstream of the matching network may be dissipated, radiated, or coupled away from any conductor that is connected to the matching network output leads. Without a direct measurement of the current and voltage at the antenna input leads, the actual power delivered to the antenna is unknown.

In order to increase the likelihood that the RF power measured at the matching network input port represents the power delivered to the thruster antenna, the matching network is placed on the thrust stand and connected to the antenna with the shortest output leads possible. Following the one-tenth RF wavelength guideline discussed in Chapter 3, the short output length scale decreases the probability of power radiating or coupling away prior to the antenna. Furthermore, all RF electrical connections in the matching network are made with a large surface area to minimize contact resistance, and low-loss matching capacitors are used to minimize dissipation in the matching circuit components. A photograph of the RPT setup in the LVTF is shown in Fig. 5.2, with the matching network, directional coupler, and RF power delivery cable indicated.

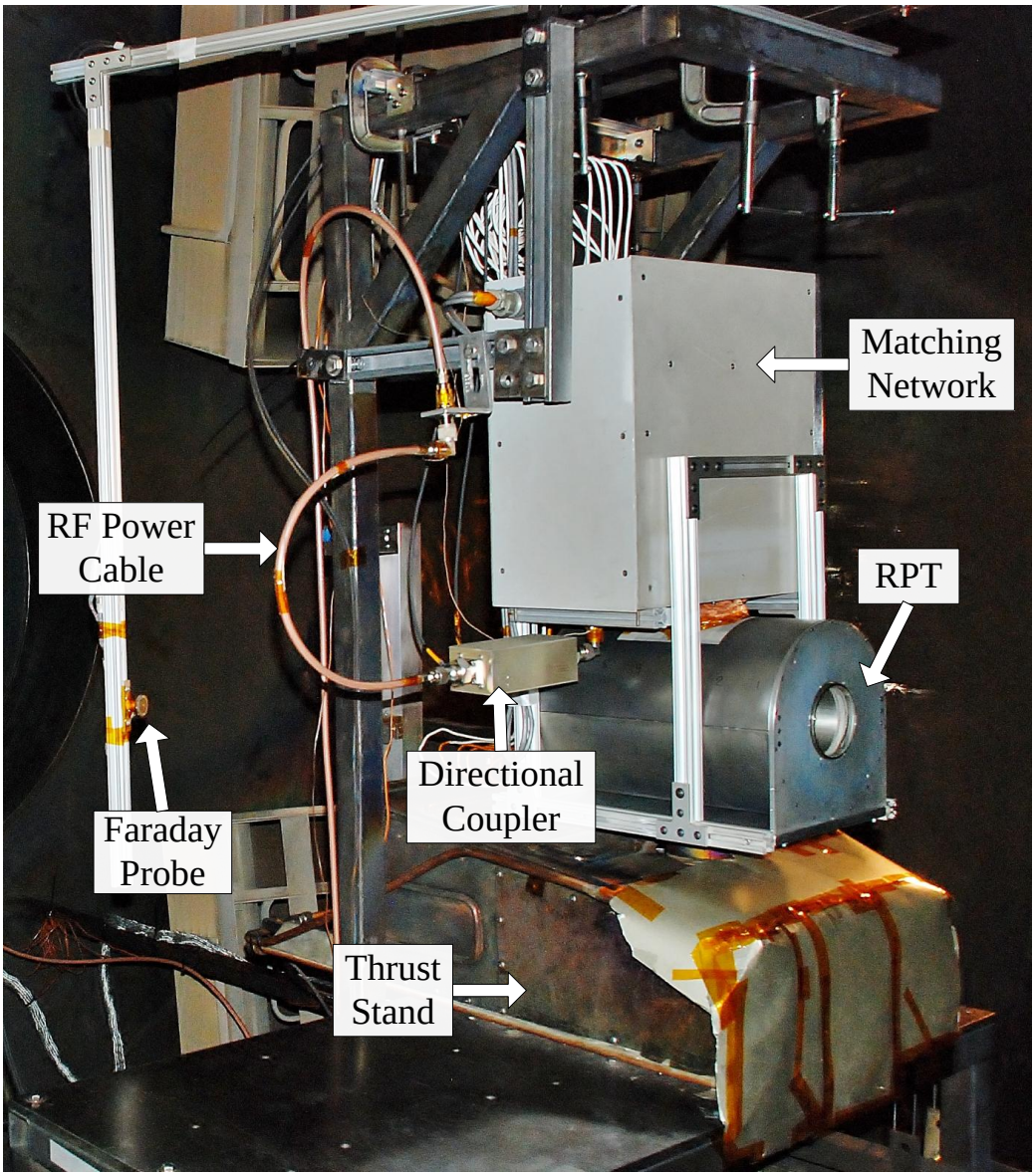

Figure 5.2: Photograph of the RPT experimental setup in the LVTF.

The matching network used to couple power to the RPT and HHT antennas is in an L-type configuration. Two vacuum variable capacitors in the matching network are manually adjusted using DC motors that are remotely controlled from outside the LVTF. The shunt or "load" capacitor is a vacuum variable capacitor manufactured by Comet. The measured capacitance range of the load capacitor is 50 to 1150 picofarads. The series or "tune" capacitor is a Jennings model UCS-500-15S, with a measured capacitance range of 25

to 500 picofarads and a withstanding voltage rating of 15 kilovolts. The range of output impedances that the matching network can provide is designed to encompass the conjugate of the vacuum impedance of the antenna, which was measured to be $(0.001 + 13.6j)\Omega$ at 13.56 megahertz using an Agilent E5071C network analyzer.

5.3 Diagnostics

The plasma properties in the thruster exhaust plumes are measured concurrently with performance. The performance parameters of thrust, specific impulse, and efficiency are determined by the propellant mass flow rate, the force measured by an inverted-pendulum thrust stand, and the net RF power measured by a dual-directional coupler. The measured plume properties include the total ion beam current, ion beam kinetic energy, and exhaust plume divergence. These properties are determined with a nude Faraday probe, an RPA, and a commercial Langmuir probe that are described in this section.

5.3.1 Dual-Directional Coupler

Because the Comdel CPS-3000 RF generator used in this experiment does not have a filtered RF output port, the nonlinear load presented by the antenna and plasma will introduce other frequencies in the transmission line (in particular, higher harmonics of 13.56 megahertz). Even if the CPS-3000 forward and reflected power meters are calibrated according to the operating manual, these other frequencies may induce errors in the generator RF power measurements. In order to make accurate measurements of the forward and reflected power at the dominant frequencies in the transmission line, a Werlatone -60dB dual-directional coupler (Model #C5389-32) is connected in-line at the matching network RF input port. Connecting the directional coupler at the load end of the transmission line eliminates the need to account for attenuation in the coaxial cable leading from the generator to the matching network. The directional coupler used is shown in Fig. 5.3.

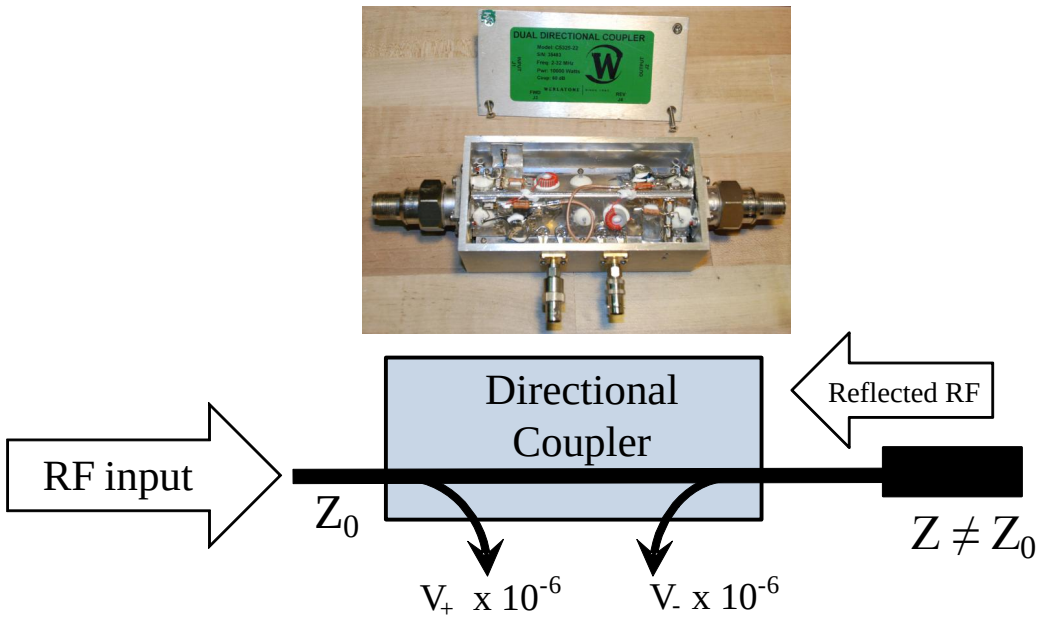

Figure 5.3: Photograph and diagram of the −60 dB dual-directional coupler.

The dual-directional coupler is a four-port device that samples the forward and reflected voltage waveforms from the main transmission line. Although the particular coupler used in this experiment is designed to work in the 2- to 32-megahertz frequency range, its response from 9 kilohertz to 100 megahertz was characterized with an Agilent E5071C network analyzer. Both the forward and reflected coupling port responses were measured to be a constant −60dB from 1 to 60 megahertz. The directivity in this frequency range was measured at a constant −30dB, showing that the forward and reflected power measurements are well-isolated from each other.

The sampled voltage waveforms are transmitted out of the LVTF to an Agilent DSOX3024A oscilloscope. The oscilloscope records and saves 2 milliseconds of the forward and reflected voltage waveforms measured at 10^9 samples per second. In order to determine the RF power in the transmission line, Parseval's theorem is applied to the power spectrum of each waveform. The power of the signals at the fundamental frequency (13.56 MHz) and the first three harmonics (27.12 MHz, 40.68 MHz, and 54.2 MHz) are summed to estimate the average RF power delivered to and reflected from the matching network. These are the dominant frequency components of the signal for every operating

point analyzed. The harmonic frequencies all fall within the frequency range at which the directional coupler was characterized. Calculations of the forward and reflected power also account for the frequency-dependent attenuation in the smaller coaxial cables used to transmit the signals from the directional coupler to the oscilloscope [123].

In order to determine the uncertainty in the RF power measurements from the directional coupler, the procedure outlined by Garvin et al. was followed [124]. The dual-directional coupler measures the forward and reflected voltage in the transmission line, $|V_+|$ and $|V_-|$, respectively. The true power delivered to the matching network, P, is given by Eq. 5.2, where Z_0 is the characteristic impedance of the RF power system (i.e. 50 Ω).

$$P = \frac{|V_+|^2 - |V_-|^2}{Z_0} \tag{5.2}$$

The power measured by the directional coupler and oscilloscope, $\bar{P}$, is given by Eq. 5.3, where $\varepsilon_{V_\pm}$ are the absolute voltage measurement uncertainties.

$$\bar{P} = \frac{\left(|V_+|^2\left(1+\varepsilon_{V_+}\right)\right)^2 - \left(|V_-|^2\left(1+\varepsilon_{V_-}\right)\right)^2}{Z_0} \tag{5.3}$$

The relative power error, ε_P, is then determined by the measurement uncertainty in $|V_+|$ and $|V_-|$, and by the reflection coefficient, $|\Gamma|$, according to Eq. 5.4. Recall from Chapter 3 that the definition of the reflection coefficient is $\Gamma = |V_-|/|V_+|$.

$$\varepsilon_P = \frac{\bar{P} - P}{P} = \frac{2\varepsilon_{V_+} + \varepsilon_{V_+}^2 - |\Gamma|^2\left(2\varepsilon_{V_-} + \varepsilon_{V_-}^2\right)}{1 - |\Gamma|^2} \tag{5.4}$$

The oscilloscope manual lists a voltage measurement uncertainty of $\pm 2.25\%$. The directional coupler response was calibrated with a network analyzer, and each voltage measurement error is conservatively rounded to $\pm 4\%$ relative uncertainty. The observed reflection coefficient, $|\Gamma|$, ranged from 0.0 to 0.4. So, the measurement uncertainty for each RF power measurement, ε_P, is between $\pm 4\%$ and $\pm 11\%$.

It is important to note that the RF power reported in this experiment is the net RF power delivered to the matching network input port. In order to quantify the exact amount of power that is delivered to the plasma, it would be necessary to thoroughly characterize the losses due to 1) ohmic dissipation in the matching network and antenna, 2) coupling to the surrounding structure, and 3) electromagnetic radiation of the RF power. An accurate model of the antenna-plasma coupling mechanism is also required to determine the true efficiency of the RF power delivery system. The assessment of the specific loss mechanisms and the antenna-plasma coupling efficiency is beyond the scope of this dissertation.

5.3.2 Thrust Stand

The performance of each thruster is measured at PEPL with an inverted-pendulum thrust stand that is run in displacement-mode. The thrust stand is based on a design from the NASA Lewis Research Center (now Glenn Research Center) [125]. When the thrust stand is run in displacement-mode, the inverted pendulum can move in a direction parallel to the thrust vector. The instantaneous pendulum position is measured by a linear variable differential transformer Linear Variable Differential Transformer (LVDT). The LVDT output is sent in real-time to a controller that actuates a non-contact, electromagnetic damper to remove oscillations in the pendulum position. A linear spring holds the pendulum in an equilibrium position, such that a steady force produced by the thruster causes a linear displacement of the pendulum. Force versus displacement calibration is performed in-situ using a set of calibration weights. The weights are connected by a string to a mounting pedestal at the top of the pendulum. Figure 5.4 shows a diagram of the thrust stand principle of operation, with the major components labeled.

The LVDT in the thrust stand at PEPL is a Schaevitz model HR-100. The HR-100 is driven by a Measurement Specialties model ATA-2001 transducer amplifier. The ATA-2001 outputs a voltage that is linearly related to the position of a magnetic core relative to the HR-100 housing. The ATA-2001 output voltage is buffered and sent to a Stanford

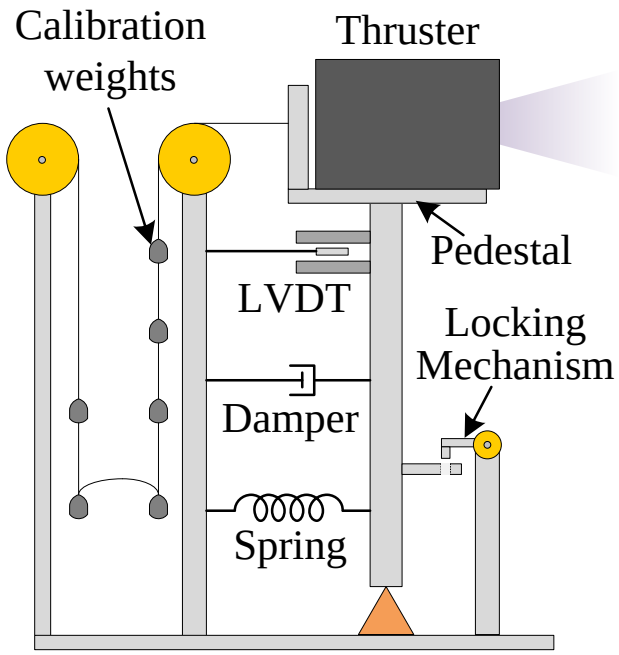

Figure 5.4: Diagram of the inverted-pendulum thrust stand. The mounting pedestal is at the top of the inverted pendulum. The spring holds the pedestal in an equilibrium position, and the LVDT measures the instantaneous position. An electro-mechanical damper reduces high-frequency oscillations in the pedestal position.

Research Systems model SIM960 analog Proportional-Integral-Derivative (PID) controller and an Opto 22 SNAP PAC data acquisition system. The SIM960 output voltage is sent to a Trust Automation model TA115 motor amplifier that drives the electromagnetic damper. A LabView Virtual Instrument communicates with the Opto 22 SNAP PAC, and records the ATA-2001 output voltage at a rate of 10 samples per second.

The thrust stand at PEPL is typically operated as a null-type thrust stand, such as that described by Xu and Walker [126]. However, preliminary experiments found that the Signal-to-Noise Ratio (SNR) and thrust measurement sensitivity were maximized when the thrust stand was operated in displacement-mode. The thermal drift was slightly greater in the displacement-mode of operation. For the RPT, the thrust stand zero-thrust position was recorded immediately before and after each operating point to ensure accurate thrust measurements. For the HHT, the thermal drift rate was highest during two-stage operation. So, the zero-thrust position was recorded before and after two-stage operating conditions.

5.3.2.1 Uncertainty Estimates

Calibrations were carried out at the beginning and end of each day of testing. During the RPT experiments, the end-of-day-calibration slope values were consistently 4–5% less than those at the beginning of the day. Observations suggested that the change in the calibration slope is due to slow thermal drift, and so individual thrust values were determined with a calibration slope that is linearly interpolated from the day's calibrations and the time of the thrust measurement. During the HHT experiments, there was less variability in the calibration slope. The absolute thrust measurement error is estimated to be $\pm 2.5\%$ for the HHT thrust measurements.

The RPT thrust is quite low. So, it was also important to quantify the resolution of the thrust stand at the low thrust levels. The noise level on the LVDT signal is approximately ± 1.5 millivolts. By averaging 25 consecutive instantaneous measurements, the uncertainty in the steady-state voltage measurement is reduced to ± 0.3 millivolts. Since the average value of the RPT thrust stand calibration slope was 200.5 millinewtons per volt, the uncertainty in each individual thrust measurement was conservatively estimated to be ± 0.1 millinewtons. Although it is anticipated that the drift in the thrust calibration slope was accounted for properly, the variation in the thrust stand calibration provides a conservative estimate of $\pm 5\%$ for the RPT absolute thrust measurement uncertainty.

5.3.2.2 EMI Mitigation

In addition to increased sensitivity and SNR, operating the thrust stand in displacement-mode allowed for a simple, in-situ procedure to check that the LVDT position signal was not influenced by electromagnetic interference EMI with the RF components or plasma. The procedure is as follows: after the LVTF is evacuated, the thrust stand pendulum is mechanically locked in place such that an applied force cannot cause a displacement. This is checked by loading all calibration weights on the thrust stand and observing no change in the LVDT position signal. The RPT or HHT is then operated normally, and any displace-

ment indicated by the LVDT signal is noted to be the result of EMI. When locked in place, the root-mean-square fluctuation level in the LVDT signal is approximately 0.4 millivolts. Thus, by averaging 10 consecutive instantaneous LVDT measurements, the observation threshold for steady-state EMI was reduced to approximately 0.13 millivolts. This lower limit on EMI detection is more than a factor of 2 lower than the above stated thrust stand measurement resolution for the RPT. So, the thrust measurement uncertainty for small thrust values is still estimated at $\pm 5\%$ due to the variation in calibration slope.

Although the initial setup was severely affected by EMI during operation with RF plasma, the implementation of multiple mitigation strategies eliminated these effects. There is no analytical solution to removing EMI from an electrical setup. The strongest EMI reduction was observed when split-core ferrite beads were applied to all wires leading to the thrust stand. It is important to note that the proper choice of a ferrite material that maximizes the impedance at the RF driving frequency was critical to the success of this strategy. The datasheets for the ferrite beads implemented at PEPL are given in Appendix B. For each wire, if there was enough slack, then two or three loops of the wire were wrapped around the ferrite bead. This further increased the impedance at the RF driving frequency.

After the EMI was eliminated, the pendulum was released so that the thrust stand returned to the displacement-mode configuration. A calibration was then performed to confirm that the thrust stand is operating normally, and then thrust measurements were taken. Every operating point presented in this work was tested first with the thrust stand in the EMI-checking configuration. After the initial EMI check and prior to venting the LVTF, the full experiment was completed. After all thrust measurements are taken, another full EMI check was performed for all operating points according to the above procedure.

A check was also performed to verify that the thrust stand calibration slope was not affected by EMI. The procedure for checking the calibration slope is as follows: while the RPT or HHT is operating with RF, one or two calibration weights are loaded on the pendulum to increase the force acting on the thrust stand spring. The masses are then unloaded

and the RF power is turned off. Then, a regular thrust stand calibration is performed. The change in the LVDT output caused by the additional force of the calibration weights is then checked against the predicted force according to the normal calibration. This check showed that any change in the calibration slope due to EMI was smaller than the thrust measurement resolution.

5.3.3 Faraday Probe

A nude Faraday probe is used to measure the ion current density in the thruster exhaust plume. The Faraday probe is mounted to a rotation stage such that it can move in an arc about the centerline of the thruster exit plane. To take data, the collector(s) and guard ring are biased into ion saturation. The current drawn by the collector is recorded as the probe position is swept between -90 and 90 degrees, where 0 degrees is on thruster centerline.

The total ion beam current, I_{beam}, may be determined by assuming that the exhaust plume is axisymmetric. The Faraday probe collected current, $I_c(\theta)$, is then integrated according to Eq. 5.5, where r is the distance from the Faraday probe collector to the thruster exit plane. For the HHT, the effective collector area, $A_{c,eff}$, includes all correction factors described by Brown [77].

$$I_{beam} = 2\pi r^2 \int_0^{\pi/2} \frac{I_c(\theta)}{A_{c,eff}} \sin\theta \, d\theta \tag{5.5}$$

Using the same Faraday probe data, the axial component of the ion beam current, I_{axial}, is calculated from Eq. 5.6.

$$I_{axial} = 2\pi r^2 \int_0^{\pi/2} \frac{I_c(\theta)}{A_{c,eff}} \sin\theta \cos\theta \, d\theta \tag{5.6}$$

The Faraday probe used for the HHT is described in detail by Liang and Gallimore [127], and is modeled after the nested Faraday probe described by Brown and Gal-

limore [128]. The Faraday probe used to measure the plasma in the RPT exhaust plume has been used in previous studies of Hall thrusters, for example by Hofer [114]. A diagram of the Faraday probe used to measure the RPT plume properties is shown in Fig. 5.5.

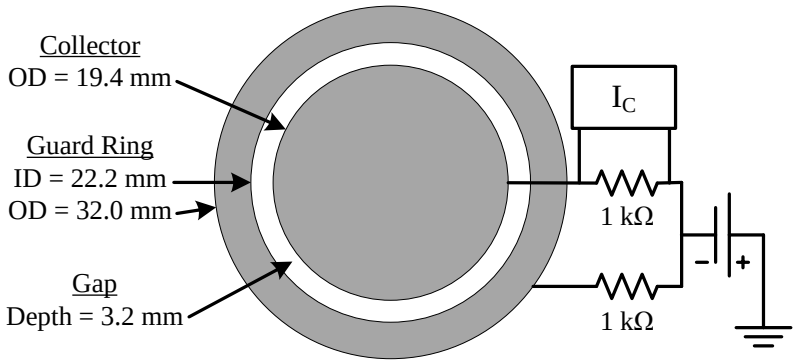

Figure 5.5: Schematic of the Faraday probe used for RPT measurements.

For the RPT, the guard ring and collector are both biased below -58 volts with respect to facility ground into ion saturation. The current drawn by the collector is recorded via the voltage drop across a 1 kilohm resistor as the Faraday probe collection surface is swept from -90 to 90 degrees at a constant distance of 96 ± 0.5 centimeters from the center of the RPT exit plane. The Faraday probe angular alignment was checked before and after the experiment with a laser bore sight inserted into the RPT gas inlet, and the alignment uncertainty is conservatively estimated to be ± 0.6 degrees.

For analysis of the RPT Faraday probe data, it is assumed that the RPT is a point source of plasma, and the effective collector area is taken to be the geometric area of the collector face. The total ion beam current is calculated from Eq. 5.5, and the axial beam current is calculated from Eq. 5.6. The RPT effective exhaust divergence half-angle, θ_{div}, is then calculated according to Eq. 5.7.

$$\theta_{div} = \cos^{-1}\left(\frac{I_{axial}}{I_{beam}}\right) \tag{5.7}$$

Following the analysis by Brown [77], and because Faraday probe data for each thruster operating condtion are taken at one downstream distance and one facility backpressure,

the uncertainty in the total and axial ion beam current measurements are initially taken to be $\pm 6\%$ and $\pm 10\%$, respectively. This translates to an uncertainty of approximately ± 9 degrees in the measured effective exhaust divergence half-angles.

5.3.4 Retarding Potential Analyzer

The Ion Voltage Distribution (IVD) is measured with a Retarding Potential Analyzer (RPA) at PEPL. This particular RPA has been previously used to measure plasma properties in a helicon plasma source [129], as well as in Hall thruster plumes [114, 117]. The RPA at PEPL is based on the multi-gridded energy analyzer described by Hutchinson [130]. It consists of three stainless steel grids and a collector contained in a stainless steel housing, as shown in Fig. 5.6. The grids and collector are isolated from each other and the housing by ceramic washers that also serve to set the spacing between the grids.

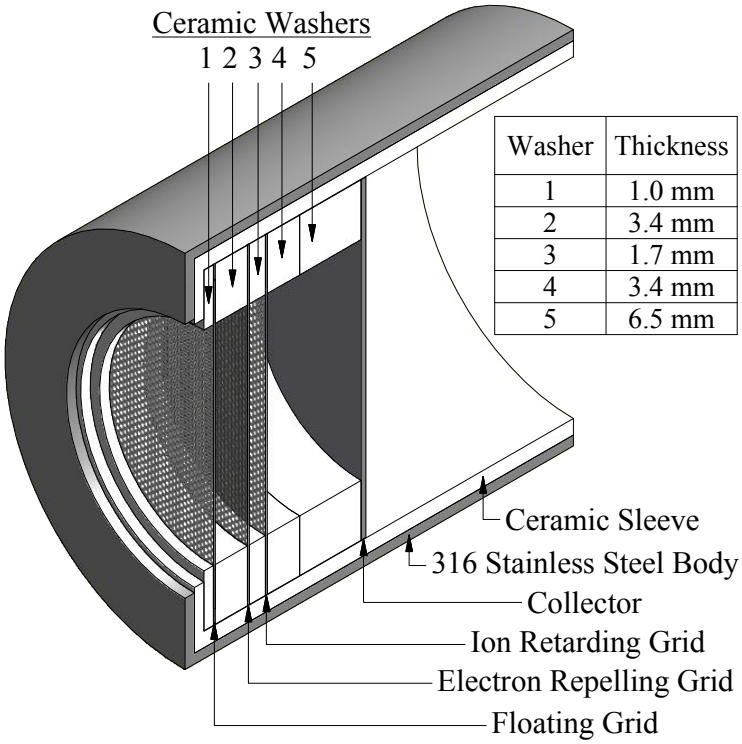

Figure 5.6: Cross-section of the RPA.

A schematic of the RPA is shown in Fig. 5.7. The electron repelling grid is biased with a Kikusui PAD 55-6L power supply. The ion retarding grid is is powered with a Keithley 2410 SourceMeter. A Keithley 6485 Picoammeter measures the current to the collector.

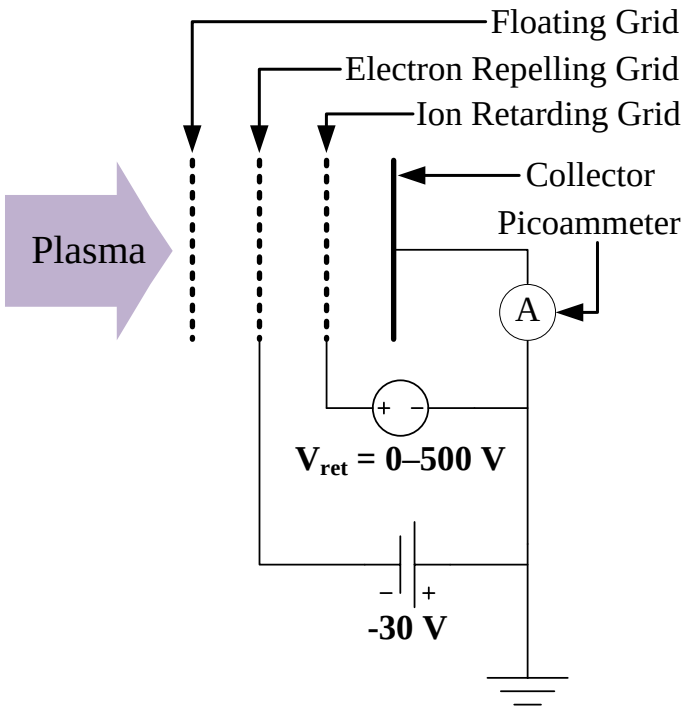

Figure 5.7: Electrical schematic of the RPA.

To collect measurements of the IVD, the floating grid first accepts charged particles from the plasma in a minimally disruptive manner. Then, the electron repelling grid is biased to a constant -30-volt potential with respect to facility ground to prevent the incident electrons from reaching the collector. The ion retarding grid is then swept from 0 to 500 volts above ground to progressively filter out higher energy ions. The current to the collector is recorded at each ion retarding voltage. The IVD, $f(V)$, is directly proportional to the first derivative of the measured current-voltage characteristic, shown by Eq. 5.8 [129], where I_c is the collected ion current, V_{ret} is the ion retarding grid bias voltage, n_i is the ion density, m_i is the ion mass, q is the ion charge, and $A_{c,eff}$ is the effective RPA collector area.

$$\frac{dI_c}{dV_{ret}} = -\left(\frac{n_i}{m_i}\right) q^2 f(V) A_{c,eff} \tag{5.8}$$

The maximum value of the first derivative is called the *most probable potential*, V_{mp}, as shown in Fig. 5.8. This voltage is related to the most probable total energy of the ions collected by the RPA.

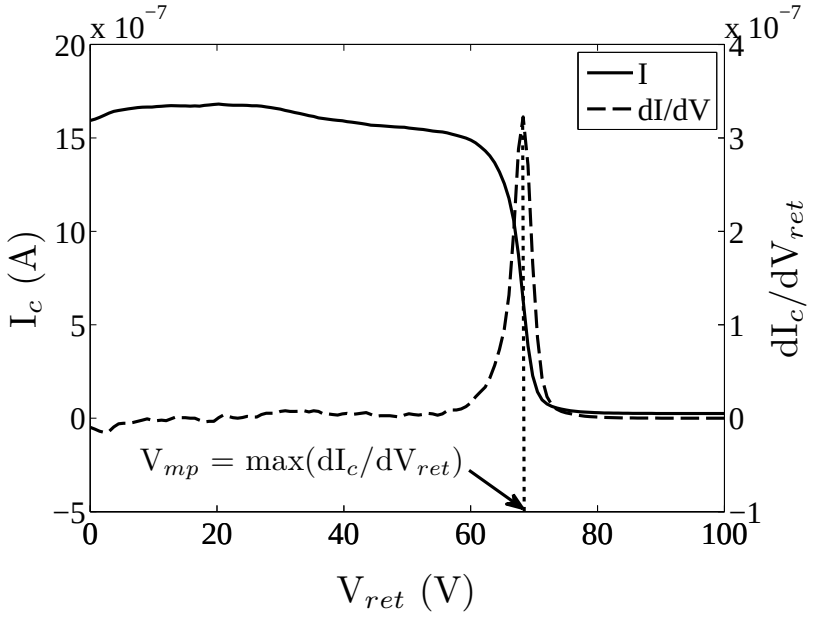

Figure 5.8: Typical data from the RPA. Data shown are from the RPT operating condition at 2.4 mg/s, 550 G, and 1080 W.

Previous studies using this particular RPA in Hall thruster plumes have estimated the uncertainty in the most probable potential measurement to be ± 10 V [77, 114]. The uncertainty can be attributed to broadening of the peak due to the RPA's large acceptance half-angle (approximately 45°), and the effects of smoothing and numerical differentiation of the raw RPA data. The Half-Width at Half-Maximum (HWHM) of the peak in the first derivative of the RPA current-voltage characteristic also gives a conservative measure of the uncertainty. The results reported in this dissertation use the HWHM to represent the uncertainty in the most-probable potential measurement of the RPA.

The RPA is mounted to a linear translation stage with a Langmuir probe so that both the RPA and Langmuir probe data can be taken at the same position. For the RPT experiments, the RPA floating grid is 1.24 meters downstream of the RPT exit plane. For the HHT experiments, the RPA floating grid is about 6 meters downstream of the HHT exit plane.

5.3.5 Langmuir Probe

An ESP*ION* Langmuir probe system manufactured by Hiden Analytical is used to determine the plasma potential in the RPT thruster exhaust plume. A cylindrical, uncompensated Langmuir probe is used for the HHT experiments. The ESP*ION* probe has been used in previous experiments with RF plasmas at PEPL, for example by Lemmer [129]. Both Langmuir probes are mounted to the RPA translation stage so that the IVD and plasma potential can be collected in the same location, on the centerline of the thruster.

For each operating condition, at least five individual current-voltage characteristics are averaged prior to analysis. The derivative method, shown in Fig. 5.9, is used to determining the plasma potential from a Langmuir probe characteristic. This method was found by Shastry to have the closest agreement with emissive probe measurements. Using the derivative method, the estimated uncertainty in the plasma potential is $\pm 20\%$ [131].

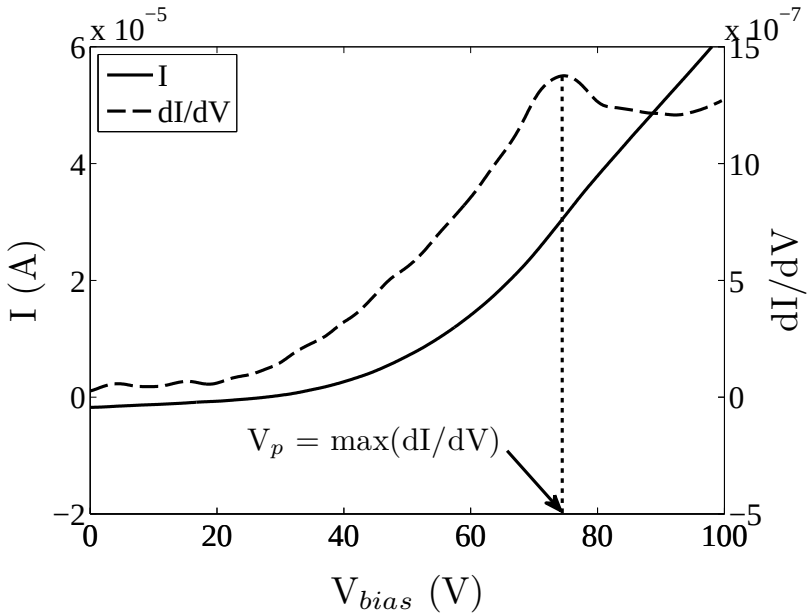

Figure 5.9: Typical data from the Langmuir probe. Data shown are from the RPT operating condition at 2.4 mg/s, 550 G, and 1080 W.

The ESP*ION* is an RF-compensated Langmuir probe driven by the HAL IV ESP Controller. A computer connected to the controller runs the program **ESPsoft** to bias the probe tip from -100 to 100 volts and simultaneously record the probe current. The ESP*ION*

probe tip is a tungsten wire that is 0.15 millimeters in diameter by 10 millimeters long.

The Langmuir probe used to measure the plasma potential in the HHT exhaust plume is a 0.25-millimeter-diameter, 5.7-millimeter-long tungsten wire. The probe holder is a 0.15 cm diameter alumina tube. The probe tip is powered by a 1-hertz -50 to 150-volt triangle wave by a Kepco model BOP 500M bipolar amplifier. The amplifier is driven by an Agilent 33220A Arbitrary Waveform Generator. The bias voltage and collected current are simultaneously recorded by a data acquisition system.

5.4 Thruster Setup

Both the RPT and HHT were electrically isolated from the vacuum chamber and the thrust stand by placing a 6.35-millimeter-thick mica plate between the thruster mounting plate and the pedestal of the thrust stand. In addition, the propellant flows through an insulating torturous path immediately upstream of the thruster gas inlet connection. This tortuous path prevents an upstream connection from the plasma to ground. The matching network is mounted on the thrust stand pedestal, and held in place by an aluminum structure. The antenna leads are connected directly to the matching network output leads. The antenna connection is covered with Kapton tape and surrounded by copper mesh to reduce the probability of locally ionizing the background neutral gas. Details unique to the individual thruster setups are described further in this section.

5.4.1 RPT

For the RPT thrust measurements, ultra high purity (99.999% pure) argon is used as the propellant. The gas flow rate during both nitrogen and argon operation is regulated by an Alicat MC-500SCCM-D mass flow controller, which has an accuracy of $\pm 0.8\%$ of the setting plus $\pm 0.2\%$ of full scale. Each RPT solenoid coil is independently powered by a Lambda EMS-series power supply, and the current of each solenoid is measured across

a Deltec MKA-25-100 current shunt. An isolated Opto 22 SNAP PAC data acquisition system records the solenoid magnet currents and the forward and reflected power output by the CPS-3000 concurrently with LVDT data from the thrust stand. The magnetic field was non-uniform during RPT operation, and the maximum magnetic field was approximately 810 Gauss, as shown in Fig. 5.10. In all further discussion of the RPT results, the magnetic field of each RPT operating condition is labeled by the average centerline axial magnetic field in the magnet assembly.

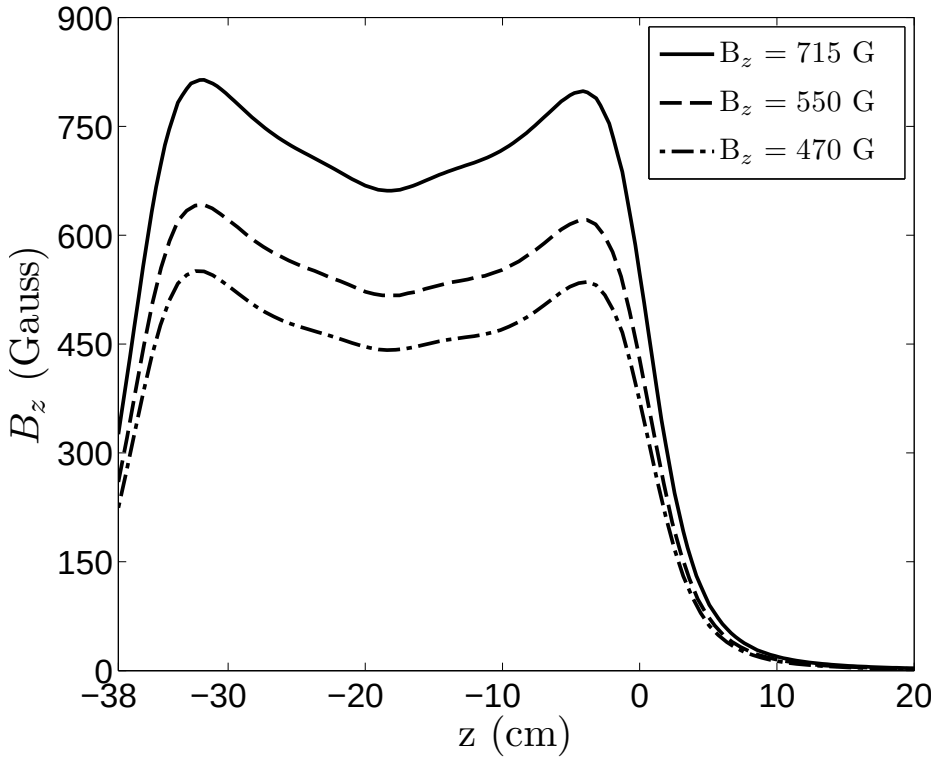

Figure 5.10: RPT centerline axial magnetic fields, simulated with measured solenoid currents. The exit plane is at z = 0 centimeters, and the legend refers to the average field in the RPT.

5.4.2 HHT

The HHT used an externally-mounted thermionic cathode with a lanthanum hexaboride (LaB_6) insert to produce electrons for the Hall acceleration stage. Research-grade xenon

(99.999% purity) was used for the cathode flow for all HHT operating conditions, and the cathode flow was regulated by an MKS model 1179A mass flow controller. This mass flow controller has a specified accuracy of $\pm 1\%$ of full scale. The cathode is mechanically connected to the HHT on the thrust stand. Thus, the HHT thrust measurements include any force that is produced by the cathode. During operation with xenon, an MKS model 1159B mass flow controller regulated the flow of research-grade xenon to the HHT anode. For the HHT argon and nitrogen operating conditions, an Alicat model MC-500SCCM-D mass flow controller was used to regulate and measure the anode mass flow rate. Note that the HHT was operated for a length of time prior to taking any performance or probe measurements. This was done to bake out any condensible materials from the thruster.

CHAPTER 6

Results

The RPT and HHT were both operated successfully on the thrust stand at PEPL. Simultaneous performance and plasma plume measurements were collected to investigate the loss mechanisms. This represents the first time such measurements have been made with a matching network located inside the vacuum chamber on the thrust stand. The RPT operated with argon, nitrogen, and ambient air, and the HHT operated with xenon, argon, and nitrogen. The first section of this chapter reports the RPT performance and probe measurements while operating with argon, followed by the results of the RPT operating with nitrogen and air. The second section then presents the single- and two-stage performance measurements of the HHT operating with xenon, argon, and nitrogen propellant.

6.1 RPT Results

The corrected LVTF operating pressure during RPT experiments remained below 4.7×10^{-6} Torr. Despite this low pressure, and the large bore of the quartz tube, the RPT operated with a bright blue core at nearly all argon operating conditions analyzed. This provided strong visible evidence of significantly improved power coupling to the plasma over previous RPT experiments in the LVTF, during which the matching network remained outside the vacuum chamber.

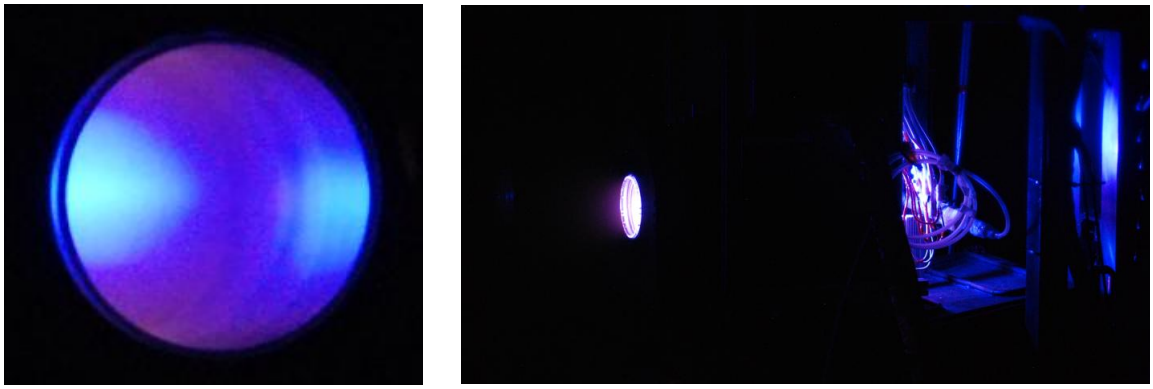

Figure 6.1: Two views of the RPT argon blue core plasma during operation in LVTF. The end-on view of the exhaust (left) shows the blue core. Light from the blue core shines through the inlet side of the RPT quartz tube and reflects off the thrust stand structure (right).

6.1.1 RF Power Measurements

As previously discussed, the antenna-and-plasma load may be nonlinear. This can cause some of the RF power to be reflected from the load at frequencies that are not 13.56 megahertz (the driving frequency). This arises from the natural behavior of the plasma, and cannot be avoided. The CPS-3000 does not have a filtered output and is not calibrated for frequencies other than 13.56 megahertz. So, the effect of other frequencies on the forward and reflected power measurements output by the CPS-3000 was unknown a priori. The forward and reflected powers determined from the directional coupler during RPT operation with argon are plotted versus the RF power readings output from the CPS-3000 in Fig. 6.2.

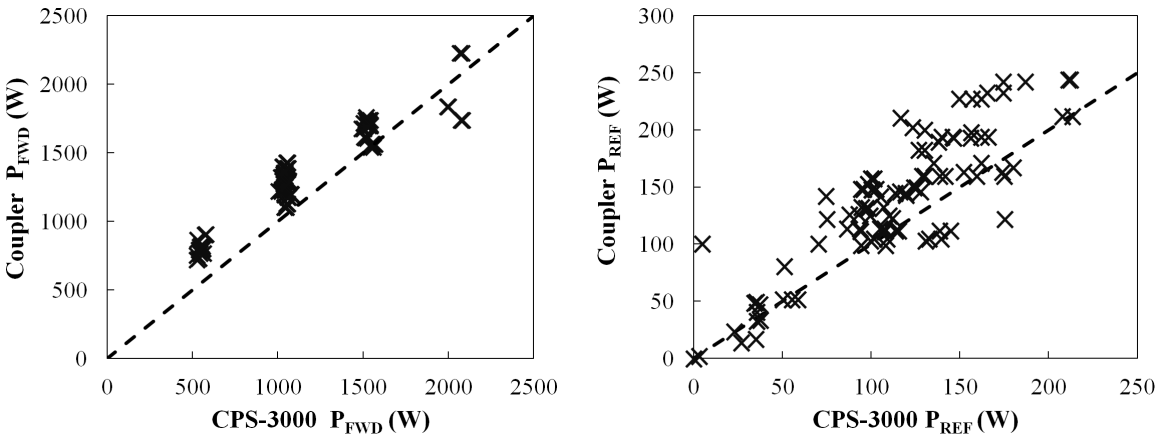

Figure 6.2: RF power measurements from the CPS-3000 versus the dual-directional coupler for forward (left) and reflected (right) RF power. CPS-3000 data are from the calibrated analog 0–10 V outputs. Points lie on the dotted line when both measurements agree.

The attenuation in the coaxial cable is accounted for so that the points in Fig. 6.2 represent the power at the CPS-3000 output port [123]. The magnitude of the reflection coefficient, $|\Gamma|$, never exceeded 0.41 for all RPT operating points analyzed, yet the CPS-3000 power meters typically indicated lower forward and reflected powers than those determined by analysis of the corresponding directional coupler signals. The discrepancy between the two measurements may be caused by a non-uniform frequency response or poor directivity in the CPS-3000 measurement circuit.

6.1.2 Argon Performance

The performance of the RPT due to cold gas expansion of argon in the quartz tube is measured first. The cold gas thrust is measured with zero input RF power, and the specific impulse is calculated. The results are plotted in Fig. 6.3. The theoretical cold gas thrust can be estimated by assuming the quartz tube as an ideal nozzle, and using supersonic isentropic flow equations, given by Anderson [132]. The resulting thrust and specific impulse using the real RPT geometry and argon mass flow rates are shown by the dotted lines in Fig. 6.3. Since the RPT quartz tube has discrete changes in area, it was anticipated that cold gas performance would be lower than that for an isentropic nozzle. This agrees with the results shown in Fig. 6.3, within an order of magnitude.

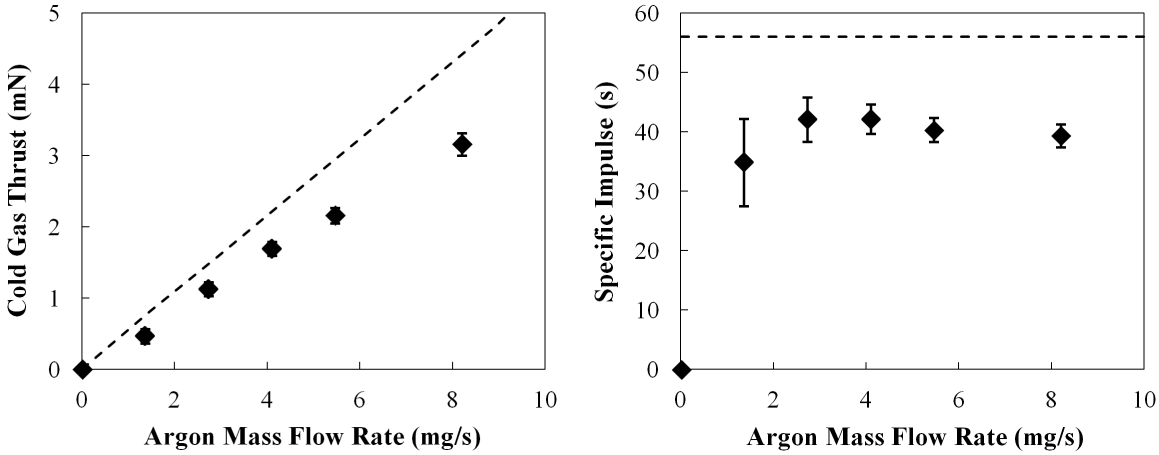

Figure 6.3: Measured cold gas thrust (left) and specific impulse (right) for argon flow in the RPT. Dotted lines represent theoretical performance from isentropic flow theory.

The thrust due to RF power and cold gas flow are separately measured. The measurements are summed to determine the total thrust at a given operating condition. The RPT thrust measurements with RF power applied were taken at argon flow rates from 2.2 to 7.0 milligrams per second. This corresponded to an LVTF operating pressure range of 1.5 to 4.7 $\times$ 10^{-6} Torr. All measurements of total thrust for the RPT operating with argon are plotted in Fig. 6.4.

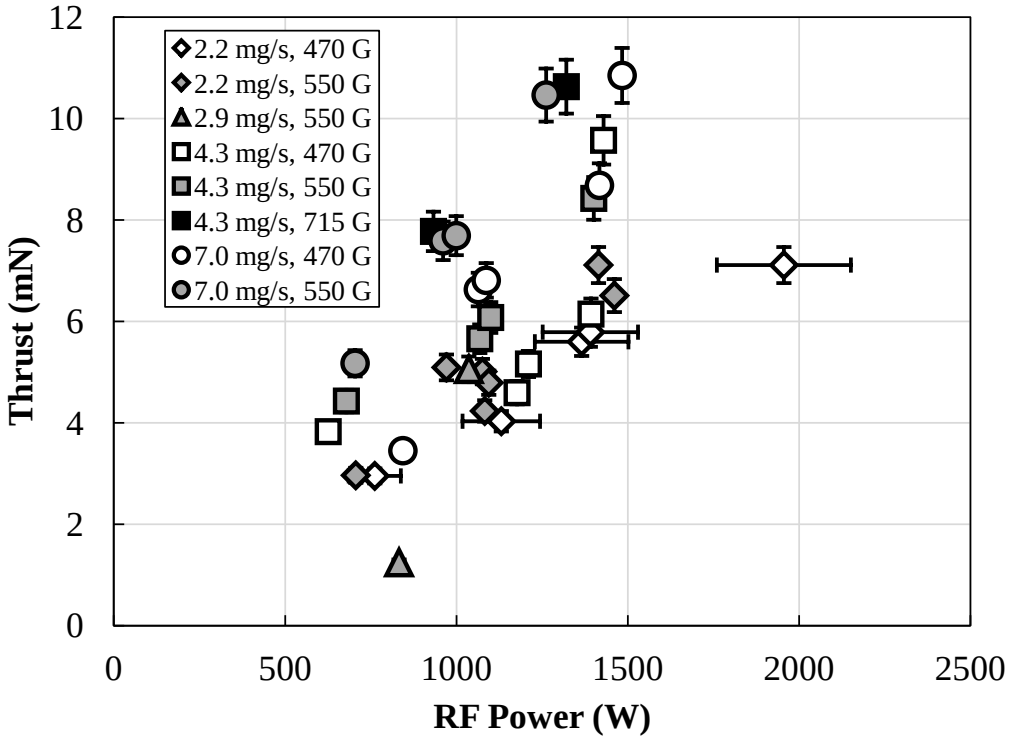

Figure 6.4: RPT total thrust versus net RF power. To reduce clutter, horizontal error bars are plotted only for the first data series, but they are representative for the entire dataset.

Total thrust increases both with increasing RF power and increasing magnetic field strength. Total thrust also increases with increasing flow rate, but it is important to note that the cold gas thrust contributes 2.7 millinewtons to the total force at the 7.0-milligram per second operating conditions. The lowest thrust measured was 1.2 millinewtons at the 2.9-milligram per second, 550-gauss operating condition at 830 watts. The RPT plasma for this data point did not exhibit a strong blue core. The cold gas thrust at 2.9 milligrams per second of argon is 1.1 millinewtons. Thus, the application of RF power did not signifi-

cantly contribute to the total thrust. Another interesting result is that the total thrust is equal for the 4.3-milligram per second, 715-gauss operating conditions and the 7.0-milligram per second, 550-gauss operating conditions that are at the same RF power. The cold gas thrust is approximately 1 millinewton less at 4.3-milligram per second flow rates, and this difference is offset by the increased magnetic field strength. The maximum total thrust measured is 10.8 millinewtons at a specific impulse of 158 seconds and RF thrust efficiency of 0.5%.

The RPT specific impulse also increases with increasing RF power, and tends to increase with increasing magnetic field strength. The RPT specific impulse is calculated from the total thrust and propellant mass flow rate, and the results shown in Fig. 6.5.

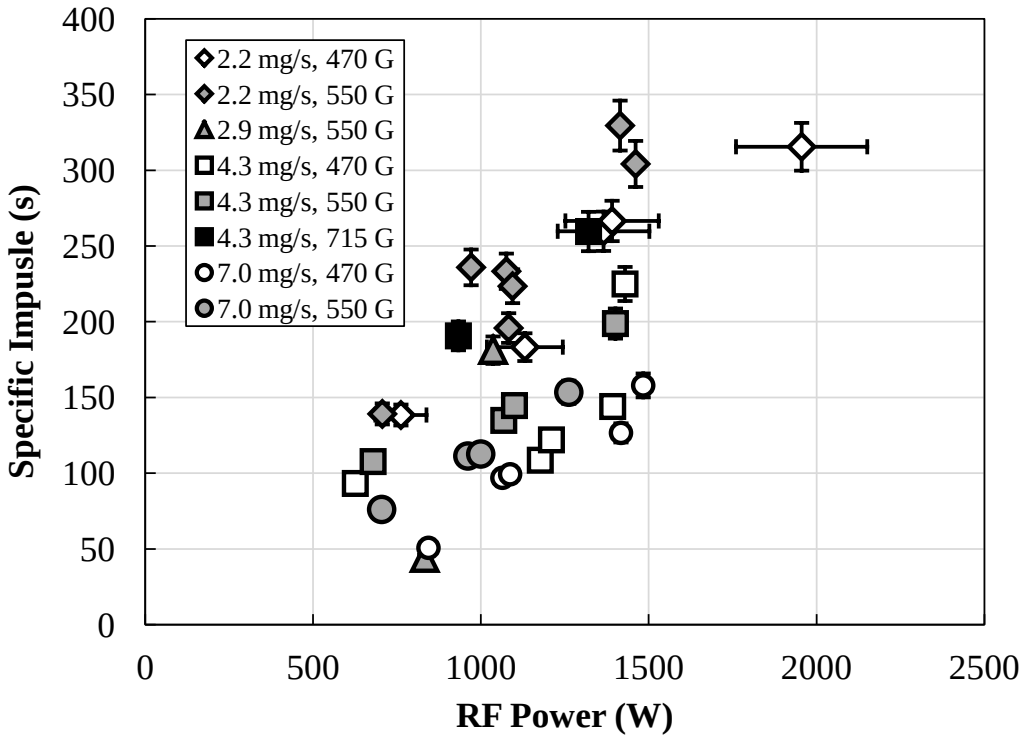

Figure 6.5: RPT specific impulse versus net RF power. Specific impulse is calculated using the sum of the cold gas thrust and the thrust due to RF. Horizontal error bars shown are representative for the entire dataset for equivalent RF power levels.

The RPT specific impulse decreases with increasing flow rate because the measured increase in thrust is much less than the increase in mass flow rate. The specific impulse at 4.3-milligrams per second and 715-gauss is approximately equal to the specific impulse at 2.2-milligram per second and 470-gauss for a given RF power. The maximum specific

impulse measured is 330 seconds at a total thrust of 7.1 millinewtons and an RF thrust efficiency of 0.7%.

The RF thrust efficiency of the RPT, η_{RF}, is calculated from the net RF power delivered to the matching network and the thrust due to RF power. The RF thrust efficiency of the RPT operating with argon is shown in Fig. 6.6. Note that the definition of RF thrust efficiency reported here includes the matching network and antenna coupling efficiency, but not the DC power supplied to the RPT magnets.

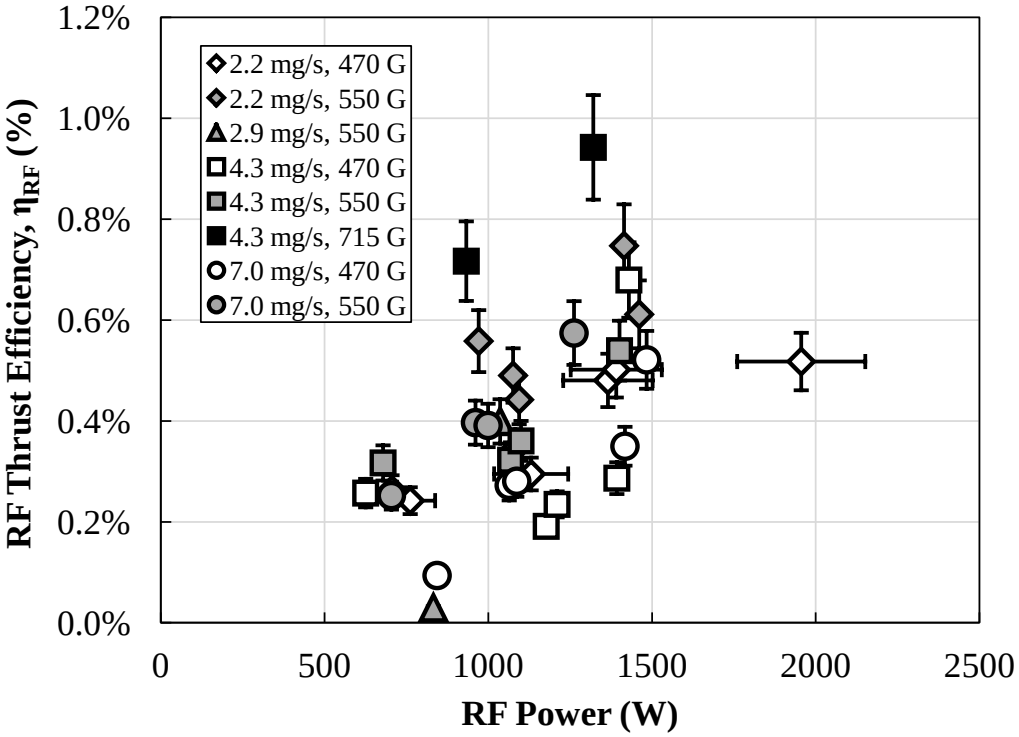

Figure 6.6: RPT RF thrust efficiency versus net RF power. RF thrust efficiency is calculated using the RF power delivered to the matching network. This definition of efficiency does not include the DC power to the magnets.

The RF thrust efficiency of the RPT increases with increasing RF power and with increasing magnetic field strength. Efficiency also increases with decreasing flow rate, but remains below 1% for all operating conditions. Note that the uncertainty in the RF power measurement increases the uncertainty in the RF thrust efficiency to $\pm 11\%$ of the value. The maximum RF thrust efficiency measured is 0.9% at a total thrust of 10.6 millinewtons and a specific impulse of 260 seconds.

6.1.3 Argon Probe Measurements

The RPA and Langmuir probe are mounted to a motion table so that the plasma potential and the most probable ion voltage can be measured at the same location. The Langmuir probe tip is aligned such that the length of the probe is parallel to the RPT axis. The electron temperature and plasma floating voltage measured by the Langmuir probe are plotted in Fig. 6.7. Electron temperature is determined by the inverse slope of the natural logarithm of the electron current in the vicinity of the floating voltage [129].

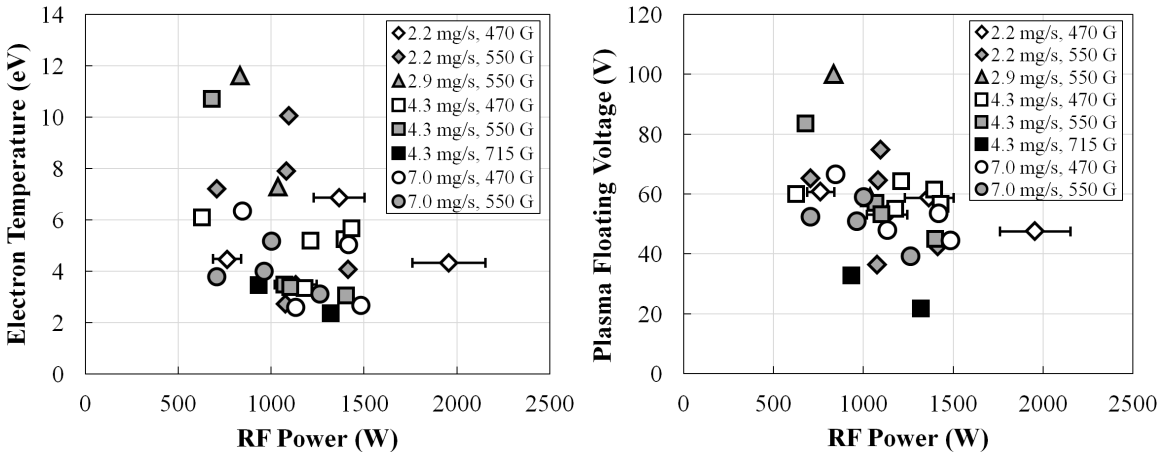

Figure 6.7: RPT plume electron temperature (left) and floating voltage (right) measured by a Hiden Langmuir probe system. Helicons typically produce 3 to 5 eV electron temperatures.

Typical helicon sources produce plasma at 3 to 5 eV electron temperatures, and temperatures in the 10 to 15 eV range may be indicative of a capacitively coupled plasma [88]. The absolute uncertainty in the electron temperature is estimated at $\pm 20\%$ [130], but the relative error between measurements in the same setup is lower [133]. Oscillations in the floating potential were not observed, and since multiple current-voltage characteristics were averaged, the uncertainty in the floating potential measurement is conservatively estimated to be ± 2 volts.

The plasma density is determined using orbit-motion limited theory in the ion saturation part of the current-voltage characteristic [129, 134]. The plasma potential is determined as the peak in the first derivative of the current-voltage characteristic. The plasma potential and density measured in the RPT plume by the Langmuir probe are plotted in Fig. 6.8.

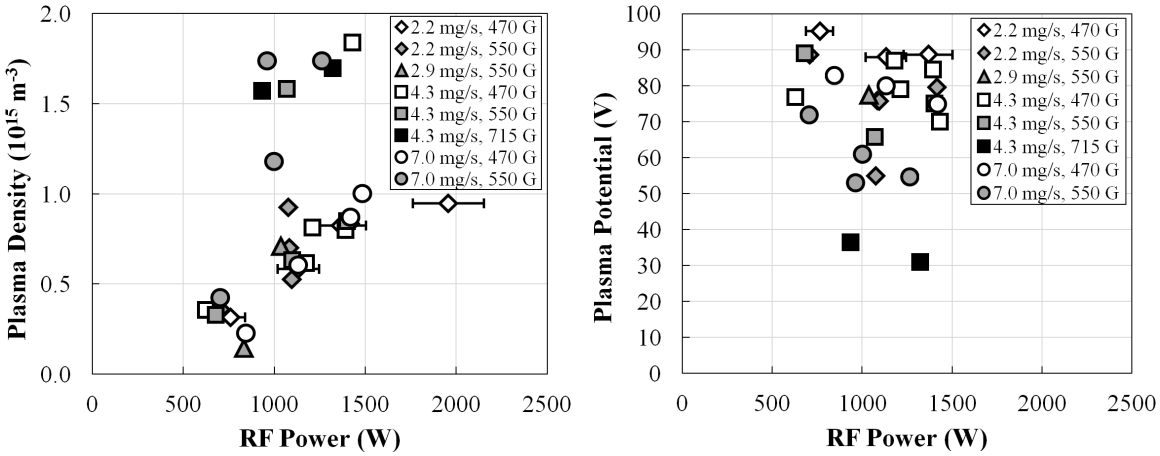

Figure 6.8: RPT plume density (left) and plasma potential (right) measured by a Hiden Langmuir probe system. Plasma potential is determined by the derivative method.

The plasma density mainly increases with increasing RF power, showing a nonlinear increase for some of the flow rate and magnetic field combinations. The plasma potential does not show any clear trends with RF power or flow rate, but the plasma potential is lower at the operating conditions with higher plasma density.

RPA measurements of the RPT operating on argon exhibited a single peak in the first derivative of the current-voltage characteristic. Other experiments have observed IVDs with two peaks [70, 71, 75]. Secondary peaks in this experiment were two orders of magnitude smaller than the dominant peak at higher voltage. So, the RPA was only used to determine the most probable voltage of the RPT exhaust ions. The results are shown in Fig. 6.9.

The most probable exhaust ion voltage decreases both with increasing flow rate and with increasing magnetic field strength. Note that the vertical error bars in Fig. 6.9 represent the half-width at half-maximum in the IVD peak. Thus, the distribution of ions about the most probable voltage is on the order of a few volts.

Faraday probe current density data was only taken at four RPT operating conditions. These Faraday probe current density characteristics were integrated to determine the total ion beam currents and the axial component of the ion beam currents in the positive hemisphere. The results showed that the four points analyzed all had an effective divergence half-angle of approximately 48 degrees. Further analyses of the RPT Faraday probe data

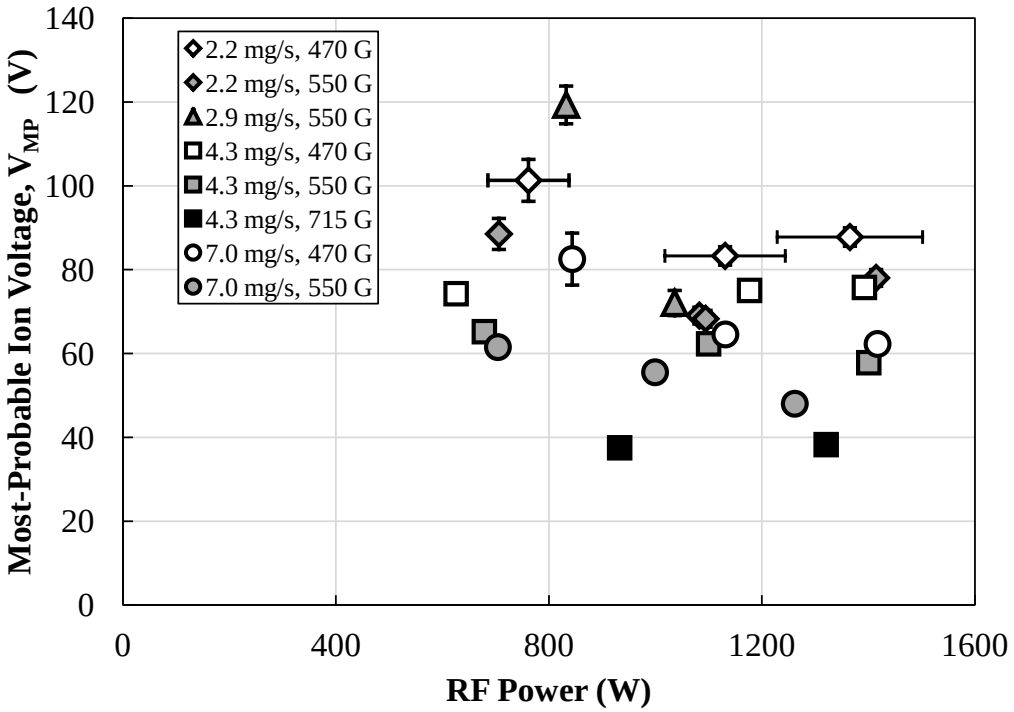

Figure 6.9: Most probable potential from RPA versus RF power. Note that the plasma potential must be subtracted to determine the most probable ion kinetic energy.

are presented in the following chapter.

6.1.4 RPT Operating on Nitrogen & Air

The helicon wave dispersion relation depends on the number density of the plasma, not the mass flow rate. So, the number flow rate was held constant for the different species. The mass flow rates at 4.3- and 7.0-milligrams per second of argon corresponded to approximately 150- and 250-standard cubic centimeters per minute, respectively. Figure 6.10 shows two photographs of the RPT operating with nitrogen propellant. Although there was visible evidence that the RPT coupling to nitrogen and air propellant was strong, no additional thrust was measured when applying RF power.

Due to the low thrust measured, relatively few nitrogen or air operating conditions were investigated. The Faraday probe data qualitatively gave lower ion current densities by about a factor of ten compared to the argon operating conditions. This suggested that

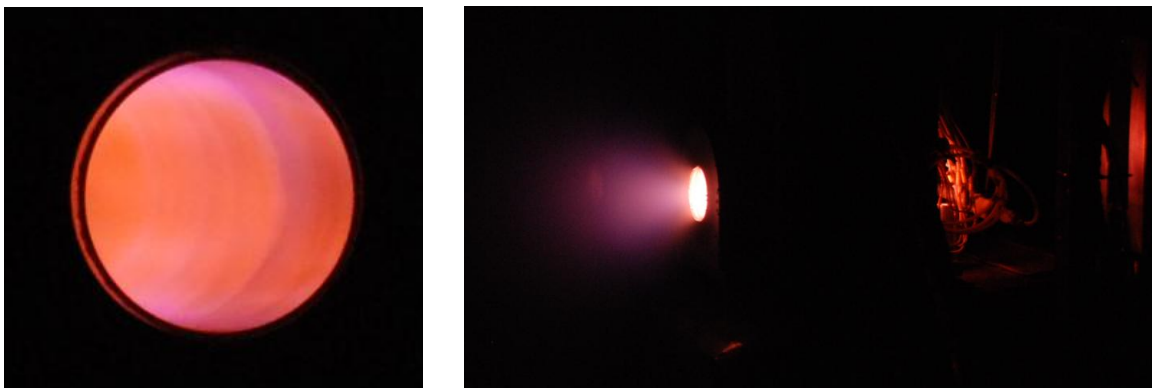

Figure 6.10: Photographs of RPT operating with nitrogen, with end-on view on left. No blue core was observed, perhaps due to the fact that nitrogen ions strongly emit in the ultraviolet.

the low thrust may be due to lower ion production by the RPT operating with nitrogen. The Langmuir probe did not reach electron saturation at the Hiden controller upper limit on bias voltage of 100 volts. Figure 6.11 shows the RPA data from the three nitrogen operating conditions where data were taken.

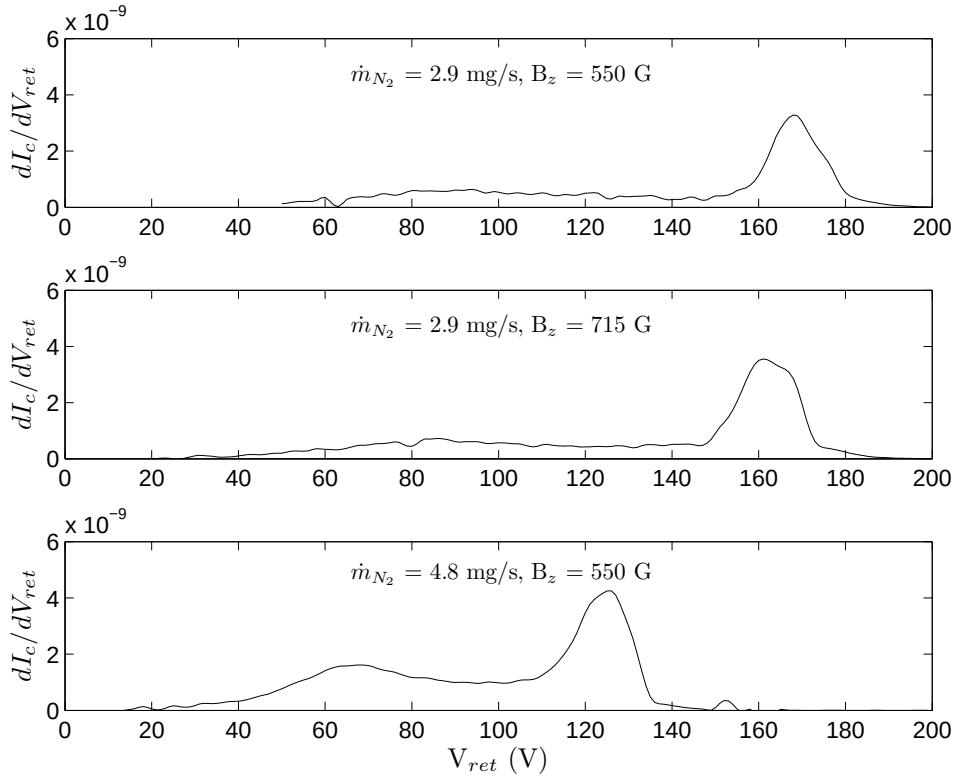

Figure 6.11: RPA data for the RPT operating on nitrogen at about 1000 watts. Plasma floating voltages were measured at 50 $\pm$ 5 volts. No plasma potential measurement is available.

The RPT operating conditions with air yielded similar results as those with nitrogen, with the flow rate having the strongest effect on the measured most probable voltage. The derivatives of the RPA data during RPT air operating conditions are shown in Fig. 6.12.

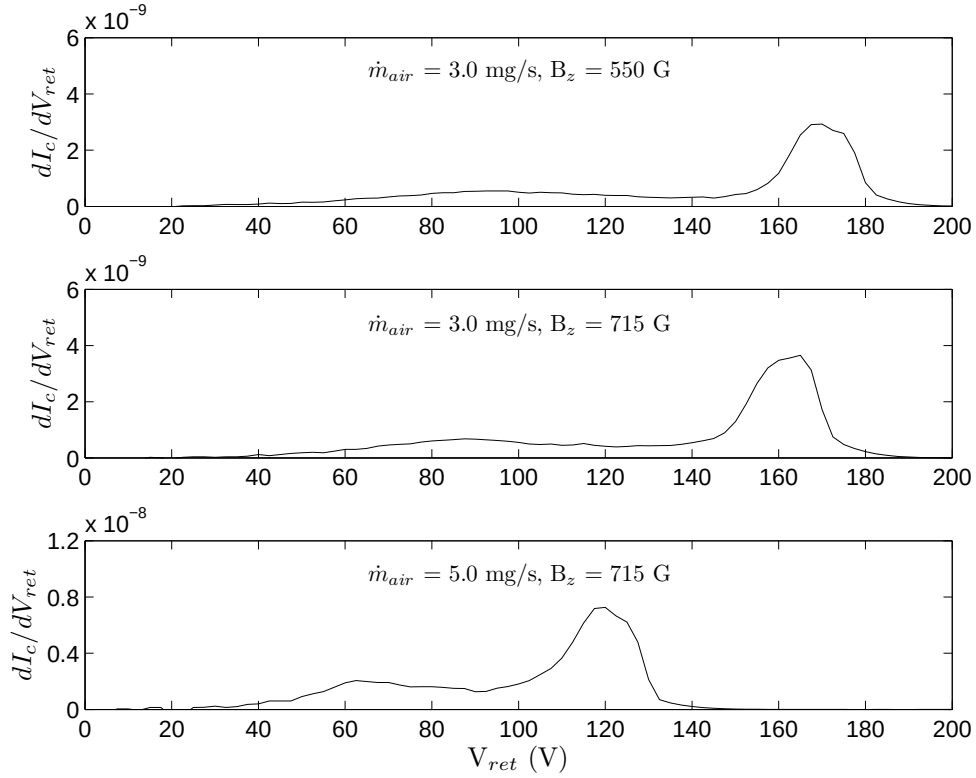

Figure 6.12: RPA data for the RPT operating on air at about 1000 watts. Note that the vertical scale in the bottom subplot is twice as large as that in the other RPA data plots.

For the RPT operating on air, the plasma floating potential measured by the ESP*ION* Langmuir probe was approximately 58 ± 5 volts for the 2.9-milligram per second operating conditions. The floating potential for the 4.8-milligram per second operating condition was measured to be 43 volts.

6.2 HHT Results

The performance of the HHT was measured on xenon, argon, and nitrogen propellants with and without the RF stage operating. For the argon and nitrogen operating conditions, the external hollow cathode was operated with research-grade xenon (99.999% purity). The HHT total flow rate when operating with xenon was in the range from 10.7 to 26.7 milligrams per second, corresponding to LVTF corrected pressures of about 4.6×10^{-6} to 1.5×10^{-5} Torr. During argon and nitrogen operation, the corrected LVTF pressure was measured at 3.9×10^{-6} Torr and 3.6×10^{-6} Torr, respectively. Figure 6.13 shows the HHT operating on each propellant.

The HHT was constructed to investigate whether an RF ionization stage could increase the efficiency of a Hall thruster operating in a low-specific impulse regime. So, the HHT operating conditions mainly focused on low discharge voltage operation with xenon propellant. Table 6.1 summarizes all the HHT operating conditions that were tested. The "Plume Measurements" column in Table 6.1 indicates where probe diagnostics were used in the HHT plume during single-stage operation and/or while the RF stage was operating.

Table 6.1: Summary of HHT operating conditions and measurements.

Propellant	Anode Flow Rate (mg/s)	Discharge Voltage (V)	RF Power Range (W)	Cathode Flow Fraction	Plume Measurements[a]
xenon	10.0	200	0 – 1036	7.1%	1s
xenon	14.9	100	0 – 1028	5.0%	1s
xenon	14.9	150	0 – 1041	5.0%	1s
xenon	14.9	200	0 – 1032	5.0%	1s
xenon	20.0	100	0 – 994	5.0%	1s & 2s
xenon	20.0	150	0 – 1205	5.0%	1s & 2s
xenon	20.0	200	0 – 986	5.0%	1s
xenon	25.0	200	0 – 613	7.0%	-
argon	5.48	300	0 – 270	16.8%[b]	1s & 2s
nitrogen	4.80	200	0 – 302	38.4%[b]	1s

[a] 1s = single-stage operation, 2s = two-stage operation

[b] cathode flow was set to 1.0 mg/s of xenon for argon and nitrogen operating conditions

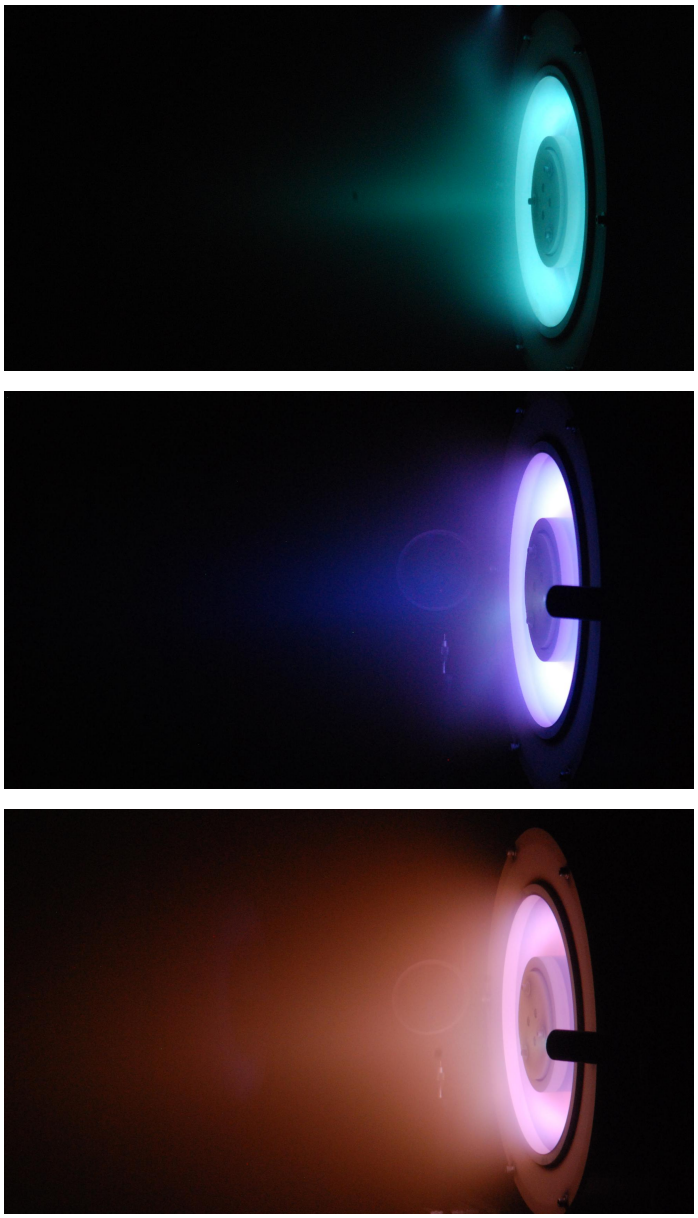

Figure 6.13: Single-stage HHT operation with xenon (top), argon (middle) and nitrogen (bottom) propellants. No significant change to the plume structure was observed when operating in two-stage mode.

6.2.1 Single-stage operation

Results of the HHT single-stage performance test are shown in Figs. 6.14 to 6.16. Figure 6.14 shows the thrust measurements, where thrust uncertainties are smaller than the marker height. The trend in thrust follows the expected result that thrust increases with both discharge voltage and anode mass flow rate.

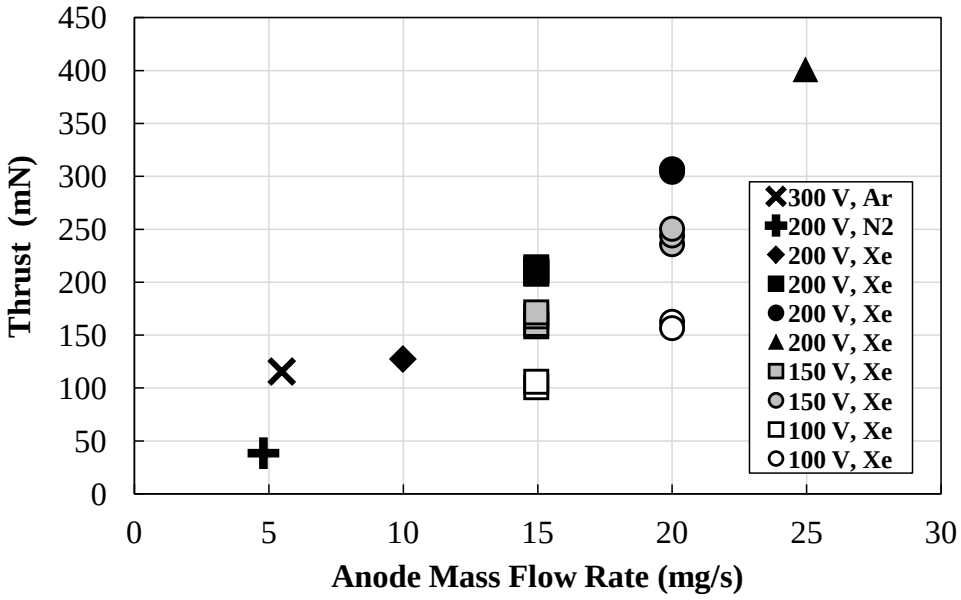

Figure 6.14: HHT single-stage thrust versus mass flow rate. No RF power is applied during single-stage operation.

The specific impulse measurements are plotted in Fig. 6.15. The results show that the HHT anode specific impulse mainly increases with increasing discharge voltage for xenon. However, the specific impulse is affected by the propellant species. Despite being much lighter than xenon, nitrogen produces a lower specific impulse during 200-volt operation.

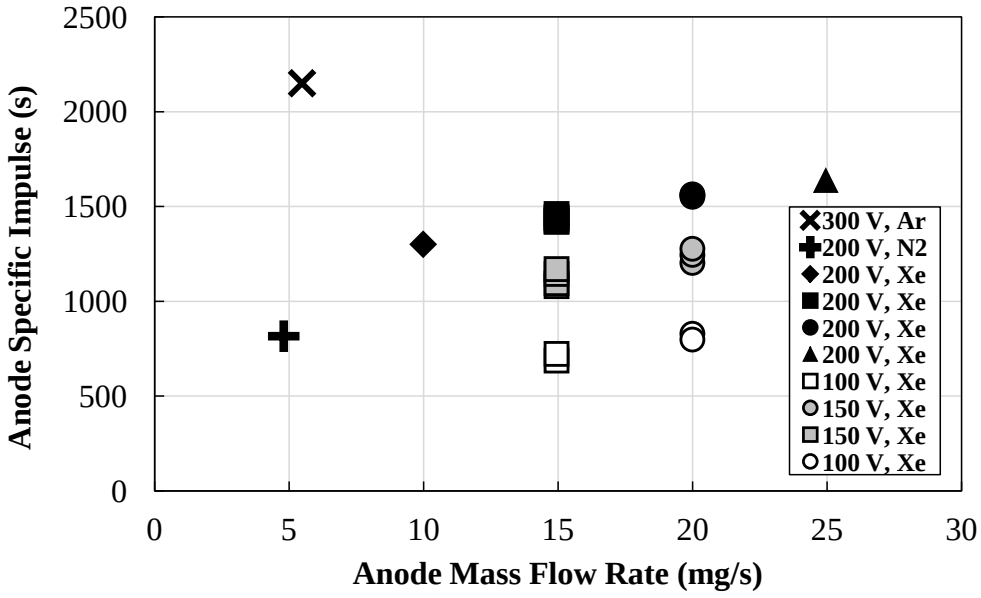

Figure 6.15: HHT single-stage anode specific impulse versus mass flow rate.

The thrust-to-power of the HHT discharge is plotted in Fig. 6.16. The results show that the thrust-to-power of the HHT operating with xenon is consistently between 60 and 72 millinewtons per kilowatt. However, the HHT thrust-to-power is much lower when operating on nitrogen or argon.

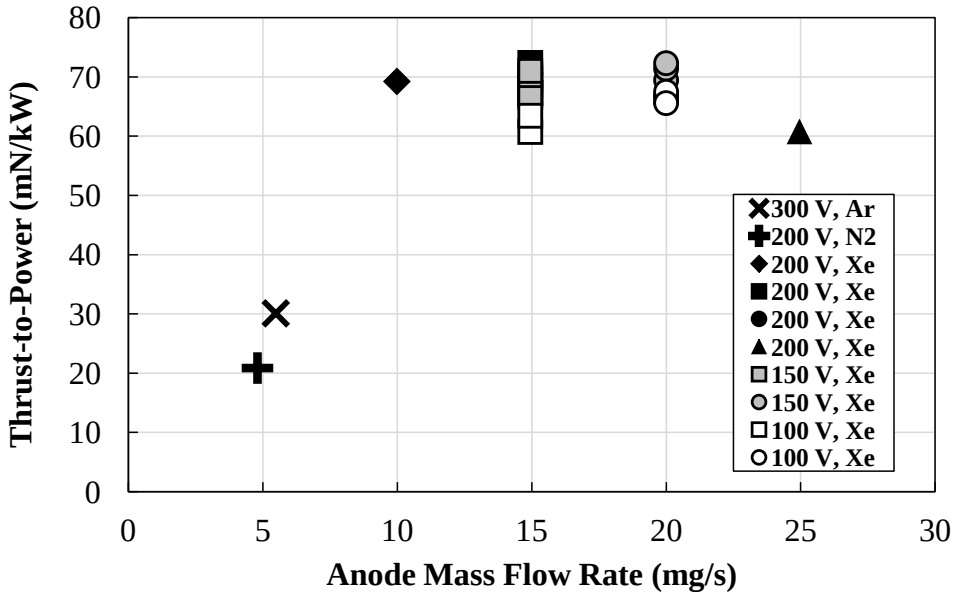

Figure 6.16: HHT single-stage thrust-to-power versus mass flow rate.

When operating with xenon propellant, thrust-to-power increases slightly with increasing discharge voltage, and is maximized at the intermediate anode mass flow rates. The HHT performance operating on argon and nitrogen was measured at higher discharge voltages, but thrust-to-power was only 30 and 21 millinewtons per kilowatt, respectively.

6.2.2 Two-stage operation

During two-stage operation, the HHT RF ionization stage was powered in the attempt to increase the anode efficiency at high thrust-to-power. The magnets in the helicon section were held constant as RF power was increased, since it was seen that the magnets for the helicon stage could act as trim coils for the Hall stage when no RF power was used.

Figure 6.17 plots the HHT two-stage thrust measurements. Thrust increases slightly with increasing RF power at all HHT operating conditions.

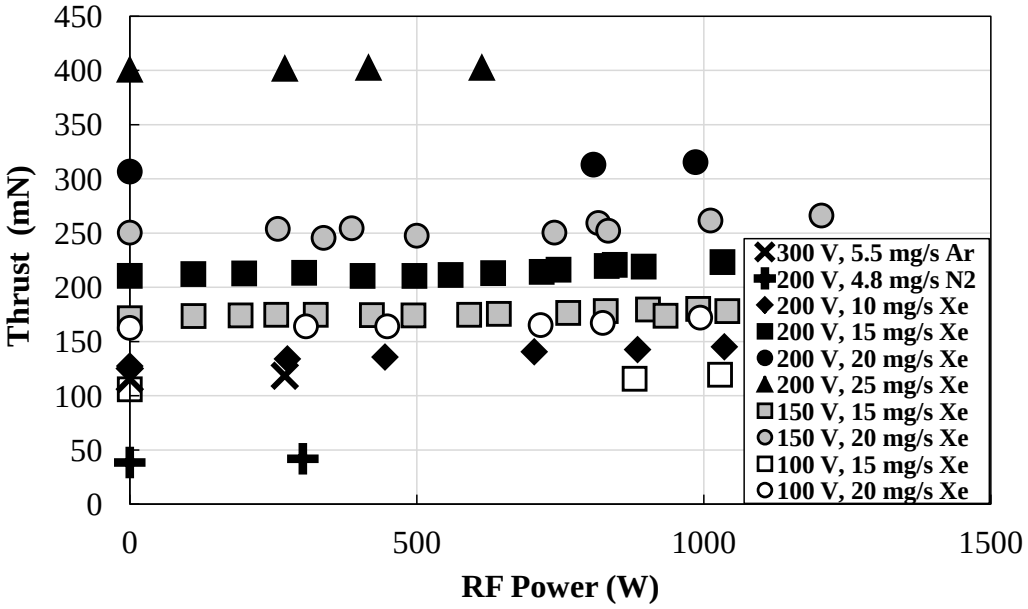

Figure 6.17: HHT two-stage thrust versus RF power. During two-stage operation, the magnet settings and DC discharge power are held constant while RF power is increased.

Figure 6.18 plots the HHT two-stage specific impulse measurements. Like thrust, the HHT anode specific impulse increases slightly with increasing RF power for all operating conditions. The argon and nitrogen operating conditions appear to be affected a little more strongly than the xenon operating conditions.

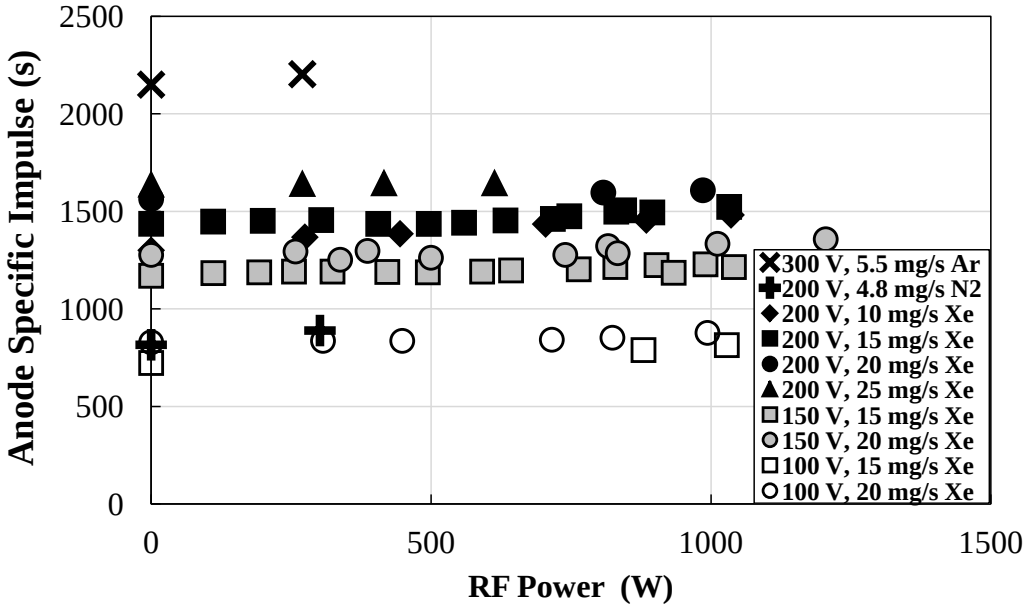

Figure 6.18: HHT two-stage anode specific impulse versus RF power.

Figure 6.19 plots the HHT two-stage thrust-to-power, with RF power included. The rate of increase in thrust was always exceeded by the rate of increase in power. Thus, the overall thrust-to-power decreases with increasing RF power for all HHT operating conditions.

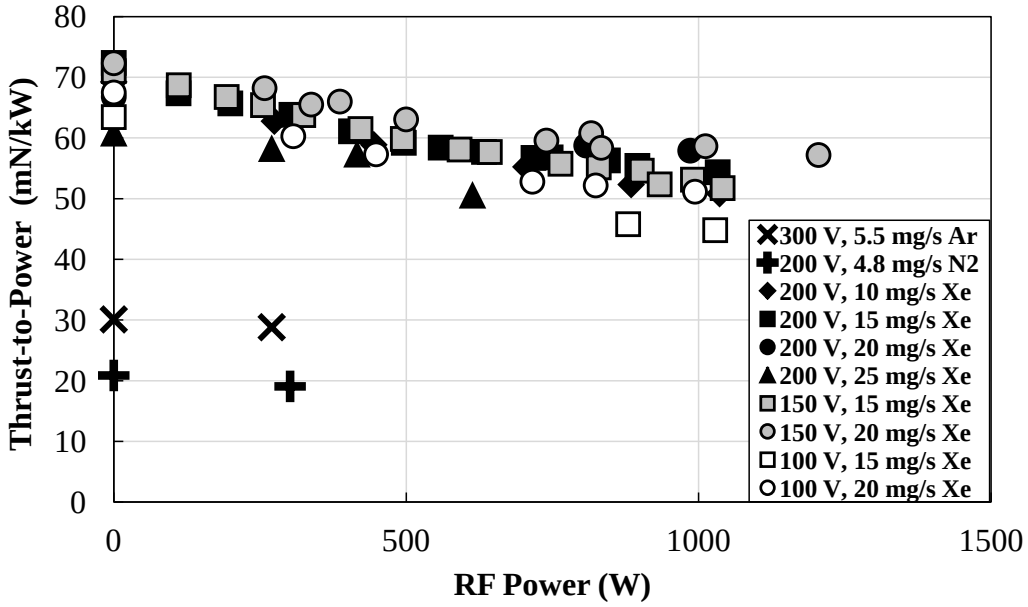

Figure 6.19: HHT two-stage thrust-to-power, including both P_{DC} and P_{RF}, versus RF power.

Figure 6.20 focuses on the gas species of greater interest to air-breathing EP. The RF stage clearly does not improve the thrust-to-power of the HHT operating on nitrogen.

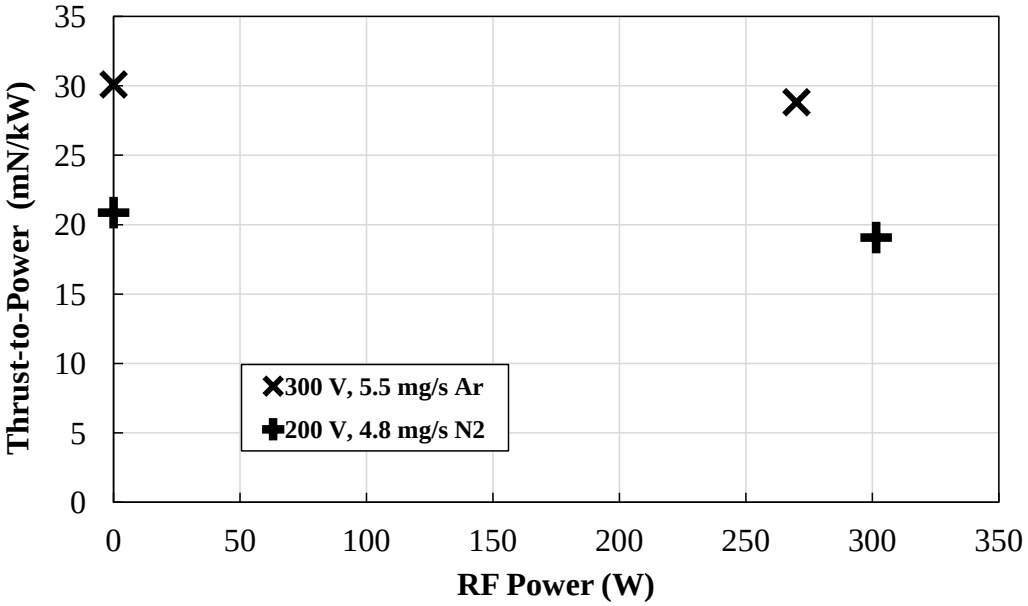

Figure 6.20: HHT two-stage thrust-to-power for the argon and nitrogen operating points.

CHAPTER 7

Discussion

The efficiency of the RPT was measured to be very low. Although the RF stage increased the thrust of the HHT, increasing the RF power did not improve the HHT's overall efficiency. This chapter discusses the results of the RPT and HHT performance measurements, with the intent of identifying the loss mechanisms in both thrusters. This chapter first describes an efficiency methodology for the RPT to lay a framework for examining the loss mechanisms. The probe measurements in the RPT plume are then analyzed according to the methodology. The second section then describes an efficiency methodology that can be applied to the HHT during both single- and two-stage operation. Then, the probe measurements in the HHT plume are analyzed to investigate the effect of the RF stage on HHT operation.

7.1 RPT

The efficiency of the RPT is measured to be quite low. Previous work in similar devices measured ion beams emanating from the exit of helicon plasma source tubes [75, 100, 135]. Thus, an ion beam is thought to be the physical mechanism for producing thrust in the RPT. The efficiency methodology described below assumes that this is the case, as well. Although the physics of devices similar to the RPT is an active area of research, describing the methodology for analysis provides a basis for examining the plasma emanating from the thruster with probe diagnostics.

7.1.1 RPT Methodology

The efficiency of a thruster may be broken down into components to reveal the loss mechanisms responsible for lowering performance. The thrust of the RPT is assumed to be generated by a reaction force with an ion beam. In order to study the losses in the RPT, the thrust-producing ion beam is broken down into three main components that can be related to plasma plume measurements: 1) the flow rate of ions in the exhaust, $\dot{m}_i$, 2) the velocity of the exhaust ions, v_i, and 3) the effective divergence of the beam, $\cos\theta_{div}$. These components are determined by the plasma measurements shown in Eq. 7.1, where F_i is the thrust produced by the ion beam, I_{beam} is the total current of accelerated ions emanating from the thruster, V_i is the effective acceleration voltage of the beam ions, and I_{axial} is the axial component of the beam ion current. The ions are assumed to have identical mass, m_i, and charge, q.

$$F_i = \dot{m}_i v_i \cos\theta_{div} = \left(\frac{I_{beam} m_i}{q}\right)\left(\frac{2qV_i}{m_i}\right)^{1/2}\left(\frac{I_{axial}}{I_{beam}}\right) \tag{7.1}$$

The total thruster efficiency, η_t, is calculated by dividing the kinetic power contained in the thrust-producing ion beam by the total electrical power supplied to the RPT. The RPT is designed to produce a wide range of magnetic field geometries, but it is not optimized for magnet power dissipation. So, the RF power, P_{RF}, and the power supplied to the magnets, P_{mag} are separated according to Eq. 7.2, where F_{RF} is the thrust due to RF power, and $\dot{m}$ is the propellant mass flow rate.

$$\eta_t = \frac{F_{RF}^2}{2\dot{m}\left(P_{RF} + P_{mag}\right)} = \frac{F_{RF}^2}{2\dot{m}P_{RF}}\frac{1}{\left(1 + \frac{P_{mag}}{P_{RF}}\right)} = \eta_{RF}\eta_{mag} \tag{7.2}$$

If a measurement of the true RF power delivered to the antenna, $P_{RF,A}$ is taken, then the RF power transmission efficiency and antenna efficiency, η_A, may be determined. Assuming that the cables used to transmit the RF power are lossless, the transmission efficiency

is reduced to a matching network efficiency, η_M, as shown by Eq. 7.3, where η_{RF} is the RF thrust efficiency. Note that this further breakdown requires measurements of the RF voltage and current at the antenna, which are not available in the RPT experiment. Detailed measurements of the plasma may also theoretically determine the plasma-antenna coupling efficiency (i.e. the fraction of the RF power delivered to the antenna that is absorbed by the plasma), but that is beyond the scope of this dissertation.

$$\eta_{RF} = \frac{F_{RF}^2}{2\dot{m}P_{RF,A}}\frac{P_{RF,A}}{P_{RF}} = \eta_A\eta_M \tag{7.3}$$

The RF thrust efficiency is further broken down into three components that represent physical attributes of the thruster exhaust. These component efficiencies can be determined from telemetry and plasma measurements according to Eq. 7.4. Other methodologies may instead refer to the specific losses that certain measurements determine [69].

$$\eta_{RF} = \Phi_P\eta_{BP}\Psi_B = \left[\frac{I_{beam}m_i}{q\dot{m}}\right]\left[\frac{I_{beam}V_i}{P_{RF}}\right]\left[\frac{I_{axial}}{I_{beam}}\right]^2 \tag{7.4}$$

The propellant utilization efficiency, Φ_P, represents the fraction of the neutral gas flow that is ionized and contributes to the exhaust ion beam. The beam power efficiency, η_{BP}, is the ratio of the total power in the beam to the input RF power. Finally, the beam efficiency, Ψ_B, accounts for the cosine losses due to the divergence of the exhaust plume.

7.1.2 Probe Results

From the Faraday probe results, and assuming that only singly-charged ion species are present, the propellant utilization efficiency is calculated according to Eq. 7.5.

$$\Phi_P = \frac{I_{beam}m_i}{e\dot{m}} \tag{7.5}$$

The Faraday probe results are also used to determine the beam efficiency, according to Eq. 7.6.

$$\Psi_B = \left(\frac{I_{axial}}{I_{beam}} \right)^2 \tag{7.6}$$

Four RPT operating points were measured with the Faraday probe in ion saturation. The results of these measurements are shown in Fig. 7.1. The propellant utilization efficiency in the RPT remained below 16%. Although differences in the RF power may confound the trends observed, the propellant utilization clearly decreased with increasing flow rate.

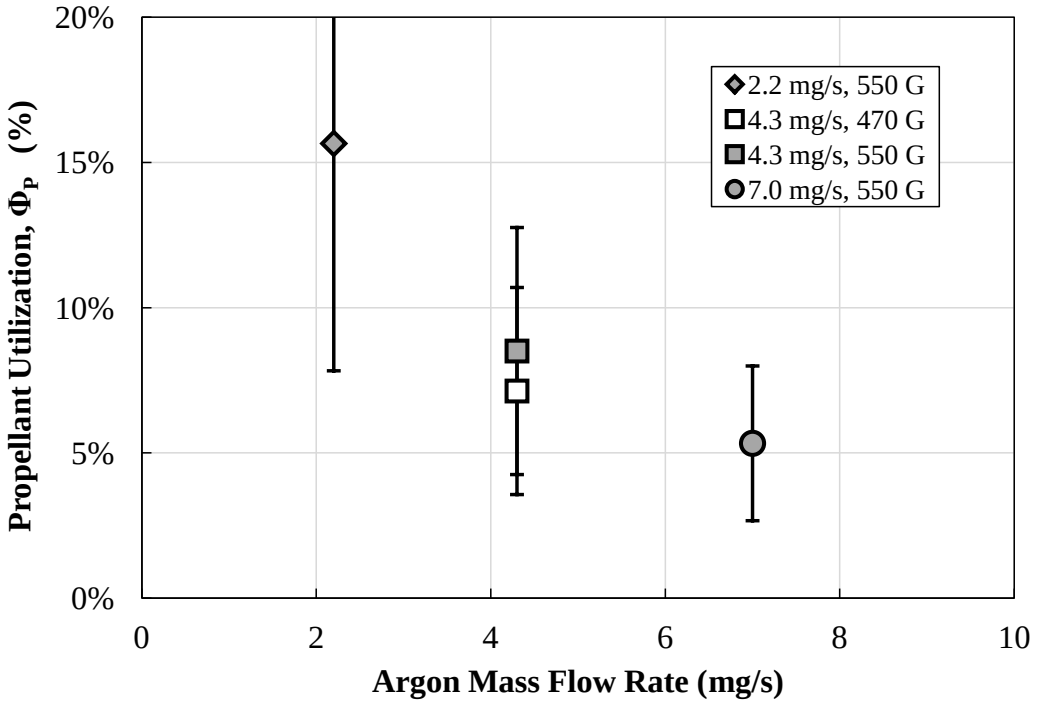

Figure 7.1: RPT propellant utilization efficiency calculated from Faraday probe data.

From Eq. 7.1 and the Faraday probe results, the effective acceleration voltage, V_i, of the exhaust ions required to account for the measured thrust can be determined with Eq. 7.7. Results from this calculation and the probe measurements are presented in Table 7.1.

$$V_i = \left(\frac{e}{2m_i} \right) \left(\frac{F_{RF}}{I_{axial}} \right)^2 \tag{7.7}$$

Table 7.1: RPT Probe analysis and theoretical acceleration potential results.

$\dot{m}$ (mg/s)	B_z (G)	P_{RF} (W)	F_{RF} (mN)	η_{RF} (%)	I_{beam} (A)	I_{axial} (A)	θ_{div} (deg)	Ψ_B (%)	Φ_P (%)	V_i (V)	V_{mp} (V)
2.4	550	1080	4.15	0.34	0.82	0.55	48	45	14	33.7	68.4
4.7	470	1210	3.47	0.11	0.74	0.48	49	42	6.5	30.9	75.0
4.7	550	1068	3.98	0.16	0.87	0.60	46	48	7.8	26.2	62.3
7.6	550	961	4.86	0.16	0.89	0.59	48	44	4.9	40.9	55.5

If the ions measured by the probe diagnostics are the thrust-bearing species in the RPT, then the thrust due to RF power should increase both with increasing axial ion beam current and with increasing beam ion energy, assuming that beam divergence does not change significantly between operating conditions. The results in Table 7.1 indicate that the thrust does indeed correlate with axial ion beam current, and that there is relatively little change in the beam divergence between conditions.

Table 7.1 also suggests that the most probable voltage of the ions measured by the RPA is sufficient to provide the kinetic energy necessary to explain the thrust. If all else remains equal, the thrust should also be proportional to the square root of the average beam ion kinetic energy (i.e. if the plasma potential is nearly constant, then thrust should also correlate with $\sqrt{V_{mp}}$). However, the results plotted in Fig. 7.2 show that there is a negative correlation between thrust and most probable potential in the RPT. One explanation for this trend might be that the beam current decreases when beam voltage increases, with the net result that thrust decreases.

Typically in Hall thruster plume analysis, the plasma potential from a Langmuir probe is subtracted from the most probable potential determined by the RPA to obtain the true exhaust ion acceleration voltage [114]. The same analysis should hold for the RPT, and if the assumption is made that only singly-charged ions are present, then the difference $V_{\mathrm{mp}} - V_p$ represents the most probable kinetic energy of the beam ions emanating from the RPT. As shown in Fig. 7.3, this quantity is approximately zero for almost all RPT operating conditions, , within the uncertainty limits. This result suggests that the kinetic energy each exhaust ion contributes to the thrust is not only dependent on V_{mp}.

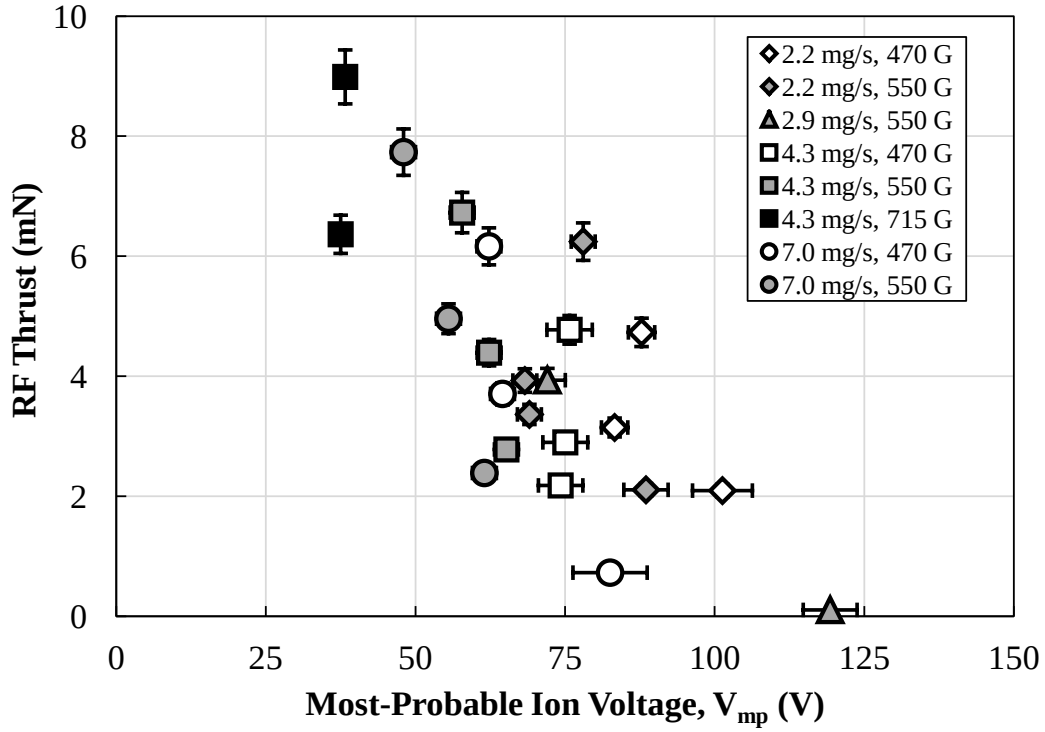

Figure 7.2: RPT thrust due to RF power versus plume most probable potential measured from RPA. The negative correlation between most probable potential and thrust may be due to a decreasing beam ion current. However, the amount of beam current data available is not sufficiently large to confirm or refute this.

The high plasma potential measured in the RPT exhaust may be explained by the fact that the quartz tube and magnetic field isolate the plasma from the facility ground. Due to the higher mobility of electrons, the plasma is expected to have a plasma potential that is greater than facility ground potential. Thus, the outflow of plasma ions from the quartz tube should be governed by ambipolar diffusion.

If an ion beam is *not* the source of the thrust produced by the RPT, then there must be another explanation for the increase in performance seen with increasing RF power. The measured cold gas thrust of the RPT nearly matched the theoretical result using the supersonic isentropic flow equations. So, gas heating mechanisms are considered here to explain the RPT thrust. To give a first-order estimate for the potential performance gain due to gas heating in the RPT, two scenarios are considered: 1) supersonic, isentropic expansion, and 2) free-molecular thermalization with the quartz tube.

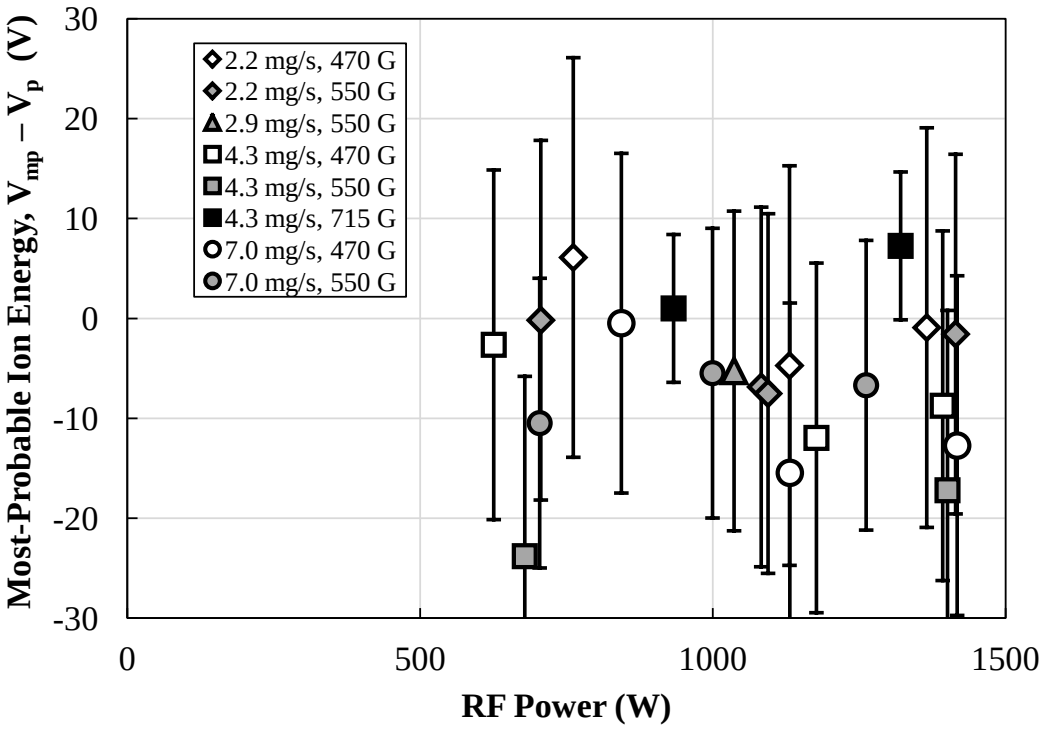

Figure 7.3: RPT ion beam most probable potential measured by the RPA minus local plasma potential measured by a Langmuir probe. This difference is typically used to define the beam most probable kinetic energy.

Assuming that the nozzle area ratio and specific heat ratio are both constant, the exit velocity of a supersonic, isentropic expansion is determined only by the stagnation temperature. The melting point of quartz is approximately 2000 degrees kelvin. No deformation of the RPT quartz tube was observed during RPT testing, but this is taken to be an upper limit on the effective temperature caused by the RF power. The result of the calculation using a 2000-degree kelvin inlet stagnation temperature and the real RPT geometry gives a specific impulse of 145 seconds. Comparing this to Fig. 6.5, there is some evidence that gas heating may have an effect at higher flow rates, as the RPT specific impulse does not exceed 160 seconds at any 7.0-milligram per second operating condition. However, this result is an optimistic assessment of the upper bound of this effect in the RPT, and the calculation requires assumptions that are not strictly satisfied in the real RPT. That said, charge-exchange collisions may produce hot or "super-thermal" argon neutrals with a translational temperature greater than 2000 degrees kelvin. These hot neutrals may in-

crease the effective temperature of the propellant, depending on the rates at which they are produced and lost.

A free-molecular thermalization process may also be considered for the acceleration of argon neutrals. Recall that the mean speed of a Maxwellian distribution of gas particles is determined by the temperature and the mass of the gas species, according to Eq. 3.37. If the argon propellant enters the RPT quartz tube at room temperature, thermalizes to the wall temperature through collisions, and then exits at the wall thermal velocity, then a net force can be imparted to the tube due to the change in thermal velocity. Again taking the melting temperature of quartz as the upper limit on the gas exit temperature, a population of argon at 2000 degrees kelvin has a mean thermal speed of 1030 meters per second, corresponding to a specific impulse of 105 seconds. The 2000-degree kelvin assumption is again optimistic (and perhaps unrealistic) for the real RPT conditions, and comparing this result to Fig. 6.5 suggests that this type of gas heating is unlikely to have a strong influence on RPT performance.

Although a gas heating mechanism should contribute to the thrust of all gases (not necessarily equally), nitrogen and air have vibrational and rotational energy modes that will absorb some of the thermal power. If the rotationally and vibrationally excited molecules escape the RPT before reaching equilibrium with the translational energy modes, then the gas "heating" will not contribute to thrust. This loss mechanism is analogous to the "frozen flow" losses in chemical rocket nozzles. However, the neutral gas flow in the RPT is a weakly collisional, non-equilibrium flow, and so it is difficult to model the gas behavior accurately.

Recent experiments have measured the thrust in a device similar to the RPT. These experiments concluded that the thrust is produced by an increased electron pressure in the quartz tube, and by an azimuthal electron current in the expanding magnetic field region that exerts a J$\times$B force [112]. Other experiments have suggested that thrust is produced by "neutral pumping" due to charge-exchange collisions in the source tube [136]. Measure-

ments in a low-pressure argon processing chamber suggest that a significant amount of fast neutrals can be created due to charge-exchange collisions [137]. Argon charge-exchange collision cross-sections taken from Hegerberg et al. [138] and Rao et al. [139], are used to calculate the effective mean free path for charge-exchange versus collision energy. The result of this calculation is plotted for multiple neutral pressures in Fig. 7.4.

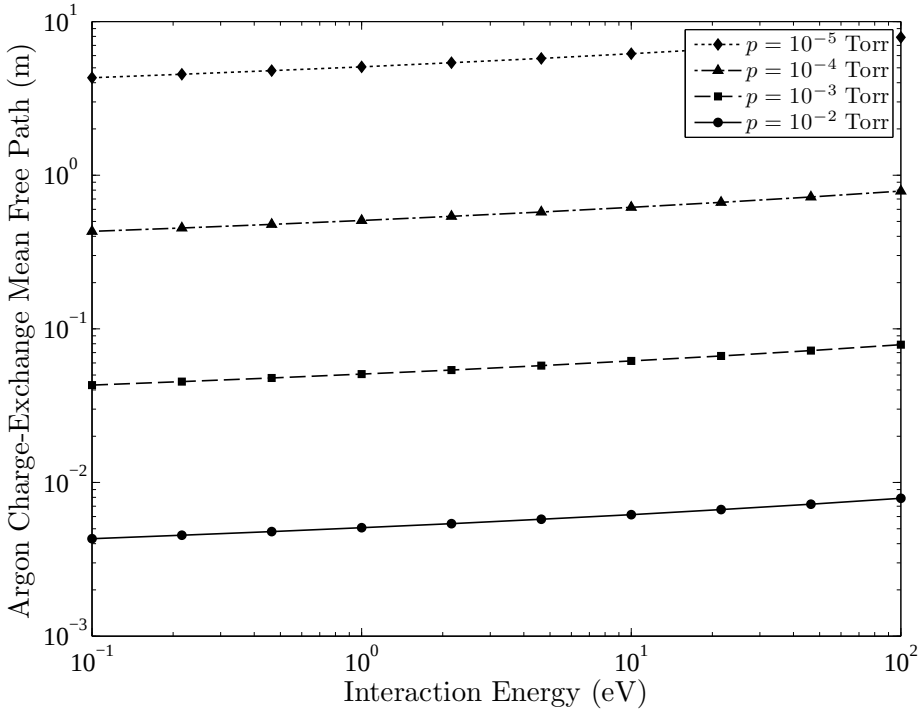

Figure 7.4: Mean free path for charge exchange collisions between argon ions and neutrals. The corrected LVTF pressure when operating with argon did not exceed 4.7 $\times$ 10^{-6} Torr, but the pressure in the RPT quartz tube may be as high as a few millitorr during operation.

Reid demonstrated that flow simulations using FLUENT give an order of magnitude agreement with direct-simulation monte carlo and particle-in-cell simulations of the flow in a Hall thruster discharge channel [140]. FLUENT simulations of the RPT gas path showed that the pressure inside the quartz tube ranges from 1 to 10 millitorr [141]. This puts the mean free path for argon charge-exchange collisions in the range of approximately 0.4 to 8 centimeters. Most of the ions created near the inlet side of the quartz tube are therefore likely to undergo charge-exchange collisions that can create fast neutrals. The fast neutrals are not influenced by electric or magnetic fields, and so they may be likely

to collide with the quartz tube. Argon ions created near the exit of the quartz tube, on the other hand, may be able to escape prior to experiencing a charge-exchange collision. This is because the low background pressure outside of the RPT increases the mean free path for charge-exchange to many meters. The single-voltage population of ions measured by the RPA may therefore represent the ions that are created near the exit plane and escape into the LVTF at the ambipolar velocity. The results would then agree with the theory suggested by Fruchtman for a collisional-plasma thruster [136].

7.2 HHT

The plasma in the exhaust plume of the HHT was measured with a Faraday probe, an RPA, and a Langmuir probe while the HHT was operating in both single-stage and two-stage modes with argon, nitrogen, and xenon propellant. When comparing the single- and two-stage operation modes, thrust increased slightly with RF power, but the HHT thrust-to-power and total anode efficiency both consistently decreased with increasing RF power. The probe results are used with the methodology described below in order to investigate the effect of the RF stage on the physics of the HHT operation.

7.2.1 HHT Efficiency Methodology

There is much previous work regarding the breakdown of the total efficiency of a Hall thruster into component quantities [114, 142]. The component efficiencies are generally determined by thruster telemetry, thruster performance measurements, and plasma probe diagnostics in the thruster exhaust plume. The component efficiencies represent values that reveal the physical nature of thruster loss mechanisms.

The total efficiency, η_t, of any EP thruster is simply the kinetic power of the thrust-producing component of the exhaust, P_{jet}, divided by the total electrical power consumed by the thruster, P_{elec}, as shown by Eq. 7.8, where $\dot{m}$ is the propellant mass flow rate, v_{ex} is

the effective propellant exhaust velocity, P_d is the discharge power, and P_{mag} is the power supplied to the magnets.

$$\eta_t = \frac{P_{jet}}{P_{elec}} = \frac{\frac{1}{2}\dot{m}v_{ex}^2}{P_d + P_{mag}} \tag{7.8}$$

In laboratory-model Hall thrusters, such as the HHT, the magnetic circuit design is generally not optimized for power consumption, and so a magnet power efficiency, η_{mag}, is separated accordingly. In addition, the cathode is not always optimized as it would be on a flight model thruster, so the cathode efficiency, η_c, is also separated. The results of this breakdown allow the discharge or anode efficiency, η_d or η_a, respectively, to be individually examined, as shown in Eq. 7.9, where $\dot{m}_a$ is the anode mass flow rate, and $\dot{m}_c$ is the cathode mass flow rate.

$$\eta_t = \frac{\frac{1}{2}\dot{m}_a v_{ex}^2}{P_d}\left(1 + \frac{\dot{m}_c}{\dot{m}_a}\right)\frac{1}{\left(1 + \frac{P_{mag}}{P_d}\right)} = \eta_a \eta_c \eta_{mag} = \eta_d \eta_{mag} \tag{7.9}$$

Brown et al. suggest that using the "voltage exchange parameter," E_1, and the "mass exchange parameter," E_2, can reveal loss mechanisms using only telemetry and thrust measurements, as shown in Eq. 7.10 [142], where F_{thrust} is the thrust force, V_d is the discharge voltage, $\mathcal{F}$ is the Faraday constant, $\mathcal{M}$ is the propellant molecular mass, I_d is the discharge current, Φ_P is the propellant utilization efficiency, Ψ_B is the beam divergence efficiency (also called the "beam efficiency" here), η_V is the voltage utilization, and η_I is the current utilization.

$$\eta_d = E_1 E_2 = \left[\frac{\frac{1}{2}\left(\frac{F_{thrust}}{\dot{m}}\right)^2}{V_d\left(\frac{\mathcal{F}}{\mathcal{M}}\right)}\right]\left[\frac{\dot{m}\mathcal{F}}{I_d\mathcal{M}}\right] = \left[\Phi_P \Psi_B \eta_V\right]\left[\eta_I\right] \tag{7.10}$$

The voltage exchange parameter is proportional to the square of the thrust, and it relates the acceleration voltage to the divergence and dispersion of the exhaust jet. The mass exchange parameter is inversely proportional to the discharge current, and it relates the input propellant flow rate to the output charge flow rate. Further analysis beyond the exchange parameters requires the use of probe diagnostics in the thruster exhaust plume.

The difference between single-stage and two-stage HHT operation is that two-stage op-

eration uses RF power to affect the discharge in the vicinity of the gas inlet manifold. This is accounted for in the efficiency architecture by separating the DC and RF components of electrical power in the discharge, P_{DC} and P_{RF}, respectively, as shown in Eq. 7.11, where η_{PRF} is called the "RF efficiency."

$$\eta_d = \frac{\frac{1}{2}\dot{m}_a v_{ex}^2}{P_{DC} + P_{RF}}\eta_c = \eta_a \frac{1}{\left(1 + \frac{P_{RF}}{P_{DC}}\right)}\eta_c = \eta_a \eta_{PRF} \eta_c \tag{7.11}$$

This definition of RF efficiency is compatible with the single-stage efficiency architecture, since $\eta_{PRF} = 1$ when zero RF power is used. The exchange parameters can therefore retain their definition from Eq. 7.10. This allows the effect of the RF power on thruster performance characteristics to be examined through the exchange parameters. In order to evaluate the net effect of RF power on propulsive efficiency, however, the RF efficiency must also be included.

7.2.2 HHT Single-Stage Losses

In order to examine the HHT loss mechanisms during operation with alternative propellants, the exchange parameters are first plotted as a function of anode mass flow rate. The cathode flow is xenon for all operating conditions. So, the weighted average molecular mass of the cathode and anode flow is used in the exchange parameter calculations. The voltage exchange parameter, E_1, is plotted in Fig. 7.5. The results show that the voltage exchange parameter generally increases with anode mass flow rate and with discharge voltage. Although the nitrogen and argon operating conditions were at higher discharge voltages, E_1 remained low for both. The argon operating condition E_1 was comparable to the 100-volt, 15-milligram per second xenon case, despite operating at 300 volts. Linearly extrapolating the 100-volt xenon points to lower flow rates would appear to intersect the nitrogen operating point. Thus, it may simply be the low mass flow rate that explains the low value of E_1. The argon operating point appears that it may have a lower E_1 than would a 300-volt operat-

ing condition with an equivalent xenon mass flow rate. The lower E_1 for argon and nitrogen reflects the fact that the effective exhaust velocity of the propellant is very low, considering the low molecular mass of the propellant and the high discharge voltage. This means that HHT is suffering from either a 1) lower propellant utilization, 2) larger beam divergence, or 3) lower voltage utilization when operating with argon and nitrogen as opposed to xenon.

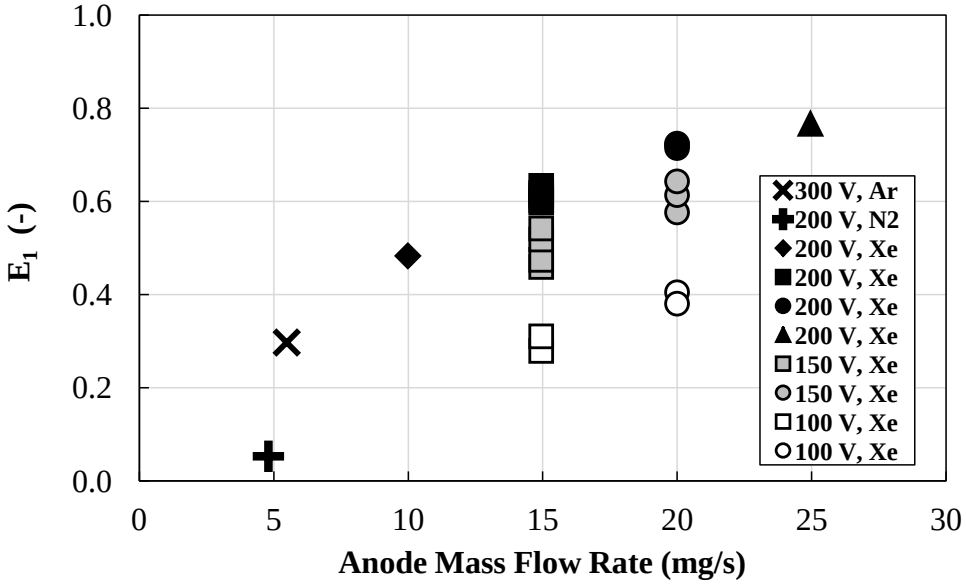

Figure 7.5: HHT single-stage voltage exchange parameter versus anode mass flow rate. E_1 relates the effective exhaust velocity of the plume to the discharge voltage, taking into account the molar mass of the propellant.

The mass exchange parameter, E_2, is plotted in Fig. 7.6 versus anode mass flow rate. The results show that the mass exchange parameter for xenon operation decreases with anode mass flow rate, and is not significantly affected by discharge voltage. E_2 for argon appears to follow the trend for xenon, but E_2 for nitrogen is much higher. The mass exchange parameter compares the rate of charge flow out of the thruster to the flow of propellant molecules into the thruster. Thus, the high value of E_2 for nitrogen may suggest that a significant portion of the molecular nitrogen propellant is dissociating into atomic nitrogen, and contributing more than one electron to the discharge.

The HHT beam efficiency is calculated from the Faraday probe data, and the results are

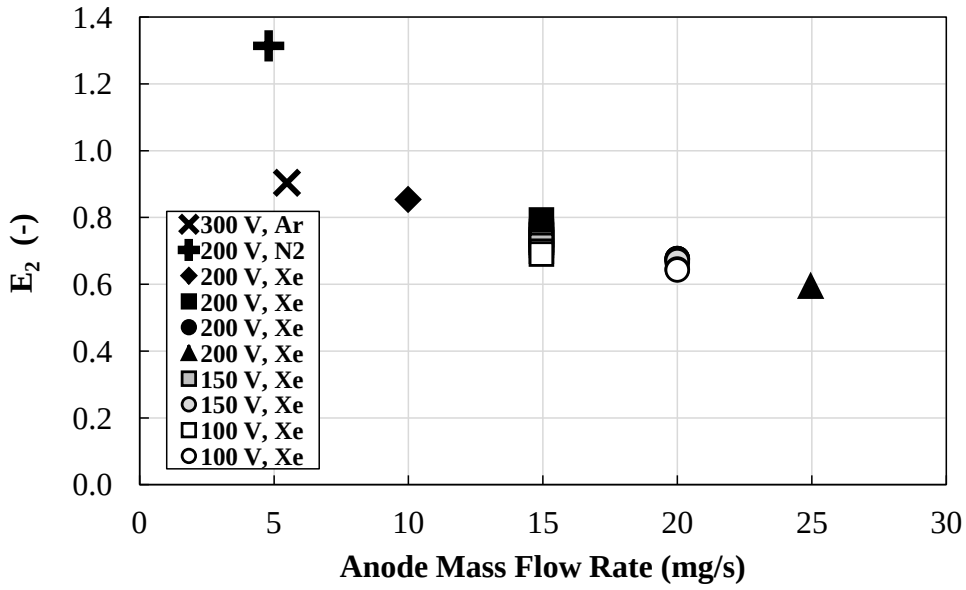

Figure 7.6: HHT single-stage mass exchange parameter versus anode mass flow rate. E_2 relates the output flow of charge in the thruster to the inflow of propellant.

shown in Fig. 7.7. The beam efficiency is above 60% at all operating conditions, and for all propellant species. The beam efficiency during nitrogen operation is similar to that of the 100-volt xenon operating conditions.

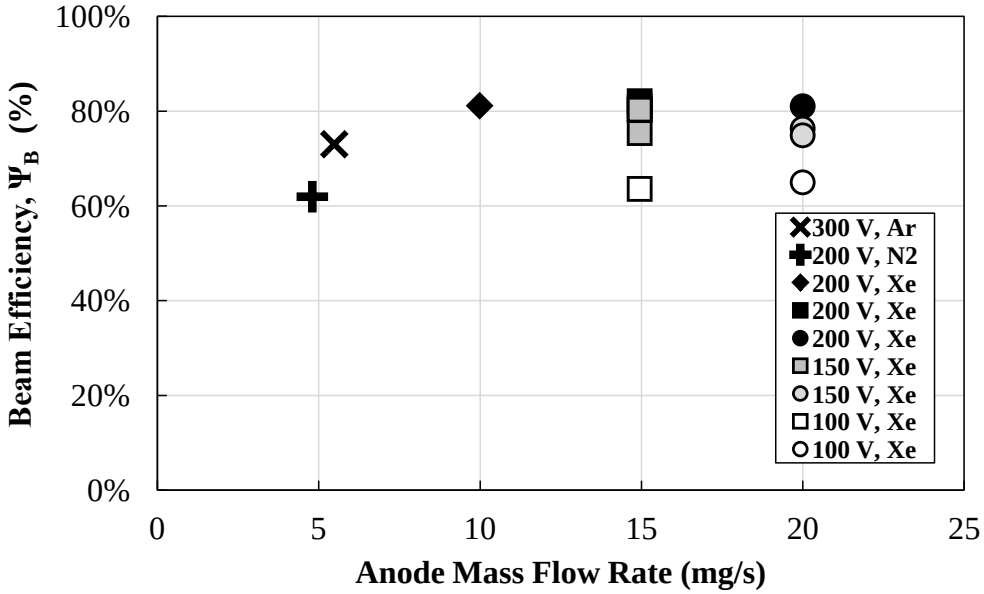

Figure 7.7: HHT single-stage beam efficiency versus anode mass flow rate. Higher beam efficiency is equivalent to a less divergent plume.

Previous experiments have shown that beam efficiency increases with increasing discharge voltage, and weakly increases with increasing anode flow rate [142]. However, Fig. 7.7 shows that the HHT's beam efficiency for the 200-volt nitrogen condition is equivalent to the 100-volt xenon conditions, and the beam efficiency of the 300-volt argon condition is nearly the same as the 150-volt xenon conditions. This result suggests that the beam divergence efficiency is affected by propellant gas species, and not simply mass flow rate. This finding is consistent with the results seen by Linell, who showed that krypton propellant consistently had a lower beam divergence efficiency than xenon for equivalent operating conditions in the NASA-173Mv1 Hall thruster [51]. Although the beam efficiency is lower for the nitrogen and argon operating points, the divergence alone does not entirely account the lower values of the voltage exchange parameter seen in both.

The HHT voltage utilization is calculated from the RPA and Langmuir probe data, and the results are plotted in Fig. 7.8.

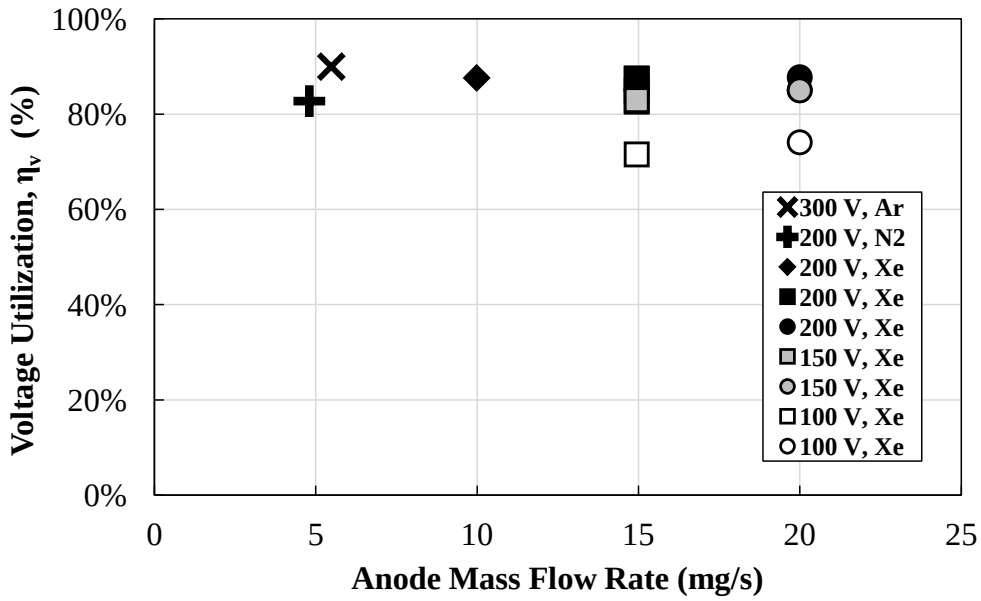

Figure 7.8: HHT voltage utilization efficiency plotted versus anode mass flow rate.

Figure 7.8 shows that the argon and nitrogen voltage utilization does not have a significant deficit compared to xenon. The slightly higher voltage utilization of the argon operating point may simply be explained by the fact that voltage utilization tends to in-

crease with increasing discharge voltage. The nitrogen operating point appears to fall in line with the 200-volt xenon trend. Discharge voltage is the dominant factor in determining voltage utilization regardless of the propellant species, further evidenced by the lower voltage utilization of the 100-volt xenon operating points.

The voltage exchange parameter is the product of the propellant utilization, the beam efficiency, and the voltage utilization. So, using the results plotted in Figs. 7.5 to 7.8 with the formula in Eq. 7.10, the propellant utilization is calculated by dividing E_1 by the beam efficiency and the voltage utilization. The resulting values are shown in Fig. 7.9.

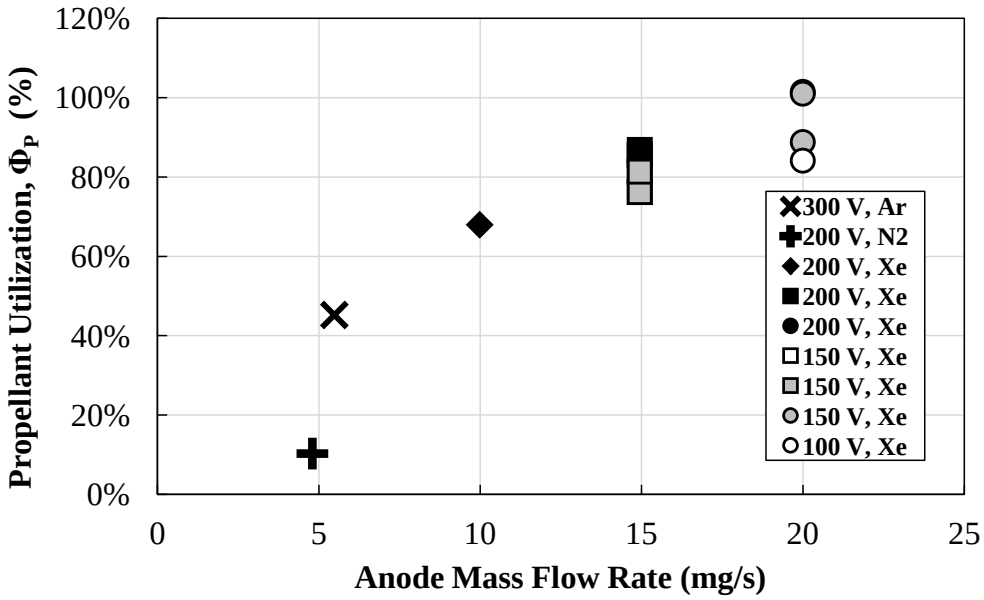

Figure 7.9: HHT propellant utilization (deduced from E_1, Ψ_B, and η_V) plotted versus anode mass flow rate. The uncertainty in the 20-mg/s extends below 100%.

This calculation shows that the HHT suffers from a very poor propellant utilization when operating with nitrogen and argon in single-stage mode. This conclusion again follows well with the results reported by Linnell, who stated that "the beam divergence accounts for a loss equally important as propellant utilization" when referring to operation with krypton versus xenon propellant [51].

Diatomic nitrogen and argon have nearly the same first ionization energy, 15.58 eV and 15.76 eV, respectively, compared to 12.13 eV for xenon [143]. However, rotational

and vibrational energy excitation can sink energy away from a nitrogen plasma, but not an argon or a xenon plasma. The decrease in propellant utilization efficiency for argon, and especially for nitrogen, is disproportionately larger than the 30% difference in ionization energy when compared to xenon. While the low efficiencies of the 100-volt xenon operating conditions are spread across mulitple loss mechanisms, the major loss for argon and nitrogen is mainly from the lower propellant utilization. This may be due in part to a shorter residence time in the discharge channel and a smaller ionization cross-section. The significantly lower value for nitrogen may be explained by the fact that a nitrogen molecule, with a bond energy of 9.8 eV, can split into a pair of nitrogen atoms, which have a 14.53 eV first ionization energy [143]. Thus, dissociation of nitrogen can sink energy away from the discharge, and transform the propellant into species that require even more energy to ionize.

7.2.3 HHT Two-Stage Losses

Since the HHT RF efficiency is defined separately from anode efficiency, the exchange parameters can be used to examine how the RF power affects the overall thruster behavior. The two-stage voltage exchange parameter is plotted against RF power in Fig. 7.10.

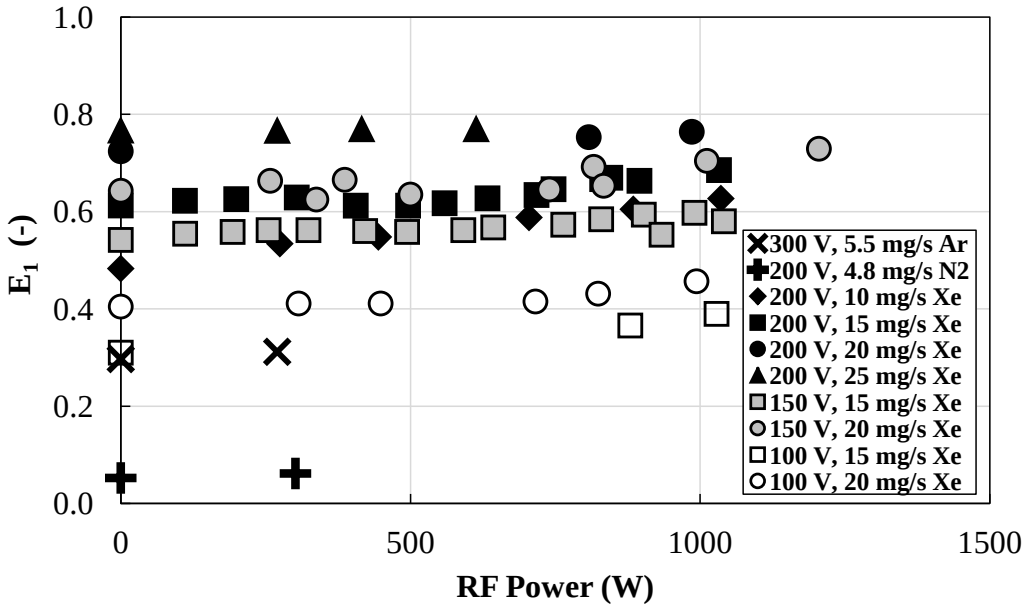

Figure 7.10: HHT two-stage voltage exchange parameter versus RF power.

Figure 7.10 shows that the voltage exchange parameter, E_1, increases slightly with RF power. This trend decreases with increasing anode mass flow rate for xenon operating conditions. At the 25-milligram per second xenon conditions, the RF power has almost no effect. The value of E_1 for the 100-volt, 20-milligram per second xenon operating condition increased by 26% with the application of 1030 watts of RF power. Only one operating point each for argon and nitrogen with RF power were measured, but 270 watts of RF caused the argon E_1 value to increase by approximately 5%, and 300 watts of RF caused the nitrogen E_1 value to increase by approximately 17%.

The HHT two-stage mass exchange parameters are plotted versus RF power in Fig. 7.10. Recall that the mass exchange parameter has the same definition as current utilization here.

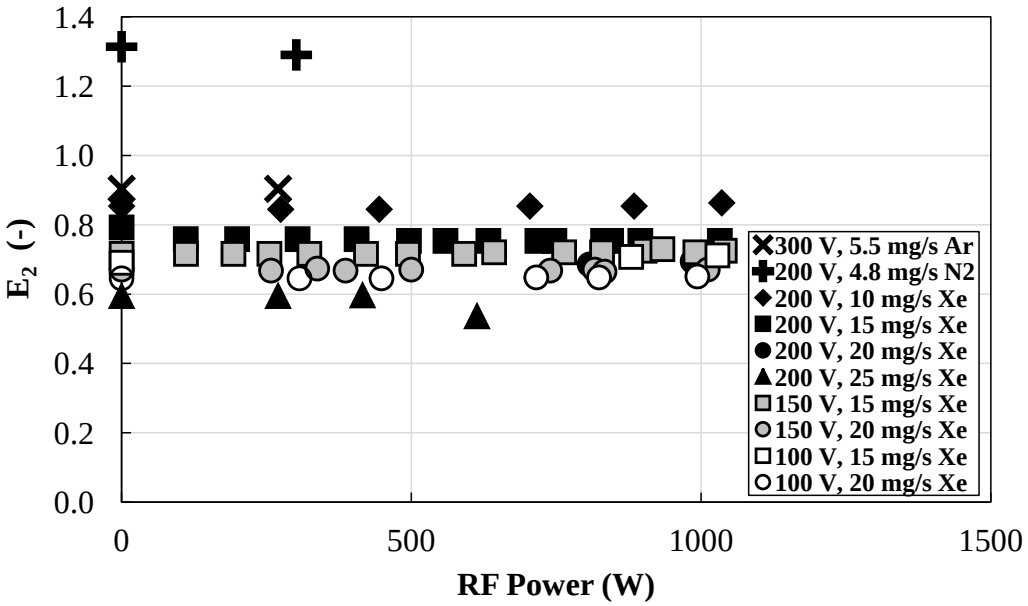

Figure 7.11: HHT two-stage mass exchange parameter versus RF power.

The mass exchange parameter, E_2, was not significantly affected by RF power at all HHT operating conditions, as shown in Fig. 7.11. However, an approximately 10% decrease in the mass exchange parameter was measured for the 200-volt, 25-milligram per second xenon condition operating with 610 watts of RF power. The value of E_2 for nitrogen decreased by about 2% with 300 watts of RF applied.

Faraday probe measurements were taken to determine the beam divergence efficiency of the HHT operating in two-stage mode. The results are plotted in Fig. 7.12.

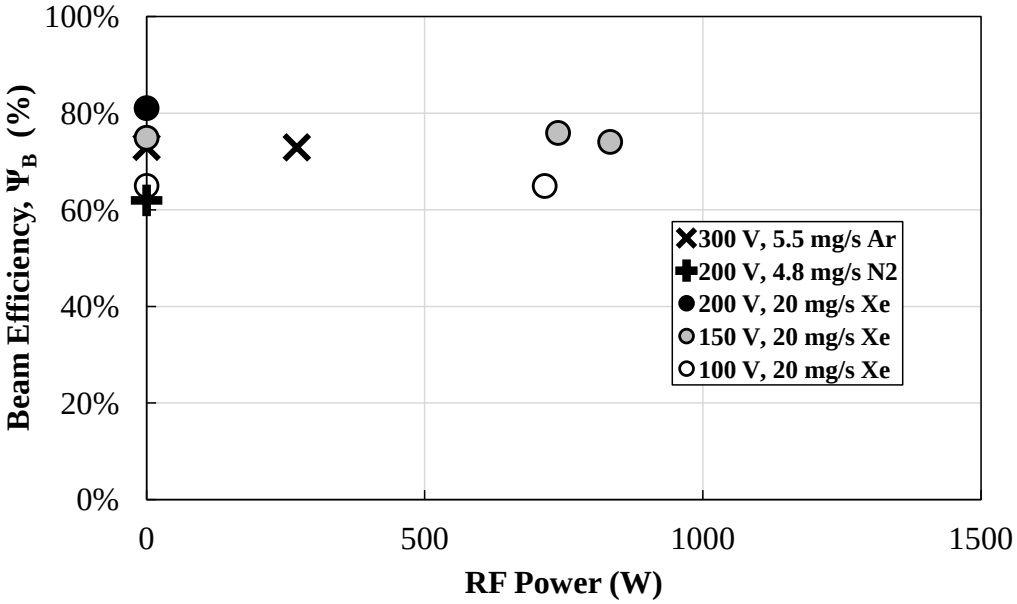

Figure 7.12: HHT two-stage beam divergence efficiency versus RF power.

For the operating conditions that were measured, the results plotted in Fig. 7.12 suggest that the RF stage did not significantly affect the beam divergence efficiency of the HHT. Although Faraday probe data was not recorded during two-stage operation with nitrogen, the two-stage value of E_1 for nitrogen was not significantly affected by the RF power. In addition, the RF stage is not designed to have a strong effect on the divergence of the thruster exhaust plume.

The voltage utilization was calculated using the RPA and Langmuir probe measurements, and with the HHT discharge voltage. The results are plotted in Fig. 7.13 versus RF power. The results indicate that the voltage utilization tends to decrease with increasing RF power. Probe data was not taken for the two-stage nitrogen operating point, but the 100-volt, 20-milligram per second xenon operating condition experienced a 9% decrease in the voltage utilization when 720 watts of RF power was applied.

The probe results together with the voltage and mass exchange parameter measurements plotted in Fig. 7.10 and 7.11 indicate that the RF power indeed increased propellant

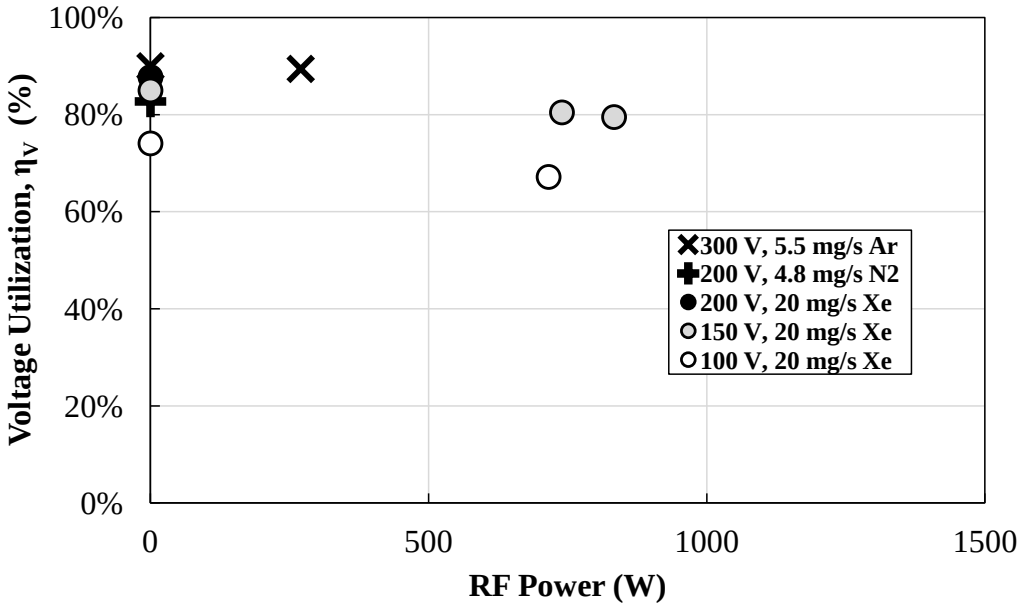

Figure 7.13: HHT two-stage voltage utilization efficiency versus RF power.

utilization efficiency. The propellant utilization of the 100-volt, 20-milligram per second xenon condition increased by 13% with 720 watts of RF power, and the propellant utilization of the argon operating condition increased by about 6%. However, the increase in propellant utilization is not sufficient to overcome the reduced efficiency due to the use of RF power. Thus, the thrust-to-power decreases with increasing RF power for all operating conditions, regardless of propellant species.

CHAPTER 8

Conclusions

This dissertation has explored whether air-breathing EP is possible with currently available technology. In particular, RF plasma technology was applied to investigate whether it may increase the performance of an air-breathing thruster. Chapter 2 showed that the concept of an air-breathing spacecraft is feasible, and that it may provide a practical benefit over a conventional electric propulsion system if it is possible to operate at approximately 200-kilometer orbit altitudes. The specific impulse requirements of an air-breathing thruster matched well with reported ion beam energies measured downstream of a helicon plasma source, but no published direct thrust measurements were available at the time. To address this void in the literature, the RPT was designed and built to test whether a helicon source could provide the thrust necessary for a small, air-breathing demonstration mission. Hall thrusters have the appropriate performance characteristics when operating with xenon, but they have specific life-limiting mechanisms, and do not operate efficiently with alternative propellants. So, the HHT was operated with nitrogen to determine whether an RF ionization stage could increase the overall efficiency of a Hall thruster operating with atmospheric gas.

8.1 Air-Breathing Thrusters

Performance measurements of the RPT showed that the overall thrust and efficiency are quite low, and that the current theoretical descriptions of helicon plasma source operation are not necessarily sufficient for designing an RF plasma thruster. Although the elimination of the hollow cathode provides a strong motivation to continue pursuing this type of thruster, the physics responsible for thrust production must be determined more concretely in order to guide the design process. The lack of thrust generated by the RPT with nitrogen and air, despite a double-peaked RPA structure and bright plasma, suggests that there is still much to be understood about how an RF thruster interacts with the propellant.

The DC acceleration voltage required for an air-breathing electric thruster is lower than the efficient operating range of Hall thrusters, but the thrust-to-power is in the appropriate range for typical Hall thruster operating on xenon propellant. Hall thrusters tend to operate at lower efficiencies when using alternative propellants, so the HHT was used to test whether an RF ionization stage could boost the overall efficiency of a Hall thruster operating with nitrogen propellant.

At approximately 20 millinewtons per kilowatt, the single-stage HHT thrust-to-power during nitrogen operation is in the range where it could allow an air-breathing spacecraft to operate below about 300-kilometer orbit altitudes. However, the RF stage did not improve the overall efficiency of the HHT. These results merit the investigation of a single-stage Hall thruster that is designed to work with nitrogen propellant. Magnetic shielding and erosion rates have not been studied in Hall thrusters operating with atmospheric gases, and the lifetime of a Hall thruster operating with nitrogen and oxygen must also be explored in order to determine whether Hall thrusters can provide a long-term air-breathing propulsion solution. In addition, the material compatibility issues between hollow cathode inserts and atmospheric gases must be resolved before a fully air-breathing Hall thruster is possible.

8.2 Future Work

Eliminating the need for a hollow cathode would greatly simplify the task of creating an air-breathing EP system. This one factor merits further investigation into ambipolar and magnetic nozzle thruster concepts like the RPT. Future work should focus on improving the knowledge of the physics responsible for producing thrust in devices similar to the RPT. Some of the physics, such as magnetic field detachment of the plasma, are difficult to study in ground-based facilities. Using smaller thrusters and larger facilities to study these phenomena may mitigate the facility effects to the point where practical knowledge can be gained.

State-of-the-art DC thrusters already have the appropriate performance characteristics to operate with atmospheric propellant. However, they require an electron source to operate. The creation of a high-current, low-power, oxygen-compatible cathode would greatly aid the development of any DC air-breathing thruster concept. Microwave cathodes have been operated on DC EP systems that have flown in space. These cathodes typically operate with xenon propellant. So, it would be beneficial to determine a microwave cathode is capable of operating at high current with atmospheric gases. Other future work related to DC thrusters might focus on the development of a Hall thruster that is magnetically shielded, and that is designed to operate with nitrogen and oxygen propellant.

In addition to the thruster, there has been very little experimental research into the design of an inlet for the air-breathing spacecraft. An efficient inlet would reduce the performance requirements of the propulsion system. Thus, it is an equally important component that must be developed concurrently with an air-breathing thruster.

To continue working with the RPT and HHT at PEPL, the following specific work could greatly improve the body of knowledge regarding RF plasma thrusters:

1. Helicon waves were not measured in the HHT or RPT. It would be beneficial to the helicon community to perform a B-dot probe study with both the HHT and the

RPT to determine whether helicon waves are excited in the plasma. There is very little published experimental work regarding annular helicon plasma sources, and no published experimental measurements of annular helicon waves.

2. The RPT thrust increased most strongly with magnetic field strength. This merits a thorough plume study with the RPT operating at even higher magnetic field strengths.

3. The matching network and antennas were not optimized to reduce ohmic dissipation. To improve RF efficiency, applying a silver-coating to all RF connections will reduce the RF circuit resistances (including connectors and antennas).

4. The losses in the matching network are unknown. The matching network should be instrumented so that measurements of the antenna voltage and current can be recorded. This will allow the study of matching network and plasma-antenna coupling efficiencies, on which there is very little published experimental work.

5. The HHT and RPT antenna designs may not have been optimal for plasma coupling, yet the HHT results indicated an increased propellant utilization efficiency. This merits a further helicon antenna design study for both the RPT and the HHT.

APPENDIX A

Atmospheric Data

Tables A.1 to A.3 show the data that was used for the air-breathing spacecraft calculations. The data is from a draft international standard by the International Organization for Standardization titled "Space environment (natural and artificial) – Earth upper atmosphere" (ISO/DIS 14222) [42]. ISO/DIS 14222 lists equatorial atmospheric reference data for 0 to 900-kilometer altitudes from the NRLMSISE-00 model for different levels of solar and geomagnetic activity. The data at 100- to 500-kilometer altitudes for low, moderate, and high solar and geomagnetic activity levels are given in Table A.1, A.2, and A.3, respectively.

Table A.1: Atmosphere constituents versus altitude for low solar and geomagnetic activity.

Altitude (km)	Density (kg/m^3)	Temp. (K)	Gas Species Number Densities (m^{-3})							
			n_O	n_{N_2}	n_{O_2}	n_{He}	n_{Ar}	n_H	n_N	$n_{Anom.\ O}$
100	6.18E-07	1.71E+02	4.78E+17	1.02E+19	2.38E+18	1.17E+14	1.04E+17	2.70E+13	3.10E+11	2.24E-37
120	1.88E-08	3.53E+02	7.23E+16	3.11E+17	4.36E+16	2.50E+13	1.36E+15	6.07E+12	1.19E+12	1.41E-27
140	3.08E-09	5.21E+02	2.12E+16	4.89E+16	4.45E+15	1.50E+13	1.09E+14	2.17E+12	6.16E+12	2.44E-19
160	9.49E-10	6.05E+02	9.37E+15	1.38E+16	1.06E+15	1.16E+13	1.88E+13	1.09E+12	1.61E+13	1.12E-12
180	3.70E-10	6.48E+02	4.88E+15	4.76E+15	3.34E+14	9.61E+12	4.23E+12	7.31E+11	2.20E+13	1.45E-07
200	1.63E-10	6.70E+02	2.73E+15	1.80E+15	1.15E+14	8.21E+12	1.08E+12	5.94E+11	2.02E+13	1.20E-03
220	7.80E-11	6.82E+02	1.59E+15	7.14E+14	4.11E+13	7.12E+12	2.98E+11	5.32E+11	1.51E+13	1.22E+00
240	3.97E-11	6.88E+02	9.42E+14	2.93E+14	1.51E+13	6.21E+12	8.62E+10	4.98E+11	1.04E+13	2.43E+02
260	2.13E-11	6.92E+02	5.66E+14	1.23E+14	5.66E+12	5.45E+12	2.59E+10	4.75E+11	6.85E+12	1.40E+04
280	1.18E-11	6.94E+02	3.44E+14	5.27E+13	2.16E+12	4.78E+12	8.02E+09	4.57E+11	4.50E+12	3.08E+05
300	6.80E-12	6.95E+02	2.10E+14	2.30E+13	8.42E+11	4.21E+12	2.54E+09	4.41E+11	2.96E+12	3.26E+06
320	4.01E-12	6.96E+02	1.30E+14	1.01E+13	3.33E+11	3.71E+12	8.22E+08	4.27E+11	1.96E+12	1.96E+07
340	2.41E-12	6.96E+02	8.05E+13	4.54E+12	1.33E+11	3.28E+12	2.71E+08	4.13E+11	1.30E+12	7.64E+07
360	1.47E-12	6.96E+02	5.02E+13	2.06E+12	5.42E+10	2.90E+12	9.06E+07	4.00E+11	8.74E+11	2.13E+08
380	9.14E-13	6.96E+02	3.15E+13	9.43E+11	2.23E+10	2.56E+12	3.07E+07	3.87E+11	5.88E+11	4.60E+08
400	5.75E-13	6.96E+02	1.99E+13	4.37E+11	9.29E+09	2.27E+12	1.06E+07	3.75E+11	3.98E+11	8.15E+08
420	3.66E-13	6.96E+02	1.26E+13	2.04E+11	3.91E+09	2.01E+12	3.66E+06	3.64E+11	2.70E+11	1.24E+09
440	2.35E-13	6.96E+02	8.06E+12	9.61E+10	1.66E+09	1.78E+12	1.29E+06	3.53E+11	1.85E+11	1.69E+09
460	1.53E-13	6.96E+02	5.17E+12	4.56E+10	7.13E+08	1.58E+12	4.55E+05	3.42E+11	1.26E+11	2.09E+09
480	1.01E-13	6.96E+02	3.33E+12	2.18E+10	3.09E+08	1.41E+12	1.63E+05	3.32E+11	8.68E+10	2.42E+09
500	6.79E-14	6.96E+02	2.15E+12	1.05E+10	1.35E+08	1.25E+12	5.87E+04	3.22E+11	5.99E+10	2.66E+09

Table A.2: Atmosphere constituents versus altitude for mean solar and geomagnetic activity.

Altitude (km)	Density (kg/m^3)	Temp. (K)	Gas Species Number Densities (m^{-3})							
			n_O	n_{N_2}	n_{O_2}	n_{He}	n_{Ar}	n_H	n_N	$n_{Anom.\ O}$
100	5.73E-07	1.88E+02	5.22E+17	9.60E+18	2.00E+18	1.16E+14	9.71E+16	1.89E+13	3.76E+11	7.28E-37
120	2.03E-08	3.65E+02	9.27E+16	3.36E+17	3.95E+16	3.08E+13	1.49E+15	3.47E+12	1.77E+12	5.52E-27
140	3.44E-09	6.10E+02	2.73E+16	5.38E+16	3.84E+15	1.83E+13	1.26E+14	8.82E+11	9.45E+12	8.98E-19
160	1.20E-09	7.59E+02	1.31E+16	1.72E+16	9.29E+14	1.39E+13	2.64E+13	3.46E+11	2.73E+13	4.12E-12
180	5.46E-10	8.53E+02	7.47E+15	7.08E+15	3.22E+14	1.16E+13	7.67E+12	2.01E+11	4.18E+13	5.33E-07
200	2.84E-10	9.11E+02	4.67E+15	3.27E+15	1.31E+14	1.00E+13	2.61E+12	1.53E+11	4.31E+13	4.43E-03
220	1.61E-10	9.49E+02	3.06E+15	1.62E+15	5.81E+13	8.91E+12	9.73E+11	1.33E+11	3.64E+13	4.48E+00
240	9.60E-11	9.73E+02	2.07E+15	8.36E+14	2.71E+13	8.00E+12	3.84E+11	1.23E+11	2.82E+13	8.94E+02
260	5.97E-11	9.88E+02	1.43E+15	4.44E+14	1.31E+13	7.24E+12	1.58E+11	1.17E+11	2.10E+13	5.14E+04
280	3.83E-11	9.98E+02	9.94E+14	2.40E+14	6.48E+12	6.59E+12	6.69E+10	1.13E+11	1.56E+13	1.14E+06
300	2.52E-11	1.00E+03	7.00E+14	1.32E+14	3.27E+12	6.01E+12	2.90E+10	1.10E+11	1.15E+13	1.20E+07
320	1.69E-11	1.01E+03	4.96E+14	7.35E+13	1.67E+12	5.50E+12	1.28E+10	1.07E+11	8.60E+12	7.22E+07
340	1.16E-11	1.01E+03	3.54E+14	4.13E+13	8.66E+11	5.04E+12	5.75E+09	1.05E+11	6.45E+12	2.81E+08
360	7.99E-12	1.01E+03	2.54E+14	2.35E+13	4.54E+11	4.62E+12	2.61E+09	1.02E+11	4.86E+12	7.85E+08
380	5.60E-12	1.01E+03	1.83E+14	1.34E+13	2.40E+11	4.24E+12	1.20E+09	1.00E+11	3.68E+12	1.69E+09
400	3.96E-12	1.02E+03	1.32E+14	7.74E+12	1.28E+11	3.90E+12	5.61E+08	9.79E+10	2.79E+12	3.00E+09
420	2.83E-12	1.02E+03	9.56E+13	4.50E+12	6.90E+10	3.59E+12	2.64E+08	9.59E+10	2.13E+12	4.57E+09
440	2.03E-12	1.02E+03	6.96E+13	2.63E+12	3.74E+10	3.30E+12	1.25E+08	9.38E+10	1.63E+12	6.21E+09
460	1.47E-12	1.02E+03	5.08E+13	1.55E+12	2.05E+10	3.04E+12	6.00E+07	9.19E+10	1.25E+12	7.70E+09
480	1.07E-12	1.02E+03	3.72E+13	9.15E+11	1.13E+10	2.80E+12	2.90E+07	9.00E+10	9.59E+11	8.92E+09
500	7.85E-13	1.02E+03	2.73E+13	5.44E+11	6.24E+09	2.58E+12	1.41E+07	8.81E+10	7.39E+11	9.81E+09

Table A.3: Atmosphere constituents versus altitude for high solar and geomagnetic activity.

Altitude (km)	Density (kg/m^3)	Temp. (K)	Gas Species Number Densities (m^{-3})							
			n_O	n_{N_2}	n_{O_2}	n_{He}	n_{Ar}	n_H	n_N	$n_{Anom.\ O}$
100	5.64E-07	2.02E+02	5.70E+17	9.71E+18	1.72E+18	1.21E+14	9.73E+16	1.43E+13	5.38E+11	1.57E-36
120	2.22E-08	3.80E+02	1.15E+17	3.72E+17	3.37E+16	3.61E+13	1.62E+15	2.13E+12	3.08E+12	1.36E-26
140	3.93E-09	7.10E+02	3.51E+16	6.07E+16	3.02E+15	2.09E+13	1.43E+14	3.93E+11	1.76E+13	2.12E-18
160	1.54E-09	9.16E+02	1.86E+16	2.17E+16	6.80E+14	1.59E+13	3.51E+13	1.24E+11	5.84E+13	9.74E-12
180	7.87E-10	1.05E+03	1.15E+16	1.00E+16	2.29E+14	1.34E+13	1.21E+13	6.34E+10	1.02E+14	1.26E-06
200	4.57E-10	1.14E+03	7.72E+15	5.24E+15	9.68E+13	1.17E+13	4.91E+12	4.52E+10	1.18E+14	1.05E-02
220	2.86E-10	1.19E+03	5.42E+15	2.93E+15	4.65E+13	1.05E+13	2.18E+12	3.83E+10	1.09E+14	1.06E+01
240	1.87E-10	1.23E+03	3.93E+15	1.71E+15	2.42E+13	9.62E+12	1.03E+12	3.51E+10	9.18E+13	2.11E+03
260	1.27E-10	1.25E+03	2.90E+15	1.03E+15	1.32E+13	8.85E+12	5.02E+11	3.34E+10	7.39E+13	1.22E+05
280	8.87E-11	1.27E+03	2.17E+15	6.30E+14	7.43E+12	8.19E+12	2.52E+11	3.23E+10	5.87E+13	2.68E+06
300	6.31E-11	1.28E+03	1.64E+15	3.91E+14	4.28E+12	7.60E+12	1.30E+11	3.15E+10	4.65E+13	2.84E+07
320	4.56E-11	1.29E+03	1.25E+15	2.46E+14	2.51E+12	7.07E+12	6.77E+10	3.08E+10	3.70E+13	1.71E+08
340	3.34E-11	1.30E+03	9.53E+14	1.56E+14	1.49E+12	6.59E+12	3.59E+10	3.02E+10	2.95E+13	6.65E+08
360	2.47E-11	1.30E+03	7.32E+14	1.00E+14	8.94E+11	6.16E+12	1.93E+10	2.97E+10	2.36E+13	1.85E+09
380	1.85E-11	1.30E+03	5.65E+14	6.44E+13	5.41E+11	5.75E+12	1.05E+10	2.91E+10	1.90E+13	4.00E+09
400	1.40E-11	1.30E+03	4.37E+14	4.18E+13	3.30E+11	5.38E+12	5.75E+09	2.86E+10	1.54E+13	7.10E+09
420	1.06E-11	1.30E+03	3.39E+14	2.73E+13	2.03E+11	5.04E+12	3.18E+09	2.82E+10	1.24E+13	1.08E+10
440	8.13E-12	1.31E+03	2.64E+14	1.79E+13	1.26E+11	4.72E+12	1.78E+09	2.77E+10	1.01E+13	1.47E+10
460	6.26E-12	1.31E+03	2.06E+14	1.18E+13	7.84E+10	4.42E+12	1.00E+09	2.72E+10	8.21E+12	1.82E+10
480	4.84E-12	1.31E+03	1.62E+14	7.85E+12	4.91E+10	4.14E+12	5.66E+08	2.68E+10	6.69E+12	2.11E+10
500	3.76E-12	1.31E+03	1.27E+14	5.23E+12	3.10E+10	3.89E+12	3.23E+08	2.64E+10	5.47E+12	2.32E+10

APPENDIX B

Ferrite Material Data

Two types of ferrite materials were used in the EMI mitigation scheme at PEPL:

Ferrite 1: TDK part # ZCAT3035-1330s Ferrite 2: API Delevan part # BF2390

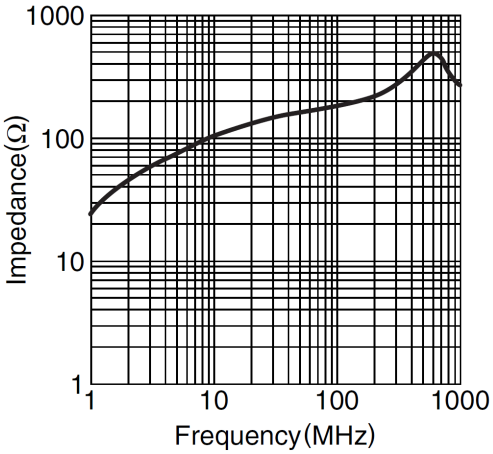

Figure B.1: TDK ZCAT 3035-1330s ferrite material characteristics.

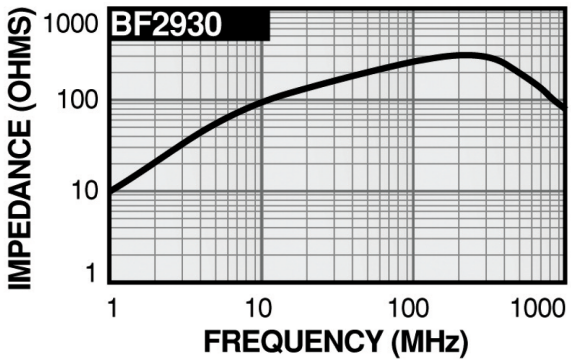

Figure B.2: API Delevan BF2390 ferrite material characteristics.

BIBLIOGRAPHY

[1] Futron Corporation, "State of the Satellite Industry Report – May 2012," Satellite Industry Association, 1200 18th, NW, Suite 1001, Washington, DC, 20036, Retrieved July 17, 2012 from http://www.sia.org/wp-content/uploads/2012/06/Final-2012-State-of-Satellite-Industry-Report.pdf. 1

[2] Swartwout, M., "A statistical survey of rideshares (and attack of the CubeSats, part deux)," *IEEE Aerospace Conference*, Big Sky, MT, March 2012. doi: 10.1109/AERO.2012.6187008. 1

[3] Sanders, G. B., "ISRU: An Overview of NASA's Current Development Activities and Long-Term Goals," *38th AIAA Aerospace Sciences Meeting & Exhibit*, AIAA-2000-1062, Reno, NV, January 2000. 2

[4] Larson, W. E., Sanders, G. B., and Sacksteder, K. R., "NASA's In-Situ Resource Utilization Project: Current Accomplishments and Exciting Future Plans," *AIAA SPACE 2010 Conference & Exhibit*, AIAA-2010-8603, Anaheim, CA, August – September 2010. 2

[5] Demetriades, S. T., "A Novel System for Space Flight Using a Propulsive Fluid Acculumator," *Journal of the British Interplanetary Society*, Vol. 17, Sept. 1959, pp. 114–119. 2, 6, 7

[6] Wertz, J. R. and Larson, W. J., editors, *Space Mission Analysis and Design*, Microcosm Press and Springer, Hawthorne, CA and New York, NY, 3rd ed., 1999. 2, 3, 4, 5, 29, 33

[7] "Space Exploration Technologies Corporation - Falcon 9," Retrieved November 10, 2012 from http://www.spacex.com/falcon9.php. 3

[8] "Pegasus® User's Guide Release 7.0," Orbital Sciences Corporation, April 2010, Retrieved July 17, 2012 from http://www.orbital.com/NewsInfo/Publications/Pegasus_UG.pdf. 3, 34, 35

[9] van Belle, G. T., Meinel, A. B., and Meinel, M. P., "The scaling relationship between telescope cost and aperture size for very large telescopes," *Proceedings of the SPIE*, Vol. 5489, September 2004, pp. 563 – 570, doi: 10.1117/12.552181. 3

[10] Fujita, K. and Noda, A., "Rarefied Aerodynamics of a Super Low Altitude Test Satellite," *41st AIAA Thermophysics Conference*, AIAA-2009-3606, San Antonio, TX, 22–25 June 2009. 3

[11] "Research and development of an ion engine for a super-low-altitude satellite," *Sora to Sora*, No. 42, Japan Aerospace Exploration Agency – Aerospace Research and Development Directorate, 2011, Retrieved July 17, 2012 from http://www.ard.jaxa.jp/eng/publication/sorasora/2011_no42/ss2011no42_02.html. 3

[12] Kruger, J. K., *CLOSeSat: Perigee-Lowering Techniques and Preliminary Design for a Small Optical Imaging Satellite Operating in Very Low Earth Orbit*, Master's thesis, Aeronautics and Astronautics, Massachusetts Institute of Technology, Cambridge, MA, 2010. 4

[13] Liou, J.-C., Johnson, N., and Hill, N., "Controlling the growth of future LEO debris populations with active debris removal," *Acta Astronautica*, Vol. 66, No. 5-6, 2010, pp. 648 – 653, doi: 10.1016/j.actaastro.2009.08.005. 4, 5

[14] Liou, J.-C., "An active debris removal parametric study for LEO environment remediation," *Advances in Space Research*, Vol. 47, No. 11, 2011, pp. 1865 – 1876, doi: 10.1016/j.asr.2011.02.003. 4

[15] Goetzberger, A., Luther, J., and Willeke, G., "Solar cells: past, present, future," *Solar Energy Materials and Solar Cells*, Vol. 74, No. 1-4, 2002, pp. 1–11, doi: 10.1016/S0927-0248(02)00042-9. 6

[16] Pedersen, E. S., *Nuclear Energy in Space*, Prentice-Hall, Englewood Cliffs, NJ, 1964, pp. 7–12. 6

[17] Berner, F. and Camac, M., "Air scooping vehicle," *Planetary and Space Science*, Vol. 4, 1961, pp. 159 – 183, doi: 10.1016/0032-0633(61)90130-1. 6, 7, 8, 42

[18] Dolgich, A., "Soviet studies on low-thrust orbital propellant-scooping systems," *Foreign Science Bulletin*, Vol. 5, No. 7, July 1969, pp. 1–9, Retrieved July 17, 2012 from http://www.dtic.mil/dtic/tr/fulltext/u2/690999.pdf. 6, 8

[19] Zukerman, A. and Kretschmer, C., "A study of the feasibility of an atomic oxygen ramjet," *Planetary and Space Science*, Vol. 4, Jan. 1961, pp. 60–76, doi: 10.1016/0032-0633(61)90123-4. 8, 17, 25

[20] Justus, C. G., Duvall, A., Keller, V. W., Spilker, T. R., and Lockwood, M. K., "Connecting atmospheric science and atmospheric models for aerocapture at Titan and the outer planets," *Planetary and Space Science*, Vol. 53, No. 5, 2005, pp. 601–605, doi: 10.1016/j.pss.2004.12.002. 9

[21] Bussard, R. W., "Galactic Matter and Interstellar Flight," *Astronautica Acta*, Vol. 6, No. 4, Feb. 1960, pp. 1–14, Retrieved July 17, 2012 from http://www.askmar.com/Robert%20Bussard/Galactic%20Matter%20and%20Interstellar%20Flight.pdf. 9

[22] Anderson, P., *Tau Zero*, Doubleday, Garden City, NY, 1st ed., 1970. 9

[23] Palaszewski, B., "Atmospheric Mining in the Outer Solar System," *41st AIAA/ASME/SAE/ASEE Joint Propulsion Conference & Exhibit*, AIAA-2005-4319, Tucson, AZ, 10–13 July 2005. 9

[24] Minovitch, M. A., "Solar Powered, Self-Refueling, Microwave Propelled Interorbital Transportation System," *18th AIAA Thermophysics Conference*, AIAA-83-1446, Montreal, Canada, June 1983. 10

[25] Lamamy, J.-A., *Enhancing the science return of Mars missions via sample preparation, robotic surface exploration, and in orbit fuel production*, Master's thesis, Aeronautics and Astronautics, Massachusetts Institute of Technology, Cambridge, MA, 2004. 10

[26] Fujita, K., "Air Intake Performance of Air Breathing Ion Engines," *Journal of the Japan Society for Aeronautical and Space Sciences*, Vol. 52, No. 610, 2004, pp. 514–521. 11

[27] DiCara, D., Gonzalez del Amo, J., Santovincenzo, A., Dominguez, B. C., Arcioni, M., Caldwell, A., and Roma, I., "RAM Electric Propulsion for Low Earth Orbit Operation: an ESA study." *30th International Electric Propulsion Conference*, IEPC-2007-162, Florence, Italy, September 2007. 11, 13

[28] Kirtley, D., Slough, J., Pihl, C., Meier, E., and Milroy, R., "Pulsed Plasmoid Propulsion: Air-Breathing Electromagnetic Propulsion," *32nd International Electric Propulsion Conference*, IEPC-2011-015, Wiesbaden, Germany, September 2011. 11, 13

[29] Hisamoto, Y., Nishiyama, K., and Kuninaka, H., "Development Statue of Atomic Oxygen Simulator for Air Breathing Ion Engine," *32nd International Electric Propulsion Conference*, IEPC-2011-294, Wiesbaden, Germany, September 2011. 11, 12

[30] Pigeon, T. D. and Whitaker, R. B., "Analysis of a Near-Vacuum Hall Thruster," *42nd AIAA Aerospace Sciences Meeting and Exhibit*, AIAA-2004-127, Reno, NV, January 2004. 11

[31] Bashir, O. S. and Sullivan, R. M., "Near-Vacuum Hall Thruster for Drag Compensation," Massachusetts Institute of Technology, 16.622 Final Report, December 7, 2004. 11

[32] Dressler, G. A., "Spacecraft Propulsive Device Using Ambient Upper Atmospheric Constituents for Reaction Mass," *42nd AIAA/ASME/SAE/ASEE Joint Propulsion Conference & Exhibit*, AIAA-2006-4650, Sacramento, CA, July 2006. 11

[33] Pekker, L. and Keidar, M., "Analysis of Air Breathing Hall Effect Thruster," *42nd AIAA Plasmadynamics and Lasers Conference*, AIAA-2011-3737, Honolulu, HI, June 2011. 11, 12

[34] Nishiyama, K., "Air Breathing Ion Engine," *24th International Symposium on Space Technology and Science*, ISTS 2004-o-3-05v, Miyazaki City, Japan, May–June 2004. 12

[35] Tagawa, M., Nishiyama, K., Yokota, K., Yoshizawa, Y., Yamamoto, D., and Kuninaka, H., "An Experimental Study on Air Breathing Ion Engine Concept Using Laser-Detonation Atomic Oxygen Beam Source as an LEO Space Environment Simulator," *27th International Symposium on Space Technology and Science*, ISTS 2009-b-04, Tsukuba City, Japan, July 2009. 12

[36] Jones, C., Masse, D., Glass, C., Wilhite, A., and Walker, M., "PHARO – Propellant Harvesting of Atmospheric Resources in Orbit," *IEEE Aerospace Conference*, Big Sky, MT, March 2010. doi: 10.1109/AERO.2010.5447034. 13

[37] Diamant, K. D., "A 2-Stage Cylindrical Hall Thruster for Air Breathing Electric Propulsion," *46th AIAA/ASME/SAE/ASEE Joint Propulsion Conference & Exhibit*, AIAA-2010-6522, Nashville, TN, July 2010. 13

[38] Kirtley, D., Pancotti, A., Slough, J., and Pihl, C., "Steady Operation of an FRC Thruster on Martian Atmosphere and Liquid Water Propellants," *48th AIAA/ASME/SAE/ASEE Joint Propulsion Conference & Exhibit*, AIAA-2012-4071, Atlanta, GA, July – August 2012. 13

[39] Hruby, V., Pote, B., Brogan, T., Hohman, K., Szabo, J., and Rostler, P., "Air Breathing Electrically Powered Hall Effect Thruster," U.S. Patent 6,834,492 B2, December 28, 2004, Assigned to Busek Company, Inc. 14

[40] Wahl, E. L., "Air-Breathing Electrostatic Ion Thruster," U.S. Patent 7,581,380 B2, September 1, 2009. 14

[41] Hedin, A. E., "Extension of the MSIS Thermospheric Model into the Middle and Lower Atmosphere," *Journal of Geophysical Research*, Vol. 96, No. A2, Feb. 1991, pp. 1159–1172, Accessed from http://omniweb.gsfc.nasa.gov/vitmo/msis_vitmo.html, doi: 10.1029/90JA02125. 16

[42] ISO/DIS 14222, *Space environment (natural and artificial) – Earth upper atmosphere*, ISO, Geneva, Switzerland. Accessed from http://www.spacewx.com/Docs/ISO_DIS_14222_E.pdf. 16, 17, 31, 148

[43] Vincenti, W. G. and Kruger, Jr., C. H., *Introduction to Physical Gas Dynamics*, Krieger, Malabar, FL, 1965 [Reprint 2002]. 17

[44] Choueiri, E. Y., "A Critical History of Electric Propulsion: The First 50 Years (1906–1956)," *Journal of Propulsion and Power*, Vol. 20, No. 2, Mar.-Apr. 2004, pp. 193–203, doi: 10.2514/1.9245. 22

[45] Sutton, G. P. and Biblarz, O., *Rocket Propulsion Elements*, John Wiley & Sons, New York, 7th ed., 2001. 24, 27

[46] Arbit, H. A., Clapp, S. D., and Nagai, C. K., "Investigation of the lithium-fluorine-hydrogen tripropellant system," *Journal of Spacecraft and Rockets*, Vol. 7, No. 10, 1970, pp. 1221–1227, doi: 10.2514/3.30138. 24

[47] Mead Jr, F., "Advanced Propulsion Concepts - Project Outgrowth," Tech. rep., DTIC Document AFRPL-TR-72-31, 1972. 24

[48] Martinez-Sanchez, M. and Pollard, J. E., "Spacecraft Electric Propulsion–An Overview," *Journal of Propulsion and Power*, Vol. 14, No. 5, Sept. 1998, pp. 688–699, doi: 10.2514/2.5331. 27

[49] Foster, J. E., Haag, T., Kamhawi, H., Patterson, M., Malone, S., Elliot, F., George J. Williams, Jr., G. J., Sovey, J. S., and Carpenter, C., "The High Power Electric Propulsion (HiPEP) Ion Thruster," *40th AIAA/ASME/SAE/ASEE Joint Propulsion Conference & Exhibit*, AIAA-2004-3812, Fort Lauderdale, FL, July 2004. 27

[50] Soulas, G. C., Haag, T. W., Herman, D. A., Huang, W., Kamhawi, H., and Shastry, R., "Performance Test Results of the NASA-457M v2 Hall Thruster," *48th AIAA/ASME/SAE/ASEE Joint Propulsion Conference & Exhibit*, AIAA-2012-3940, Atlanta, GA, July–August 2012. 27

[51] Linnell, J. A., *An Evaluation of Krypton Propellant in Hall Thrusters*, Ph.D. thesis, Aerospace Engineering, University of Michigan, Ann Arbor, MI, 2007. 27, 46, 138, 139

[52] Curran, F. M. and Byers, D. C., "New Developments and Research Findings: NASA Hydrazine Arcjets," *25th AIAA Plasmadynamics and Lasers Conference*, AIAA-84-2463, Colorado Springs, CO, June 1994. 27

[53] Mathers, A. J., Aadland, R. S., Manzella, D., and Kamhawi, H., "Development Status of the HiVHAC Hall Thruster," *44th AIAA/ASME/SAE/ASEE Joint Propulsion Conference & Exhibit*, AIAA-2008-4524, Hartford, CT, July 2008. 27

[54] Mikellides, I. G., Katz, I., Hofer, R. R., Goebel, D. M., de Grys, K., and Mathers, A., "Magnetic shielding of the channel walls in a Hall plasma accelerator," *Physics of Plasmas*, Vol. 18, No. 3, 2011, pp. 033501–1–18, doi: 10.1063/1.3551583. 27, 46, 82

[55] Hofer, R. R., Goebel, D. M., Mikellides, I. G., and Katz, I., "Design of a Laboratory Hall Thruster with Magnetically Shielded Channel Walls, Phase II: Experiments," *48th AIAA/ASME/SAE/ASEE Joint Propulsion Conference & Exhibit*, AIAA-2012-3788, Atlanta, GA, July – August 2012. 27, 82

[56] Cifali, G., Misuri, T., Rossetti, P., Andrenucci, M., Valentian, D., and Feili, D., "Preliminary characterization test of HET and RIT with Nitrogen and Oxygen," *47th AIAA/ASME/SAE/ASEE Joint Propulsion Conference & Exhibit*, AIAA-2011-6073, San Diego, CA, July – August 2011. 28, 45

[57] Wallace, N., Jameson, P., Saunders, C., Fehringer, M., Edwards, C., and Floberghagen, R., "The GOCE Ion Propulsion Assembly – Lessons Learnt from the First 22 Months of Flight Operations," *32nd International Electric Propulsion Conference*, IEPC-2011-327, Wiesbaden, Germany, September 2011. 28

[58] Haynes, W. M., editor, *CRC Handbook of Chemistry and Physics*, CRC Press/Taylor and Francis, Boca Raton, FL, 92nd ed., (Internet Version 2012). 31

[59] Sutton, E. K., "Normalized Force Coefficients for Satellites with Elongated Shapes," *Journal of Spacecraft and Rockets*, Vol. 46, No. 1, Jan.-Feb. 2009, pp. 112–116, doi: 10.2514/1.40940. 32

[60] "29.5% NeXt Triple Junction (XTJ) Solar Cells," Spectrolab, Inc., September 2012, Retrieved December 12, 2012 from http://www.spectrolab.com/DataSheets/cells/PV%20XTJ%20Cell%205-20-10.pdf. 34

[61] "Space Solar Panels," Spectrolab, Inc., May 2010, Retrieved December 12, 2012 from http://www.spectrolab.com/DataSheets/Panel/panels.pdf. 34, 36

[62] "ESA - Living Planet Programme - GOCE - GOCE satellite," Retrieved July 17, 2012 from http://www.esa.int/esaLP/ESA1MK1VMOC_LPgoce_0.html. 35

[63] Shastry, R., Herman, D. A., Soulas, G. C., and Patterson, M. J., "NASAs Evolutionary Xenon Thruster (NEXT) Long-Duration Test as of 736 kg of Propellant Throughput," *48th AIAA/ASME/SAE/ASEE Joint Propulsion Conference & Exhibit*, AIAA-2012-4023, Atlanta, GA, July – August 2012. 44

[64] Gallagher, H. E., "Poisoning of LaB_6 Cathodes," *Journal of Applied Physics*, Vol. 40, No. 1, Jan. 1969, pp. 44–51, doi: 10.1063/1.1657092. 45

[65] Goebel, D. M. and Katz, I., *Fundamentals of Electric Propulsion: Ion and Hall Thrusters*, chap. 4, John Wiley & Sons, New York, 2007, pp. 148–171. 45

[66] Killinger, R., Kukies, R., Surauer, M., Tomasetto, A., and van Holtz, L., "ARTEMIS Orbit Raising Inflight Experience with Ion Propulsion," *Acta Astronautica*, Vol. 53, No. 4–10, 2003, pp. 607–621, doi: 10.1016/S0094-5765(03)80022-X. 45

[67] Kuninaka, H., Nishiyama, K., Funaki, I., Yamada, T., Shimizu, Y., and Kawaguchi, J., "Powered Flight of Electron Cyclotron Resonance Ion Engines on Hayabusa Explorer," *Journal of Propulsion and Power*, Vol. 23, No. 3, May-Jun. 2007, pp. 544–551, doi: 10.2514/1.25434. 45, 46

[68] Jahn, R. G., *Physics of Electric Propulsion*, chap. 6, McGraw-Hill, New York, 1st ed., 1968, pp. 133–139. 45

[69] Longmier, B. W., Cassady, L. D., Ballenger, M. G., Carter, M. D., Chang-Daz, F. R., Glover, T. W., Ilin, A. V., McCaskill, G. E., Olsen, C. S., and Squire, J. P., "VX-200 Magnetoplasma Thruster Performance Results Exceeding Fifty-Percent Thruster Efficiency," *Journal of Propulsion and Power*, Vol. 27, No. 4, Jul.-Aug. 2011, pp. 915–920, doi: 10.2514/1.54932. 45, 74, 126

[70] Williams, L. T. and Walker, M. L. R., "Thrust Measurements of a Helicon Plasma Source," *47th AIAA/ASME/SAE/ASEE Joint Propulsion Conference & Exhibit*, AIAA-2011-5893, San Diego, CA, July – August 2011. 45, 46, 80, 114

[71] Pottinger, S., Lappas, V., Charles, C., and Boswell, R., "Performance characterization of a double layer thruster using direct thrust measurements," *Journal of Applied Physics D: Applied Physics*, Vol. 44, No. 23, June 2011, pp. 235201–1–5, doi: 10.1088/0022-3727/44/23/235201. 45, 46, 74, 80, 114

[72] Motomura, T., Ohno, E., Katanami, H., Sakei, Y., Yasutake, T., Mori, J., Shinohara, S., and Hada, T., "Novel Electromagnetic Propulsion System Using High-Density Helicon Plasma," *52nd Annual Meeting of the APS Division of Plasma Physics*, Chicago, IL, Retrieved from http://meetings.aps.org/link/BAPS.2010.DPP.TP9.55, November 2011. 45

[73] Pavarin, D., Ferri, F., Manente, M., Curreli, D., Güçlü, Y., Melazzi, D., Rondini, D., Suman, S., Carlsson, J., Bramanti, C., Ahedo, E., Lancellotti, V., Katsonis, K., and Markelov, G., "Design of a 50 W Helicon Plasma Thruster," *31st International Electric Propulsion Conference*, IEPC-2009-205, Ann Arbor, MI, September 2009. 45, 74

[74] Winglee, R., Ziemba, T., Giersch, L., Prager, J., Carscadden, J., and Roberson, B. R., "Simulation and laboratory validation of magnetic nozzle effects for the high power helicon thruster," *Physics of Plasmas*, Vol. 14, No. 6, June 2007, pp. 063501–1–14, doi: 10.1063/1.2734184. 45

[75] Wiebold, M., Sung, Y., and Scharer, J. E., "Experimental observation of ion beams in the Madison Helicon eXperiment," *Physics of Plasmas*, Vol. 18, No. 6, June 2011, pp. 063501, doi: 10.1063/1.3596537. 45, 74, 114, 124

[76] Huang, W., *Study of Hall Thruster Discharge Channel Wall Erosion via Optical Diagnostics*, Ph.D. thesis, Aerospace Engineering, University of Michigan, Ann Arbor, MI, 2011. 45

[77] Brown, D. L., *Investigation of Low Discharge Voltage Hall Thruster Characteristics and Evaluation of Loss Mechanisms*, Ph.D. thesis, Aerospace Engineering, University of Michigan, Ann Arbor, MI, 2009. 46, 98, 99, 102

[78] Gottlieb, I. M., *Practical RF Power Design Techniques*, TAB Books, Blue Ridge Summit, PA, 1st ed., 1993. 48

[79] "Terms and Definitions," *Electronic Code of Federal Regulations* Title 47, Pt. 2.1, Retrieved December 11, 2012 from http://www.ecfr.gov/. 49

[80] "Assignment of frequencies," *Electronic Code of Federal Regulations* Title 47, Pt. 2.102, Retrieved December 11, 2012 from http://www.ecfr.gov/. 49

[81] Kaiser, K. L., *Transmission Lines, Matching, and Crosstalk*, CRC Press, Taylor & Francis Group, Boca Raton, FL, 2006. 50, 56

[82] Ulaby, F. T., *Fundamentals of Applied Electromagnetics*, Pearson Prentice Hall, Upper Saddle River, NJ, 5th ed., 2007. 54, 59

[83] Kieckhafer, A. W. and Walker, M. L. R., "RF Power System for Thrust Measurements of a Helicon Plasma Source," *Review of Scientific Instruments*, Vol. 81, No. 7, July 2010, pp. 075106, doi: 10.1063/1.3460263. 56

[84] Chen, F. F., "Experiments on helicon plasma sources," *Journal of Vacuum Science & Technology A: Vacuum, Surfaces, and Films*, Vol. 10, No. 4, Jul.-Aug. 1998, pp. 1389–1401, doi: 10.1116/1.578256. 70, 78

[85] Gerwin, R. A., "Integrity of the Plasma Magnetic Nozzle," NASA/TP–2009-213439, NASA Glenn Research Center, Cleveland, OH, 2009. 70, 75

[86] Ebersohn, F. H., Girimaji, S. S., Staak, D., Shebalin, J. V., Longmier, B., and Olsen, C., "Magnetic Nozzle Plasma Plume: Review of Crutial Physical Phenomena," *48th AIAA/ASME/SAE/ASEE Joint Propulsion Conference & Exhibit*, AIAA-2012-4274, Atlanta, GA, July–August 2010. 70, 75

[87] Deline, C. A., *Characterization of the Magnetic Nozzle Region of High Powered Electric Propulsion Thrusters Using Numerical Simulation, RF Interferometry and Electrostatic Probes*, Ph.D. thesis, Electrical Engineering, University of Michigan, Ann Arbor, MI, 2008. 70, 75

[88] Lieberman, M. A. and Lichtenberg, A. J., *Principles of Plasma Discharges and Materials Processing*, John Wiley & Sons, Hoboken, 2nd ed., 2005. 71, 113

[89] Stix, T. H., *Waves in Plasmas*, American Institute of Physics, New York, 1992. 72

[90] Chen, F. F., "Plasma ionization by helicon waves," *Plasma Physics and Controlled Fusion*, Vol. 33, No. 4, 1991, pp. 339–364, doi: 10.1088/0741-3335/33/4/006. 72

[91] Blackwell, D. D., Madziwa, T. G., Arnush, D., and Chen, F. F., "Evidence for Trivelpiece-Gould Modes in a Helicon Discharge," *Physical Review Letters*, Vol. 88, No. 14, March 2002, pp. 145002–1–4, doi: 10.1103/PhysRevLett.88.145002. 73

[92] Boswell, R. W. and Chen, F. F., "Helicons – The Early Years," *IEEE Transactions on Plasma Science*, Vol. 25, No. 6, Dec. 1997, pp. 1229–1244, doi: 10.1109/27.650898. 73

[93] Chen, F. F. and Boswell, R. W., "Helicons – The Past Decade," *IEEE Transactions on Plasma Science*, Vol. 25, No. 6, Dec. 1997, pp. 1245–1257, doi: 10.1109/27.650899. 73

[94] Palmer, D. D. and Walker, M. L. R., "Operation of an Annular Helicon Plasma Source," *Journal of Propulsion and Power*, Vol. 25, No. 5, Sep.-Oct. 2009, pp. 1013–1019, doi: 10.2514/1.41403. 73

[95] Yano, M. and Wallker, M. L. R., "Plasma ionization by annularly bounded helicon waves," *Physics of Plasmas*, Vol. 13, No. 6, June 2006, pp. 063501–1–5, doi: 10.1063/1.2207125. 73

[96] Shabshelowitz, A. and Gallimore, A. D., "Divergence Angle of Ion Beams Emanating from an Immersed Radiofrequency Plasma Source," *32nd International Electric Propulsion Conference*, IEPC-2011-166, Wiesbaden, Germany, September 2011. 74, 81

[97] Palmer, D., Walker, M. L. R., Manente, M., Carlsson, J., Bramanti, C., and Pavarin, D., "Performance Analysis of a Low-Power Helicon Thruster," *44th AIAA/ASME/SAE/ASEE Joint Propulsion Conference & Exhibit*, AIAA-2008-4925, Hartford, CT, July 2008. 74

[98] Nakamura, T., Yokoi, K., Nishida, H., Shinohara, S., Funaki, I., Matsuoka, T., Tanikawa, T., Hada, T., Shamrai, K. P., and Rudenko, T. S., "Experimental Investigation of Plasma Acceleration by Rotating Electric Field for Electrodeless Plasma Thruster," *32nd International Electric Propulsion Conference*, IEPC-2011-279, Wiesbaden, Germany, September 2011. 74

[99] Slough, J., Kirtley, D., and Weber, T., "Pulsed Plasmoid Propulsion: The ELF Thruster," *31st International Electric Propulsion Conference*, IEPC-2009-265, Ann Arbor, MI, September 2009. 74

[100] Charles, C. and Boswell, R. W., "Laboratory evidence of a supersonic ion beam generated by a current-free "helicon" double-layer," *Physics of Plasmas*, Vol. 11, No. 4, 2004, pp. 1706–1714, doi: 10.1063/1.1652058. 74, 124

[101] Cohen, S. A., Siefert, N. S., Stange, S., Boivin, R. F., Scime, E. E., and Levinton, F. M., "Ion acceleration in plasmas emerging from a helicon-heated magnetic-mirror device," *Physics of Plasmas*, Vol. 10, No. 6, 2003, pp. 2593–2598, doi: 10.1063/1.1568342. 74

[102] Batishchev, O., "Minihelicon Plasma Thruster," *IEEE Transactions on Plasma Science*, Vol. 37, No. 8, Aug. 2009, pp. 1563–1571, doi: 10.1109/TPS.2009.2023990. 75

[103] Boswell, R. W., "Very efficient plasma generation by whistler waves near the lower hybrid frequency," *Plasma Physics and Controlled Fusion*, Vol. 26, No. 10, Oct. 1984, pp. 1147–1162, doi: 10.1088/0741-3335/26/10/001. 75

[104] Tysk, S. M., Denning, C. M., Scharer, J. E., and Akhtar, K., "Optical, wave measurements, and modeling of helicon plasmas for a wide range of magnetic fields," *Physics of Plasmas*, Vol. 11, No. 3, March 2004, pp. 878–887, doi: 10.1063/1.1642656. 75

[105] Ellingboe, A. R. and Boswell, R. W., "Capacitive, inductive and helicon-wave modes of operation of a helicon plasma source," *Physics of Plasmas*, Vol. 3, No. 7, 1996, pp. 2797 – 2804, doi: 10.1063/1.871713. 76

[106] Kramida, A., Ralchenko, Y., Reader, J., and NIST ASD Team (2012), *NIST Atomic Spectra Database* ver. 5.0, [Online], National Institute of Standards and Technology, Gaithersburg, MD. Retrieved December 18, 2012 from http://physics.nist.gov/asd. 76

[107] Pearse, R. W. B. and Gaydon, A. G., *The Identification of Molecular Spectra*, Chapman and Hall, New York, 4th ed., 1976. 77

[108] Carroll, P. K. and Sayers, N. D., "The Band Spectrum of Nitrogen: New Studies of the Triplet Systems," *Proceedings of the Physical Society. Section A*, Vol. 66, No. 12, 1953, pp. 1138, doi: 10.1088/0370-1298/66/12/309. 77

[109] Jamroz, P. and Zyrnicki, W., "Optical emission spectroscopy study for nitrogen-acetylene-argon and nitrogen-acetylene-helium 100 kHz and dc discharges," *Vacuum*, Vol. 84, No. 7, 2010, pp. 940 – 946, doi: 10.1016/j.vacuum.2009.12.019. 77

[110] Suraj, K. S., Bharathi, P., Prahlad, V., and Mukherjee, S., "Near cathode optical emission spectroscopy in N_2-H_2 glow discharge plasma," *Surface and Coatings Technology*, Vol. 202, No. 2, 2007, pp. 301 – 309, doi: 10.1016/j.surfcoat.2007.05.063. 77

[111] Xu, N., Du, Y., Ying, Z., Ren, Z., and Li, F., "An arc discharge nitrogen atom source," *Review of Scientific Instruments*, Vol. 68, No. 8, 1997, pp. 2994 – 3000, doi: 10.1063/1.1148232. 77

[112] Takahashi, K., Lafleur, T., Charles, C., Alexander, P., and Boswell, R. W., "Electron Diamagnetic Effect on Axial Force in an Expanding Plasma: Experiments and Theory," *Physical Review Letters*, Vol. 107, Nov. 2011, pp. 235001–1–4, doi: 10.1103/PhysRevLett.107.235001. 80, 131

[113] Kamenski, I. V. and Borg, G. G., "An evaluation of different antenna designs for helicon wave excitation in a cylindrical plasma source," *Physics of Plasmas*, Vol. 3, No. 12, 1996, pp. 4396–4409, doi: 10.1063/1.872057. 81

[114] Hofer, R. R., *Development and Characterization of a High-Efficiency, High-Specific Impulse Xenon Hall Thruster*, Ph.D. thesis, Aerospace Engineering, University of Michigan, Ann Arbor, MI, 2004. 82, 99, 100, 102, 128, 133

[115] Makela, J. M., Washeleski, R. L., Massey, D. R., King, L. B., and Hopkins, M. A., "Development of a Magnesium and Zinc Hall-Effect Thruster," *Journal of Propulsion and Power*, Vol. 26, No. 5, Sep.-Oct. 2010, pp. 1029–1035, doi: 10.2514/1.47410. 82

[116] Szabo, J., Robin, M., Duggan, J., and Hofer, R. R., "Light Metal Propellant Hall Thrusters," *31st International Electric Propulsion Conference*, IEPC-2009-138, Ann Arbor, MI, September 2009. 82

[117] Liang, R. and Gallimore, A. D., "Constant-Power Performance and Plume Properties of a Nested-Channel Hall-Effect Thruster," *32nd International Electric Propulsion Conference*, IEPC-2011-030, Wiesbaden, Germany, September 2011. 82, 100

[118] Florenz, R., Gallimore, A. D., and Peterson, P. Y., "Developmental Status of a 100-kW Class Laboratory Nested Channel Hall Thruster," *32nd International Electric Propulsion Conference*, IEPC-2011-246, Wiesbaden, Germany, September 2011. 82

[119] Martinez, R. A., Hoskins, W. A., Peterson, P. Y., and Massey, D. R., "Development Status of the Helicon Hall Thruster," *31st International Electric Propulsion Conference*, IEPC-2009-120, Ann Arbor, MI, September 2009. 82, 84

[120] Kamhawi, H., Manzella, D., Pinero, L., Haag, T., Mathers, A., and Liles, H., "In-Space Propulsion High Voltage Hall Accelerator Development Project Overview," *45th AIAA/ASME/SAE/ASEE Joint Propulsion Conference & Exhibit*, AIAA-2010-5282, Denver, CO, August 2009. 82

[121] Beal, B. E., Gallimore, A. D., Morris, D. P., Davis, C., and Lemmer, K. M., "Development of an Annular Helicon Source for Electric Propulsion Applications," *42nd AIAA/ASME/SAE/ASEE Joint Propulsion Conference & Exhibit*, AIAA-2006-4841, Atlanta, GA, July 2006. 83

[122] Peterson, P. Y., Massey, D. R., Shabshelowitz, A., Shastry, R., and Liang, R., "Performance and Plume Characterization of a Helicon Hall Thruster," *32nd International Electric Propulsion Conference*, IEPC-2011-269, Wiesbaden, Germany, September 2011. 84

[123] Wilson, M. J., editor, *The ARRL Handbook For Radio Communications*, ARRL - the national association for Amateur Radio, Newington, CT, 86th ed., 2008. 89, 93, 109

[124] Garvin, C., Grimard, D., Grizzle, J., and Gilchrist, B. E., "Measurement and error evaluation of electrical parameters at plasma relevant frequencies and impedances," *Journal of Vacuum Science & Technology A: Vacuum, Surfaces, and Films*, Vol. 16, No. 2, Mar.-Apr. 1998, pp. 595–606, doi: 10.1116/1.581098. 93

[125] Haag, T. W., "Thrust stand for high-power electric propulsion devices," *Review of Scientific Instruments*, Vol. 62, No. 5, 1991, pp. 1186 – 1191, doi: 10.1063/1.1141998. 94

[126] Xu, K. and Walker, M. L. R., "High-Power, Null-Type, Inverted Pendulum Thrust Stand," *Review of Scientific Instruments*, Vol. 80, No. 5, May 2009, pp. 055103–1–6, doi: 10.1063/1.3125626. 95

[127] Liang, R. and Gallimore, A. D., "Far-Field Plume Measurements of a Nested-Channel Hall-Effect Thruster," *49th AIAA Aerospace Sciences Meeting*, AIAA-2011-1016, Orlando, FL, January 2011. 98

[128] Brown, D. L. and Gallimore, A. D., "Evaluation of ion collection area in Faraday probes," *Review of Scientific Instruments*, Vol. 81, No. 6, June 2010, pp. 063504–1–11, doi: 10.1063/1.3449541. 99

[129] Lemmer, K. M., *Use of a Helicon Source for Development of a Re-Entry Blackout Amelioration System*, Ph.D. thesis, Aerospace Engineering, University of Michigan, Ann Arbor, MI, 2009. 100, 101, 103, 113

[130] Hutchinson, I. H., *Principles of Plasma Diagnostics*, Cambridge University Press, New York, NY, 2002. 100, 113

[131] Shastry, R., *Experimental Characterization of the Near-Wall Region in Hall Thrusters and its Implications on Performance and Lifetime*, Ph.D. thesis, Aerospace Engineering, University of Michigan, Ann Arbor, MI, 2010. 103

[132] Anderson, J. D., *Fundamentals of Aerodynamics*, chap. 10, McGraw-Hill, New York, 3rd ed., 2001, pp. 566–567. 109

[133] Foster, J. E., "Intercusp Electron Transport in an NSTAR-Derivative Ion Thruster," *Journal of Propulsion and Power*, Vol. 18, No. 1, Jan. 2002, pp. 213–217, doi: 10.2514/2.5922. 113

[134] Demidov, V. I., Ratynskaia, S. V., and Rypdal, K., "Electric probes for plasmas: The link between theory and instrument," *Review of Scientific Instruments*, Vol. 73, No. 10, 2002, pp. 3409–3439, doi: 10.1063/1.1505099. 113

[135] Sun, X., Keesee, A. M., Biloiu, C., Scime, E. E., Meige, A., Charles, C., and Boswell, R. W., "Observations of Ion-Beam Formation in a Current-Free Double Layer," *Physical Review Letters*, Vol. 95, July 2005, pp. 025004–1–4, doi: 10.1103/PhysRevLett.95.025004. 124

[136] Fruchtman, A., "The Thrust of a Collisional-Plasma Source," *IEEE Transactions on Plasma Science*, Vol. 39, No. 1, Jan. 2011, pp. 530–539, doi: 10.1109/TPS.2010.2089067. 131, 133

[137] Kaeppelin, V., Carrère, M., and Layet, J.-M., "Ion energy distribution functions and Langmuir probe measurements in low pressure argon discharges," *Journal of Vacuum Science & Technology A: Vacuum, Surfaces, and Films*, Vol. 20, No. 2, Mar.-Apr. 2002, pp. 526–529, doi: 10.1116/1.1451274. 132

[138] Hegerberg, R., Elford, M. T., and Skullerud, H. R., "The cross section for symmetric charge exchange of Ne^+ in Ne and Ar^+ in Ar at low energies," *Journal of Physics B: Atomic and Molecular Physics*, Vol. 15, No. 5, March 1982, pp. 797–811, doi: 10.1088/0022-3700/15/5/022. 132

[139] Rao, M. V. V. S., Van Brunt, R. J., and Olthoff, J. K., "Resonant charge exchange and the transport of ions at high electric-field to gas-density ratios (*E/N*) in argon, neon, and helium," *Physical Review E: Statistical, nonlinear, and soft matter physics*, Vol. 54, No. 5, Nov. 1996, pp. 5641–5656, doi: 10.1103/PhysRevE.54.5641. 132

[140] Reid, B. M., *The Influence of Neutral Flow Rate in the Operation of Hall Thrusters*, Ph.D. thesis, Aerospace Engineering, University of Michigan, Ann Arbor, MI, 2009. 132

[141] Shabshelowitz, A. and Gallimore, A. D., "Ion Energy Distribution Measurements of a Radiofrequency Plasma Source Immersed in Vacuum," *38th IEEE International Conference on Plasma Science*, Chicago, IL, doi: 10.1109/PLASMA.2011.5993301, June 2011. 132

[142] Brown, D. L., Larson, C. W., Beal, B. E., and Gallimore, A. D., "Methodology and Historical Perspective of a Hall Thruster Efficiency Analysis," *Journal of Propulsion and Power*, Vol. 25, No. 6, Nov.-Dec. 2009, pp. 1163–1177, doi: 10.2514/1.38092. 133, 134, 138

[143] Lias, S. G., "Ionization Energy Evaluation," *NIST Chemistry WebBook, NIST Standard Reference Database Number 69*, Eds. P. J. Linstrom and W. G. Mallard, National Institute of Standards and Technology, Gaithersburg, MD, 20899, http://webbook.nist.gov, retrieved May 31, 2012. 139, 140